POLITECNICO

MILANO 1863

Department of Energy
Doctoral Program in Energy and Nuclear Science and Technology

Mechanistic modeling of fission gas behavior in conventional and advanced nuclear fuel

Supervisors

Prof. Lelio Luzzi
Dr. Giovanni Pastore
Dr. Paul Van Uffelen

Tutor

Prof. Lelio Luzzi

The Chair of the Doctoral Program
Prof. Vincenzo Dossena

Doctoral Dissertation by
Tommaso Barani

XXII Cycle

JULY 2020

Acknowledgments

Abstract

Modeling the behavior of fission gas is a fundamental step to predict the thermo-mechanical performance of nuclear fuels under irradiation, given its role in determining the condition of the fuel rods in normal operating conditions and potentially affecting fuel rod operation in reactor under off-normal and accident conditions. This thesis work deals with the development of Fission Gas Behavior (FGB) models for the analysis of conventional and advanced nuclear fuels, and their application to Fuel Performance Codes (FPCs). The modeling approach I followed in this thesis relies on a physically-based description of the involved phenomena, in order to properly describe the behavior of nuclear fuel in the widest possible range of conditions, allowing also to bridge different modeling scales, i.e., transferring information gathered at atomistic scale on the parameters of the developed models to the continuum mechanics scale, typical of FPCs. Yet, the modeling approach retains a computational burden in-line with requirements dictated by the target recipients of this work, i.e., FPCs. I applied this modeling strategy to develop original models for nuclear fuels for conditions in which available models cannot be applied or entail critical limitations. In particular, I tackled (i) the evolution of intra-granular bubbles in UO_2, focusing on high temperature transient conditions, in which bubble abnormal growth (*coarsening*) may be responsible up to about half of the fuel total swelling; (ii) the restructuring encountered in oxide fuels at high local irradiation damage leading to the formation of the high burnup structure (HBS) and the associated, peculiar intra- and inter-granular FGB; (iii) the evolution of intra- and inter-granular fission gas bubbles in U_3Si_2, an enhanced accident tolerant fuel investigated as a possible replacement of conventional UO_2 in light water reactors. The developed models constitute a significant step forward with respect to the state-of-the-art, filling gaps in the physical description of nuclear fuels included in current FPCs. I implemented the models into the SCIANTIX code, an open-source software developed at POLIMI, meant to be either a stand-alone code or to be included in FPCs as a module accounting for FGB. I compared each model predictions to available separate-effect experiments, always accompanied with predictions by models included in state-of-the-art FPCs to underline the progress brought by this work. In the case of uranium silicide, since no experimental data are available in power reactor conditions, I performed a thorough sensitivity analysis aimed at identifying the most important parameters considered in the model, thus suggesting priorities for the future efforts on the lower-length scale calculations. Given the promising results from the stand-alone comparisons, I made available the developed models to FPCs, via a direct implementation in the code (e.g., in the BISON FPC) or via a coupling to SCIANTIX (e.g., for the TRANSURANUS FPC).

Contents

List of Tables

List of Figures

List of Acronyms

3DOT	3D Oregonstate TRIM
AFC	Advanced Fuel Campaign
ATF	Accident Tolerant Fuel
ATR	Advanced Test Reactor
BCA	Binary Collision Approximation
BRT	Beginning of the Ramp Test
CD	Cluster Dynamics
CEA	Commissariat à l'énergie atomique et aux énergies alternatives
DFT	Density Functional Theory
EBSD	Electron Backscatter Diffraction
EoS	Equation of State
EPFL	École Polytechnique Fédérale de Lausanne
EPMA	Electron Probe Micro Analysis
ERT	End of the Ramp Test
FBR	Fast Breeder Reactor
FG	Fission Gas
FGB	Fission Gas Behavior
FGR	Fission Gas Release
FPC	Fuel Performance Code
GB	Grain-boundary
HBS	High Burnup Structure
HS	Hard Sphere
I-NERI	International Nuclear Energy Research Initiative
INL	Idaho National Laboratory
INSPYRE	Investigations Supporting MOX Fuel Licensing for ESNII Prototype Reactors
IRSN	Institut de radioprotection et de sûreté nucléaire
JRC	Joint Research Center
KJMA	Kolmogorov-Johnson-Mel-Avrami
LHR	Linear Heat Rate
LOCA	Loss of Coolant Accident
LWR	Light Water Reactor
MD	Molecular Dynamics
MES	Method of Exact Solutions
MIMAS	MIcronized MASterblend
MMS	Method of Manufactured Solutions
MOX	U-Pu Mixed Oxides
NEB	Nudged Elastic Band
PAW	Projector Augmented-Wave
PBE	Perdew-Burke-Ernzerhof
PCI	Pellet-Cladding Interaction

PIE	Post-Irradiation Examinations
POLIMI	Politecnico di Milano
PWR	Pressurized Water Reactor
RIA	Reactivity Initiated Accident
SEM	Scanning Electron Microscopy
TRIM	Transport of Ions in Matter
VASP	Vienna Ab initio Simulation Package

List of Symbols

A	atm m^{-3}	First moment of the HBS pore-size distribution
A_{gf}	m^2	Projected area of grain-boundary bubbles
a_L	m	Lattice parameter of UO$_2$
a_s	m^3	Setyawan re-solution model parameter
B	atm^2 m^{-3}	Second moment of the HBS pore-size distribution
B_{ig}	m^3	Volume occupied by gas atoms in intra-granular bubbles
bu	MWd kg$_U^{-1}$	Local fuel burnup
bu_{eff}	MWd kg$_U^{-1}$	Local fuel effective burnup
c, c_1	atm m^{-3}	Concentration of single fission gas atoms in intra-granular dynamic solution
c_{gb}, q	atm m^{-3}	Concentration of gas at the grain boundaries
c_n	atm m^{-3}	Number density of a gas cluster containing n atoms
c_t	atm m^{-3}	Total concentration of fission gas atoms in a fuel grain
D	m^2 s^{-1}	Single gas atom diffusion coefficient
D_{eff}	m^2 s^{-1}	Effective gas atom diffusion coefficient
D_i^d	m^2 s^{-1}	Interstitial diffusion coefficient along dislocations
D_v^d	m^2 s^{-1}	Vacancy diffusion coefficient along dislocations
D_{gb}^{SA}	m^2 s^{-1}	Gas atoms diffusion coefficient at grain boundaries
D_{gb}^v	m^2 s^{-1}	Vacancy diffusion coefficient at grain boundaries
$D_{i,bulk}$	m^2 s^{-1}	Bulk interstitial diffusion coefficient
$D_{v,bulk}, D_{ig}^v$	m^2 s^{-1}	Bulk vacancy diffusion coefficient
D_n	m^2 s^{-1}	Total (surface plus volume) diffusion coefficient of a cluster containing n gas atoms
d_V	m	Critical distance from the HBS pore surface allowing atom re-solution
$\dot{F}$	fiss m^{-3} s^{-1}	Fission rate density
F_c, F_{gf}	(/)	Grain-boundary fractional coverage
$F_{c,sat}, F_{gf,sat}$	(/)	Grain-boundary saturation fractional coverage
f_{gf}	(/)	Fraction of non-cracked grain faces
f_n	(/)	Nucleation factor for intra-granular bubbles in U$_3$Si$_2$
$f(R_b)$	bbl m^{-3} m^{-1}	Intra-granular bubble density distribution
G	atm m^{-3} s^{-1}	Fission gas atoms production rate
$g(bu)$	(/)	Function of local burnup limiting grain growth
H	(/)	Hard-sphere nearest neighbor distribution
j	m	Jump distance of Xe or vacancies in U$_3$Si$_2$
K	bbl m^{-1}	Number of bubbles nucleated dislocation
K_A	s$^{-\gamma_A}$	Phase transformation rate constant
k_B	J K^{-1}	Boltzmann constant
M	m^2 s^{-1}	Grain boundary mobility
m, m_b	atm m^{-3}	Concentration of fission gas atoms in bulk intra-granular bubbles

N	bbl or pore m^{-3}	Intra-granular bubble or HBS pore number density
N_{gf}	bbl m^{-2}	Inter-granular bubble areal density
n	atm bbl^{-1}	Number of atoms per intra-granular bubble
$\bar{n}$	atm pore^{-1}	Average number of atoms per bubble or HBS pore
n_d	atm bbl^{-1}	Number of atoms per bubble at dislocation
n_g	atm bbl^{-1}	Number of atoms per bubble at grain boundary
n_{iv}	vac bbl^{-1}	Number of vacancies per intra-granular bubble
n_v^d	vac bbl^{-1}	Number of vacancies per bubble at dislocation
n_v	vac bbl^{-1}	Number of vacancies per bubble at grain boundary
$n_{v,p}$	vac pore^{-1}	Number of vacancies per HBS pore
$n(R_b)$	atm bbl^{-1}	NUmber of atoms in an intra-granular bubble of radius R_b
$P_1,\ P_2,\ P_3$	kW m^{-1}	Power levels of White and co-workers experiments
p	Pa	Bubble or HBS pore pressure
p_{eq}	Pa	Bubble or HBS pore equilibrium pressure
R	m	Intra-granular bubble or pore radius
$\dot{R}$	atm $m^{-3}\,s^{-1}$	Total rate of atom re-soluted from intra-granular bubbles
R_{ff}	m	Radius of influence of a fission fragment
R_{gf}	m	Inter-granular bubble radius
R_n	m	Radius of a bubble or HBS pore containing n gas atoms
R_{sg}	m	Radius associated to a single gas atom in the fuel matrix
r_d	m	Radius of influence associated to a dislocation
r_{gr}	m	Fuel grain radius
r_m	m	Limiting size for grain growth
$r_{gr,\infty}$	m	Asymptotic grain radius in the HBS
$r_{WS,d}$	m	Radius of the Wigner-Seitz cell associated to a dislocation
$\bar{T}$	°C	Threshold temperature for effective burnup calculation
t	s	Time
V_d	m^3	Dislocation bubble volume
V_d^*	m^3	Volume associated to the complex dislocation/bulk volume
V_f	m^3	Fuel volume
V_{gf}	m^3	Volume of grain boundary bubbles
V^P	m^3	HBS pore volume
v	s^{-1}	Attempt frequency of Xe or vacancies jump in U_3Si_2
y	atm fiss^{-1}	Fission gas atom atomic yield per fission
Z	(/)	Available sites for a Xe or vacancy jump in U_3Si_2
$\tilde{y}$	(/)	Hard Sphere packing fraction

α	s^{-1}	Re-solution rate of gas atoms from bubbles or HBS pore
$\alpha_n,\ b_n$	s^{-1}	Re-solution rate of gas atoms from a bubble or HBS pore containing n atoms
α_r	(/)	Volumetric fraction of restructured fuel
α_0	atm fiss^{-1}	Re-solution parameter in U_3Si_2
$\alpha',\ \alpha''$	s^{-1}	First and second derivative of pore re-solution rate to cluster size
β	s^{-1}	Trapping rate of gas atoms into a bubble or a HBS pore
$\beta_n,\ g_n$	s^{-1}	Trapping rate of gas atoms into a bubble or a HBS pore containing n atoms
$\beta',\ \beta''$	s^{-1}	First and second derivative of pore trapping rate to cluster size
β'_d	s^{-1}	Trapping rate of gas atoms at dislocations
γ	$\mathrm{J\,m}^{-2}$	Gas/material surface tension
γ_A	(/)	Avrami constant
$\Delta V/V$	(/)	Generic expression for fuel swelling
δ	m	Radius of the Wigner-Seitz cell associated to a dislocation bubble
δ_b	m	Radius of the Wigner-Seitz cell associated to a bulk intra-granular bubble
δ_{gb}	m	Thickness of grain boundaries
δ_{HS}	m	Hard sphere diameter for Xe
δ_V	m	Thickness of the re-solution layer around a HBS pore
ζ	(/)	Sink strength of a spherical secondary phase inclusion
η	bbl ff^{-1}	Bubbles nucleated per fission fragment
θ	°	Semi-dihedral angle of grain-boundary bubbles
κ	atm m^{-3} s^{-1}	Gas arrival rate at the grain boundaries
λ	s^{-1}	Generic decay term of an ordianry differential equation
$\lambda^d,\ \lambda^P$	(/)	Correction factor for hard spheres coalescence equation
μ_{ff}	m	Fission fragment length
ν	bbl or pore m^{-3} s^{-1}	Nucleation rate of intra-granular gas dimers or HBS pores
ξ	(/)	Local fuel porosity or gaseous swelling
ρ_d	m^{-2}	Intra-granular dislocation density
ρ_p	m	Radius of the Wigner-Seitz cell associated to a HBS pore

σ_h	Pa	Hydrostatic stress acting on the bubble or pore
τ	GWd t_{UO2}^{-1}	Characteristic time for HBS formation in the SCIANTIX model
τ_{1-4}	h	Duration of the power holdings of White and co-workers experiments
υ	atm m^{-3}	Atomic density in a HBS pore
φ	(/)	Geometric factor linking circular and lenticular bubbles areal projection
ϕ, ϕ_b, ϕ_d	(/)	Correction factor accounting for dimer removal in homogeneous re-solution
ψ	(/)	Ratio of secondary phase inclusion radius to its Wigner-Seitz cell radius
Ω	m^3	Vacancy volume
ω	m^3	Xenon atomic volume

atm:	atom
bbl:	bubble
ff:	fission fragment
fiss:	fission
vac:	vacancy

To M.S.

CHAPTER 1. FOREWORD AND MOTIVATIONS

"Ma il canale scorre lieve, tranquillo e sicuro nel mare, non è canale, limite, Regulation, bensì fluire che si apre e si abbandona alle acque e agli oceani di tutto il globo, e alle creature delle loro profondità"

————————————

C. Magris, *Danubio*, 1986

This thesis work deals with the development of mechanistic models of Fission Gas Behavior (FGB) for the analysis of conventional and advanced nuclear fuels, and their application to Fuel Performance Code (FPC) environments. Modeling of FGB is a fundamental step to predict the performance of nuclear fuels under irradiation, given its role in determining the thermo-mechanical condition of fuel rods and potentially affecting fuel rod operation in reactor [1, 2].

The need for improved safety and the design of future nuclear reactors, combined to the exigence of increasing flexibility of nuclear reactors to cope with output of renewable sources, calls for the improvement of the traditional UO_2-zirconium fuel system currently employed in nuclear reactors, or the development of new fuel and cladding materials. While the legacy approach to development of fuel systems massively relied on costly experimental campaigns, current trends of reducing the time (and costs) of nuclear fuel development enlighten the importance of combining experimental efforts to reliable computational tools [3]. In this process, fuel performance codes play a major role in nuclear fuel design, licensing, and analysis under irradiation [1, 4, 5]. Essentially, these codes perform the thermo-mechanical analysis of fuel rods (i.e., predicting stress, strain, displacement, and temperature fields), accounting for all the phenomena occurring in the fuel rods under irradiation in reactor, in normal operating, transient, and accident conditions [5].

To correctly represent fuel performance, various intricate and interrelated phenomena must be modeled to predict the evolution of material properties and microstructure, which in turn strongly affects the thermo-mechanical analysis of the nuclear fuel rod [5, 6]. The enormous experimental database built over the years on the UO_2-zirconium system performance and the inherent difficulty in developing mechanistic models for the behavior of nuclear fuel led to the development of fuel performance codes featured by empirical models. Such models quantify phenomena as a function of local temperature, burnup, with parameters fitted to experimental results, thus can describe accurately nuclear fuel behavior within their calibration range, yet they bring about significant limitations [3]. In fact, they cannot extrapolate outside their calibration range. Moreover, fuel performance codes featured by such models cannot be used to analyze different (normal and off-normal) reactor conditions, or new fuel systems as well. Thus, FPCs are being integrated with more predictive

models to boost the modifications of current fuel systems and/or be employed in the design and licensing of next generation fuel systems and reactors based on sound physical understanding.

Among the various phenomena occurring in nuclear fuel under irradiation, FGB plays a crucial role in determining the overall fuel rod behavior and performance [2, 5]. Fission Gas (FG), mainly xenon and krypton, is produced by fissions in nuclear fuel grains. Subsequently, a population of intra-granular bubbles forms, exchanging atoms with the fuel matrix through the trapping and re-solution mechanisms, along with a net diffusion of gas atoms towards grain boundaries. At grain boundaries, a population of inter-granular bubbles arises, which may interconnect and grow, ultimately forming a connected path to the rod free volume and causing the release of FGs. These FG bubbles are responsible for the fuel gaseous swelling, whilst dissolved atoms in the fuel matrix concur in determining the fuel matrix swelling. Moreover, the external part of oxide nuclear fuel (and the regions in the proximity of Pu-rich agglomerates in uranium-plutonium mixed oxide fuel) may experience a re-crystallization of the original polycrystalline structure, due to severe irradiation conditions achieved at high local burnups. The resulting so-called High Burnup Structure (HBS) is characterized by smaller grains than the original microstructure, and by large pores collecting FG and responsible for additional fuel swelling. Indeed, the combination of these processes strongly affects the thermo-mechanical behavior of nuclear fuels, under normal operating and transient/accident conditions. The primary role of FGB in determining the nuclear fuel rod performance in both Light Water Reactor (LWR) and Fast Breeder Reactor (FBR) conditions is confirmed by its investigation in the framework of different international research projects [7–11]. Among them, this thesis work grafts on the Investigations Supporting MOX Fuel Licensing for ESNII Prototype Reactors (INSPYRE) H2020 European Project [10], the SciDAC project of the US DOE [11], and an International Nuclear Energy Research Initiative (I-NERI) collaboration project between US DOE and EURATOM involving Politecnico di Milano (POLIMI), Joint Research Center (JRC) Karlsruhe, and Idaho National Laboratory (INL).

Two different approaches are possible to describe FGB in the frame of fuel performance codes: (i) correlation-based approaches, in which fission gas release and gaseous swelling are calculated via expressions directly related to macroscopic quantities that characterize the state of the fuel rod (e.g., fuel temperature and burnup) and tuned on experimental data [12–20], and (ii) physics-based approaches, which aim at describing the physical mechanisms of fission gas behavior within the fuel[1] [21–34]. Indeed, mechanistic modeling approaches are preferable to meet the aforementioned goals about nuclear fuels development. Mechanistic models can describe nuclear fuel performance in normal, transient, and high burnup conditions [5, 21, 23, 25, 31, 34–37]. Moreover, mechanistic models are not subject to constrains dictated by the calibration range of empirical correlations, since they are built upon

---

[1] Often hybrid approaches are used, combining correlation-based and physics-based models to describe different phenomena, e.g., a correlation can be used for fuel gaseous swelling and paired with a physics-based description of fission gas release as driven by diffusion (e.g., [12, 16]), or representing only partial steps of the fission gas evolution through mechanistic approaches, relegating the remainder to empirical correlations [21].

evolution equations describing (up to a targeted detail) the underlying physical processes. This latter aspect is crucial, since mechanistic models allow for the so-called scale bridging [8, 9, 34, 38–44], i.e., the transfer of information calculated through lower-length scale methods (e.g., ab initio or molecular dynamics) to the scale of interest for engineering-scale applications, complementing information from experiments with very detailed insights on material behavior at the atomic or meso-scale (multi-scale modeling). Finally, mechanistic models are applicable with minor modifications to different fuel materials [3, 45–47].

In this work, I leverage a multi-scale mechanistic approach to represent FGB, demonstrating how this modeling technique is (i) suitable to describe some aspects of FGB in transient/high burnup condition in conventional uranium dioxide nuclear fuel, which have been neglected so far for application in FPCs, in an original manner and (ii) to develop an original description of FGB in a fuel material – U_3Si_2, a candidate accident tolerant material to replace UO_2 in conventional LWR applications [48] – of recent consideration for use in power reactors. More in detail, the phenomena I tackled in this thesis are:

- The *coarsening* (i.e., abnormal growth) of intra-granular bubbles in UO_2, which could be responsible for a conspicuous part of fuel swelling in high temperature transients and high burnup conditions [49, 50] (Chapter 2)

- The restructuring of oxide fuels microstructure at high local irradiation damage (HBS formation), accompanied by a peculiar intra- and inter-granular FGB with strong implications on local fuel swelling [51]. (Chapter 3)

- The evolution of intra- and inter-granular bubbles in U_3Si_2, and resulting FGB [43]. (Chapter 4)

Being conceived for engineering-scale FPCs, the models enforce a more detailed description of the underlying physical phenomena, while retaining a degree of complexity (in terms of computational burden and numerical robustness) in-line with the requirements of FPC application. In fact, one should consider that FGB models are applied to every integration node of the computational mesh of FPC models, which can gather thousands of nodes, and for every time step of a simulation which normally can span multiple years.

The conceptual flow of the work carried out in this thesis is shown in Figure 1.1. The development strategy I followed in this work to effectively pursuing the goals of the thesis followed a common route among the different models for the development phase, whilst it was twofold for the assessment phase.

As for the development side, I implemented and verified all the models in the stand-alone computer code SCIANTIX [52], currently under development in the Nuclear Reactor Groups at POLIMI and of which I am one of the main authors. This code is a meso-scale code, describing FGB at the level of the fuel grain, meant for model verification, validation against local measurements, and designed to be included in existing FPCs in a multi-scale coupling scheme. As for the assessment against experimental data, I compared stand-alone model predictions when local measurements were available (i.e., the case for uranium dioxide models). For the uranium silicide FGB model, a significant experimental database is not available, due
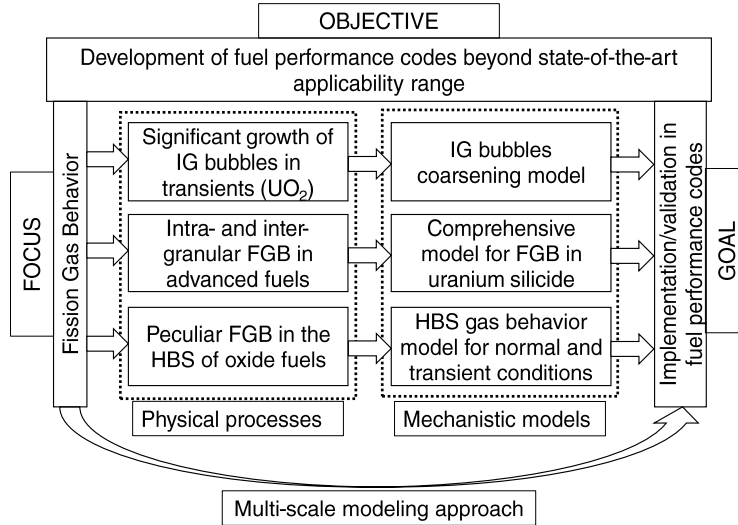
Figure 1.1: Conceptual organization of this thesis work.

to the new conception of the fuel system for use in power reactors. Thus, I performed a comprehensive sensitivity and uncertainty analysis on the model parameters to support the conclusions of this work and to guide future research efforts, since an integral (i.e., by means of a FPC) assessment against ongoing experiments is not yet achievable.

The models developed in this thesis work surpass critical constraints of state-of-the-art FPCs. In fact, the new models consider critical FGB phenomena that are currently neglected in FPCs, albeit being very important in determining fuel performance under irradiation. Moreover, the description of FGB in uranium silicide constitutes a pivotal step towards the analysis and design of this fuel system for use in LWRs. Lastly, the model development followed a multi-scale approach, i.e., integrates information derived at atomic scale into the developed models conceived for application in FPCs. This aspect is a key component of the followed approach, allowing to infer model parameters which would be impossible to derive from experiments, and represents the only method to speed up model development for novel fuel systems. I included the developed models in the SCIANTIX code, thus they will entirely be released as open source, being available to the general public.

I introduced the developed models in engineering-scale fuel performance codes. In particular, I considered the codes TRANSURANUS [12], developed at the European Commission JRC in Karlsruhe, and BISON [53], developed at INL, under the aegis of a long-lasting collaboration between POLIMI, JRC-Ka, and INL.

To summarize, the outcome of this thesis is threefold:

- The development of more mechanistic models aimed at filling gaps in state-of-the-art FPC capabilities to describe FGB in uranium dioxide in a broad range of conditions, comprising – but not limited to – high temperature transients and high burnup conditions.

- The development of more mechanistic models to provide FPCs with capabilities to describe FGB in a novel, accident-tolerant fuel material (i.e., uranium silicide) to boost its design phase. This activity constitutes a fundamental step in understanding uranium silicide behavior in LWR conditions, which would not be possible otherwise, given the scarcity of experimental data on this material in such conditions.

- The introduction of the developed models in engineering-scale fuel performance codes. The models are made available to the codes either via a direct implementation into the code itself (which is the case of the models introduced in the BISON code), or via the coupling of SCIANTIX with the code of interest (which is the case of the models made available to the TRANSURANUS code).

The structure of this thesis is as follows. In each Chapter, I provide a detailed presentation of the phenomena of interest, of the models available in the state of the art, of their consideration or not in fuel performance codes, alongside the original work carried out in this thesis. As anticipated above, the model about intra-granular bubble coarsening is presented in Chapter 2, the HBS modeling efforts are showcased in Chapter 3, whereas I present a comprehensive model for U_3Si_2 FGB in Chapter 4. Each Chapter comes with specific closing remarks, whereas I present the thesis general conclusions and future perspectives in Chapter 5. Given the primary role played by the SCIANTIX code in this thesis, an overview of this tool is presented in the Appendix.

As a closing annotation, I report the published and/or submitted papers to international journals constituting the foundations of the presented Chapters:

- Chapter 2: T. Barani, G. Pastore, A. Magni, D. Pizzocri, P. Van Uffelen, L. Luzzi, "Modeling intra-granular fission gas bubble evolution and coarsening in uranium dioxide during in-pile transients", Journal of Nuclear Materials, No. 152195, 2020.

- Chapter 3:

  - T. Barani, D. Pizzocri, F. Cappia, L. Luzzi, G. Pastore, P. Van Uffelen, "Modeling High Burnup Structure in Oxide Fuels for Application to Fuel Performance Codes. Part I: High Burnup Structure formation", Accepted for publication, Journal of Nuclear Materials.

  - T. Barani, D. Pizzocri, F. Cappia, L. Luzzi, G. Pastore, P. Van Uffelen, "Modeling High Burnup Structure in Oxide Fuels for Application to Fuel Performance Codes. Part II: High Burnup Structure porosity evolution", In preparation.

- Chapter 4: T. Barani, G. Pastore, D. Pizzocri, D.A. Andersson, C. Matthews, A. Alfonsi, K.A. Gamble, P. Van Uffelen, L. Luzzi, J.D. Hales, "Multiscale modeling of fission gas behavior in U_3Si_2 under LWR conditions", Journal of Nuclear Materials, vol. 522, pp 97–110, 2019.

- Appendix: D. Pizzocri, T. Barani, L. Luzzi, "SCIANTIX: A new open source multi-scale code for fission gas behaviour modelling designed for nuclear fuel performance codes", Journal of Nuclear Materials, vol. 532, No. 152042, 2020.

CHAPTER 2. MODELING INTRA-GRANULAR FISSION GAS BUBBLE COARSENING IN URANIUM DIOXIDE DURING IN-PILE TRANSIENTS

"È questione d'equilibrio
Non è mica facile"

———————

Baustelle, *Charlie fa surf – Amen*, 2008

Abstract

The description of intra-granular fission gas behavior during irradiation is a fundamental part of models used for the calculation of fission gas release and gaseous swelling in nuclear FPCs. The relevant phenomena include diffusion of gas atoms towards the grain boundaries coupled to the evolution of intra-granular bubbles. While intra-granular bubbles during normal operating conditions are limited to sizes of a few nanometers, experimental evidence exists for the appearance of a second population of bubbles during transients, characterized by coarsening to sizes of tens to hundreds of nanometers and that can significantly contribute to gaseous fuel swelling. Typically, existing fission gas behavior models are limited to the evolution of nanometric intra-granular bubbles. In this Chapter, I present a model of intra-granular fission gas behavior in uranium dioxide fuel that includes both nanometric fission gas bubble evolution and bubble coarsening during transients. The developed model incorporates the fundamental mechanisms of gas atom diffusion to grain boundaries and dislocations, gas bubble nucleation and re-solution, gas atom and vacancy absorption at bubbles, and bubble coalescence by impingement. While retaining a physical basis, the developed model is relatively simple and is intended for application in engineering FPCs. I assess the model through comparisons to a substantial number of experimental data from SEM observations of intra-granular bubbles in power ramp tested uranium dioxide samples. The results demonstrate that the model reproduces the coarsening of a fraction of the intra-granular bubbles and correspondingly, predicts gaseous swelling during power ramps with a significantly higher accuracy than is allowed by traditional models limited to the evolution of nanometric intra-granular bubbles.

2.1 Introduction

The behavior of the gaseous fission products xenon and krypton significantly affects the performance of nuclear fuel rods during irradiation [1, 5]. Gas atoms are created in the fuel grains during fission events and due to their low solubility, tend to precipitate forming bubbles. Intra-granular bubble evolution is governed by gas atom trapping from the matrix into the bubbles and the counteracting mechanism of irradiation-induced re-solution of gas atoms from the bubbles back into the matrix. Concomitantly, diffusion to grain boundaries of atoms dissolved in the matrix occurs [2, 7, 21, 54–56]. The behavior of gas at grain boundaries determines inter-granular gaseous swelling and fission gas release to the rod free volume [2, 5]. Although inter-granular swelling due to Grain-boundary (GB) bubbles is the dominant contribution to gaseous fuel swelling under normal operating conditions, intra-granular swelling becomes significant during transients to high temperatures and at high burnups [50, 57–61].

During normal operating conditions, intra-granular fission gas bubbles are generally limited to sizes of one to a few nanometers [49]. However, experiments have shown the appearance of a second population of bubbles characterized by sizes of tens to hundreds of nanometers, which has been observed following post-irradiation annealing, power ramps and in high-burnup fuel [49, 50, 57–64]. Although the mechanisms for such abnormal bubble growth are largely unknown (see, e.g., [49, 50, 63, 64]), there is evidence that the larger bubbles are associated with dislocations [50, 57, 58, 65]. The population of larger bubbles can account for local gaseous swelling of up to 7-8% volumetric fraction [50, 61, 62] and is therefore of high engineering interest.

Given the importance of FGB in fuel rod performance, models for fission gas release and gaseous fuel swelling have been developed and incorporated in engineering FPCs [2, 19, 21, 23, 24, 26–31, 33, 34, 61]. However, these models are generally limited to the evolution of nanometric bubbles [21, 23, 24, 26, 29, 31, 33]. Developing models able to represent the bubble coarsening effect and that can be effectively applied in FPCs appears necessary in order to accurately model fuel behavior in high temperature transients and high-burnup conditions. Modeling fuel gaseous swelling during transients such as power ramps has implications, for example, in the analysis of Pellet-Cladding Interaction (PCI) [66, 67].

A detailed calculation of intra-granular bubble size distribution is achievable through cluster dynamics methods (e.g., [27, 68–71]). These methods allow for calculating the evolution of atom clusters (bubbles) distribution, tightly coupling re-solution and trapping phenomena acting on each cluster. Although being very accurate, these methods are generally not applied directly in FPCs due to a high computational cost. In engineering fuel performance calculations, fission gas models are called, for each time step and each non-linear iteration, in every element of the computational mesh, thus they need to be computationally efficient, hindering the application of cluster dynamics approaches in this computational scheme. In the recent years, models have been developed to calculate fission gas release and gaseous swelling in UO_2 [25, 26, 34, 72], which constitute the foundation of mechanistic FGB calculations in the TRANSURANUS and BISON FPCs [12, 53, 73, 74]. In particular,

in [26] a model for intra-granular fission gas behavior was developed. The model is limited to the evolution of nanometric fission gas bubbles during normal operating conditions and represents the bubble size distribution with the mean size and the total number density ('single-size' model). In this work, I extend the description of intra-granular FGB presented in [26] to consider bubble evolution and coarsening during high-temperature transients other than during normal operating conditions.

A model for bubble coarsening under post-irradiation annealing conditions was proposed by White [61]. In particular, White considered the role of the dislocation network in the fuel acting as a vacancy sink or a vacancy source, with vacancy absorption at intra-granular bubbles being dependent on the dislocation density. White's model only covered annealing conditions and the population of coarsened bubbles visible through SEM, without consideration of bubble nucleation and re-solution. A purely empirical model of intra-granular bubble coarsening was proposed by Lösönen [29, 64]. In this model, coarsening was triggered at the attainment of a temperature threshold, with the average bubble radius during coarsening being calculated as a function of time with an exponential relation leading to a (fixed) saturation value of 100 nm. Mechanistic modeling of intra-granular bubble coarsening under irradiation was considered by Veshchunov and coworkers [23, 31, 75]. In this case, bubble coarsening during transients was ascribed to bubble-size dependent re-solution of fission gas atoms from bubbles. In particular, as re-solution becomes less effective with increasing bubble radius, it was postulated that a fraction of the bubbles may surmount a 'critical' size beyond which they are able to further grow without significant restriction.

The model developed in the present work considers the reduced effectiveness of resolution with increasing bubble radius on the basis of atomic-scale calculations but also invokes the role of dislocations as a source of vacancies and preferential growth along dislocations as the mechanism for bubble coarsening. The model computes the average size and number density of both populations of nanometric bubbles in the fuel bulk and coarsening bubbles along dislocations, the corresponding gaseous fuel swelling, and diffusion of single gas atoms to grain boundaries which is coupled to bubble evolution. While both nanometric and coarsening bubbles are modeled, only the average size of each population is considered. In this sense, the new model can be considered as a 'two-size' description of intra-granular bubble evolution.

The model presented in this work integrates information obtained from atomistic calculations for the parameters (in particular, for re-solution rate and defect diffusivities). Yet, it is meant for inclusion in engineering-scale fuel performance codes, thus retains a focus to end-user, industrial applications.

Model predictions, in terms of bubble size, number density and gaseous swelling, are compared to the extensive experimental database of White and coworkers [50], consisting of SEM observations of power ramp tested UO$_2$ samples.

The outline of the Chapter is as follows. In Section 2.2, I discuss the physical processes considered for fission gas behavior and the related modeling, including the developed theory for bubble coarsening. In Section 2.3, I present the general formulation of the intra-granular FGB model. In Section 2.4, I present the comparison of model predictions to experimental data. Closing remarks are presented in Section 2.5.

2.2 Physical processes

2.2.1 General considerations

The in-pile evolution of intra-granular bubbles in oxide nuclear fuels is mainly governed by the following processes: bubble nucleation, irradiation-induced re-solution of gas atoms from the bubbles back into the lattice, absorption of gas atoms (trapping) and vacancies at bubbles, and bubble coalescence.

During normal operating conditions, intra-granular bubbles generally have number densities of the order of $10^{23} - 10^{24}$ m^{-3}, spherical and/or faceted shape[2], diameters of one to a few nanometers, and a gas density of 3-7 kg m^{-3} [63, 65, 78–82], close to the density of solid-state Xe (e.g., [21, 49, 56, 65, 82]). In these conditions, intra-granular bubbles are strongly overpressurized, as concluded by authors analyzing fuels irradiated in commercial light water reactors up to 80 GW d t^{-1} [80, 83]. The over-pressurization and small size of intra-granular bubbles during normal operating conditions has been ascribed to a 'vacancy starvation' effect, which has been postulated for UO$_2$ under both irradiation and annealing[3] conditions [61, 83, 85, 86]. During high-temperature transient and high-burnup conditions, while the population of nanometric bubbles is still present, a second population of coarsened bubbles with lower number densities and larger sizes of tens to hundreds of nanometers has been observed [50, 57–61]. Coarsened bubbles can be associated with significant fuel gaseous swelling [50, 61, 62]. This selective bubble growth under certain conditions suggests that a threshold process exists for the activation of significant absorption of vacancies at a fraction of the bubbles.

I refer to the abnormal growth of a fraction of the intra-granular bubbles as bubble *coarsening*. When dealing with a diluted phase in a two-phase system, this term is usually adopted in the literature in reference to the growth of larger particles absorbing solute atoms which are made available by smaller particles [87–89]. This process, which is known as Ostwald ripening, has been considered by several authors to describe the growth of gas bubbles and voids in nuclear materials (e.g., [36, 90–93]). While I refer to the abnormal intra-granular bubble growth adopting the same terminology, I do not consider Ostwald ripening as the phenomenon responsible for abnormal growth of intra-granular bubbles during irradiation, as I will detail in the following.

Mechanisms that have been proposed for bubble coarsening under in-pile and annealing conditions include bubble coalescence through bubble migration due to surface or volume diffusion, and Ostwald ripening [23, 49, 59, 90, 91, 94]. An additional mechanism of bubble growth has been investigated by molecular dynamics employing empirical pair potentials by Murphy and co-workers [95]. They suggest

---

[2]In UO$_2$, faceted bubbles have been observed by a few authors (e.g., [76, 77]), especially when the radii reach values of multiple nanometers.

[3]An exception is represented by the evolution during annealing tests of intra-granular bubbles located near grain boundaries, which can act as a source of thermal vacancies, allowing for localized bubble coarsening and/or vacancy-assisted migration [35, 59, 84].

that nanometric intra-granular bubbles would force the surrounding oxygen ions into the lattice to relieve the internal pressure. Even though this mechanism may contribute to relaxing the bubble internal pressure, I consider that further evidence is needed before it can be regarded as a primary contribution to bubble coarsening.

As for bubble migration either via surface or volume diffusion, from a theoretical perspective, the effectiveness of both phenomena in UO_2 under irradiation is drastically reduced at bubble radii exceeding ≈ 10 nm [23, 35, 96, 97]. This is due to the dependence of volume and surface diffusivities on the bubble radius, with diffusivities being proportional to R_b^{-3} and R_b^{-4} [35], respectively. Moreover, the activation energy of cations in UO_2 is deemed too high to cause an appreciable volume diffusion mechanism [23]. Also, various mechanisms of surface diffusion suppression under irradiation have been elucidated in the literature [35, 49]. Ostwald ripening involves a transfer of gas atoms from small bubbles to larger ones. This mechanism is inhibited if the bubbles are strongly overpressurized [49, 90, 94], as is the case for the nanometric bubbles in UO_2 grains experiencing the vacancy starvation condition. Moreover, Ostwald ripening involves (thermal) re-solution of gas atoms from small bubbles being transferred to larger ones. Thermal re-solution would entail high solubility of gaseous fission products in the UO_2 crystal, to enable a substantial flux of gas atoms from the small bubbles to the larger ones. On one hand, xenon should retain a non-zero solubility in the crystal matrix close to intra-granular bubbles and its solubility should increase with temperature and bubble over-pressurization. On the other, the expected low value of solubility prevents a substantial thermal re-solution to take place [95, 98, 99]. Lastly, in-pile experimental intra-granular bubble size distributions reported in [50] exhibit a right skewness which is not compatible with Ostwald ripening effects (cf [89]). Nevertheless, it must be noted that in high temperature annealing experiments on irradiated UO_2 Ostwald ripening may play a role in the coarsening of intra-granular bubbles, together with vacancy-assisted migration and coalescence (e.g., [35, 36, 59, 61, 75, 100]). In fact, grain boundaries in these conditions may act as source of thermal vacancies for the intra-granular bubble population.

The observations of coarsened bubbles being along dislocations [50, 57, 58, 65] suggest a role of dislocations in favoring selected bubble growth under certain conditions. It is accepted that fission gas bubbles at grain boundaries grow to micrometric sizes through vacancy absorption (e.g., [30]), which is favored at grain boundary bubbles compared to the bulk of the fuel. Bubble growth due to vacancy absorption at grain boundaries driven by bubble overpressure has been broadly considered in modeling inter-granular fission gas behavior (e.g., [30, 34]). As a conceptual extension of the accepted behavior at grain boundary bubbles, I propose bubble growth through vacancy absorption at line defects (i.e., dislocations) as a mechanism of intra-granular bubble coarsening. Bubbles along dislocations may absorb vacancies from the region of the medium where dislocations induce a compressive local stress state, which convoys vacancies. The condition for the activation of vacancy absorption is considered as the bubble internal energy (pressure) exceeding the mechanical equilibrium pressure. Also, as coarsened bubbles may reach a size compatible with the inter-bubble distances, bubble coalescence by impingement is also considered.

The effect of size-dependent re-solution as put forward in [23, 31, 75] provides an

explanation for bubble coarsening that is alternative, or complementary, to the role of dislocations, and may be further investigated in the future.

In the following, I discuss modeling of the individual physical processes considered for the evolution of nanometric bubbles in the bulk and for bubble coarsening at dislocations, before presenting the formulation of the overall model in Section 2.3.

2.2.2 Bubble nucleation

Two different approaches have been proposed to model the rate of fission gas bubble nucleation in UO_2. The homogeneous mechanism describes bubble nucleation as a consequence of diffusion-limited precipitation of gas atom dimers [56, 75, 101], while the heterogeneous mechanism considers nucleation as a direct consequence of fission spikes [26, 102, 103]. Although both mechanisms are presumably active, following a previous work [26] I model the nucleation of small intra-granular bubbles in the bulk of the grain as heterogeneous. The nucleation rate ν_b (bubble $m^{-3}\,s^{-1}$) is calculated as

$$\nu_b = 2\eta\dot{F} \tag{2.1}$$

where η (bubble per fission fragment) is in the range 5-25 [65, 102], $\dot{F}$ (fission $m^{-3}\,s^{-1}$) is the fission rate density, and the factor of 2 corresponds to the approximate number of fragments generated by each fission event.

Nucleation of bubbles lying along dislocations may be due to the precipitation of gas in the region where dislocations induce a tensile stress state, due to the larger radii of fission gas atoms atoms with respect to U [104]. Rather than directly describing this mechanism, I choose to adopt a simplified approach. I consider a step-wise nucleation of dislocations and a subsequent constant value for simplicity, thus a one-off nucleation of associated bubbles, reading

$$\begin{aligned} N_d(t=0) &= N_{d,0} \\ \nu_d &= 0 \end{aligned} \tag{2.2}$$

where and N_d (bubble m^{-3}) the number density of bubbles at dislocations, $N_{d,0} = K \cdot \rho_d$, being ρ_d ($m\,m^{-3}$) the space-averaged dislocation density in the fuel grain, K (bubble m^{-1}) is a model parameter representative for the number of bubbles nucleated per dislocation, and ν_d (bubble $m^{-3}\,s^{-1}$) the nucleation rate of bubbles at dislocations. While this approach is followed here for simplicity, a more refined treatment is envisaged where the nucleation is calculated as

$$\nu_d = K \cdot \frac{d\rho_d}{dt} \tag{2.3}$$

and coupled to a model describing the time evolution of the dislocation density (e.g., [31]). In this work, I assume an overall representative dislocation density, without

distinguishing among the different types of dislocations. Furthermore, I assume that the dislocations are immobile, i.e., I neglect conservative and non-conservative dislocation motion. This latter phenomenon is indeed playing a role at temperatures of interest for the application of the herein presented model, but its inclusion in the analysis would call for a dislocation evolution model, which is prone to uncertainties and beyond the scope of the present work and is left as future development.

2.2.3 Gas atom trapping

In the present model, I consider the trapping of single gas atoms at bubbles as well as at dislocations. In turn, gas atoms trapped at dislocations are considered to provide an additional contribution to gas inflow at bubbles that lie along dislocations. Bubbles are assumed to be spherical. Following Ham [105], the trapping rate at bubbles in the bulk is calculated as

$$\beta_b = 4\pi D R_b N_b \tag{2.4}$$

and the trapping rate at bubbles along dislocations is calculated as

$$\beta_d = 4\pi D R_d N_d \tag{2.5}$$

where β (s^{-1}) is the trapping rate, D ($\mathrm{m^2\,s^{-1}}$) the single gas atom diffusion coefficient, R the bubble radius, and N (bubble m^{-3}) the number density of bubbles, and the subscripts b and d refer to bubbles in the bulk and along dislocations, respectively. For the trapping rate at dislocations, I write

$$\beta' = \frac{2\pi D_d \rho_d}{\ln \dfrac{r_{ws,d}}{r_d} - \dfrac{3}{5}} \tag{2.6}$$

where β' (s^{-1}) is the trapping rate, D_d ($\mathrm{m^2\,s^{-1}}$) is the xenon diffusivity close to the dislocation core, $r_{ws,d} = 1/\sqrt{\pi \rho_d}$ (m) the radius of the Wigner-Seitz cell associated with a dislocation, and r_d (m) is the dislocation core radius, taken equal to five times the magnitude of the UO$_2$ Burgers vector. The diffusion coefficient of single gas atoms in the bulk of the grain is calculated according to Turnbull and co-workers [106], whereas the gas diffusivity close to the dislocation core has been derived from the work of Murphy and co-workers [107] – the corresponding correlations are reported in a subsequent Section of this Chapter.

As a modeling assumption, gas atoms captured by dislocations are considered as instantaneously trapped into bubbles along dislocations. The hypothesis is justified by the rapid diffusion of species near the core of dislocations (pipe diffusion), as shown, e.g., by Murphy et al. [107]. In addition, direct trapping of gas atoms from the bulk at bubbles along dislocations is considered. It follows that the total rate of gas atom trapping at bubbles along dislocations is given by $\beta_d + \beta'$.

2.2.4 Re-solution

As for the re-solution of gas atoms from the bubbles, no clear consensus emerges from the literature regarding the dominating mechanism in uranium dioxide, i.e., whether the interaction of intra-granular bubbles with fission fragments occurs by complete bubble destruction (so-called *heterogeneous* mechanism) or by gradual re-dissolution of individual gas atoms (*homogeneous* mechanism). *Heterogeneous* re-solution was advocated by legacy theoretical works (e.g., by Turnbull [102], Blank and Matzke [108]), while the *homogeneous* mechanism was originally proposed by Nelson [109] and more recently by Schwen and coworkers [110, 111]. Molecular Dynamics (MD) calculations performed by Govers et al. [112] and more recently, by Setyawan et al. [113] provided support for re-solution being induced by the thermal spike due to electronic stopping, which corresponds to the heterogeneous re-solution model, while at the same time allowing for a partial re-dissolution of the gas for sufficiently large bubbles, a behavior closer to the homogeneous model.

In the present model, I adopt the following expression or the resolution rate developed through MD calculations by Setyawan et al. [113], which I apply to both bubbles in the bulk and at dislocations:

$$\alpha = \left(a_s \exp(-b_1 \cdot R) + \frac{b_0 - a_s}{1 + c \cdot R^2} \exp\left(-d \cdot R^2\right) \right) \cdot \dot{F} \tag{2.7}$$

where α (s^{-1}) is the resolution rate, R (m) is the bubble radius and a_s, b_0, b_1, c, d are parameters from [113]. In particular, I considered the parameters corresponding to a ratio between the thermal spike energy and the total electronic stopping power of 0.73, as suggested in [113]. This formulation for the re-solution rate improves and extends through atomistic methods the legacy work on resolution from Turnbull [102], and introduces consideration of the thermal spike energy dissipation, the off-centered ballistic distance (i.e., the distance between the thermal spike and the bubble center), and the reduced efficiency of resolution with increasing bubble radius. The latter aspect is particularly important for the present work, where large coarsened bubbles are considered. The reduced resolution efficiency with increasing bubble radius evaluated by Setyawan and coworkers through lower-length scale modeling confirms the theoretical conclusions from other authors, e.g., [23, 27, 64].

A sketch of the processes described above is reported in Figure 2.1.

2.2.5 Bubble coarsening along dislocations

In the proposed model, the bubble coarsening mechanism is naturally activated during transient conditions according to the physical representation adopted.

I assume that bubbles at dislocations may absorb vacancies when their internal energy (pressure) exceeds the mechanical equilibrium pressure. This condition is favored during transients to high temperatures, when additional gas atom trapping
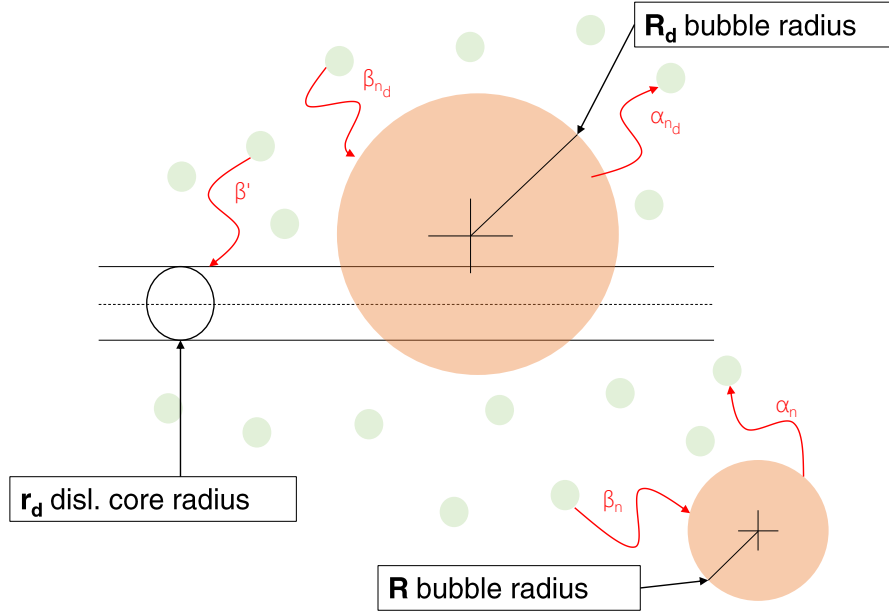
Figure 2.1: Sketch of the gas atoms trapping into and re-solution from bubbles considered in the model. In particular, β_n, β_{n_d}, and β' represent the trapping of single gas atoms into bulk intra-granular bubbles, into dislocation bubbles, and on dislocation lines, respectively while α_n and α_{n_d} represent the re-solution of gas atoms from bulk and dislocation bubbles, respectively, to the matrix.

at bubbles due to enhanced thermal diffusion acts to increase bubble pressure. It is also favored for bubbles along dislocations, which undergo additional inflow of gas atoms following trapping at dislocations (Section 2.2.3), compared to bubbles in the bulk. As I assume that vacancies are available near dislocations, once the condition is met, vacancy absorption at bubbles along dislocations and the associated bubble growth are considered. Modeling details are given below.

Vacancy absorption

The rate of vacancy absorption at a dislocation bubble is calculated using an adaptation of the Speight-Beere model [30, 43, 114, 115], as

$$\frac{\mathrm{d}n_v^d}{\mathrm{d}t} = \frac{2\pi D_v^d \delta}{k_B T \zeta}(p_d - p_{d,eq}) \tag{2.8}$$

where n_v (vacancy bubble^{-1}) is the number of vacancies per bubble, D_v^d (m^2 s^{-1}) the vacancy diffusion coefficient along dislocations, δ (m) the radius of the equivalent

Wigner-Seitz cell associated with a dislocation bubble[4], k_B (J K^{-1}) the Boltzmann constant, T (K) the local temperature, p_d and $p_{d,eq}$ (Pa) are the bubble pressure and the equilibrium pressure, respectively, and ζ (/) is a dimensionless factor calculated as [43]

$$\zeta = \frac{10\psi(1+\psi^3)}{-\psi^6 + 5\psi^2 - 9\psi + 5} \tag{2.9}$$

where $\psi = R_d/\delta$ is the ratio between the radii of the dislocation bubble and of the cell. The present model for vacancy absorption/emission is a reformulation of the Speight and Beere model for behavior at grain boundaries of bubbles of circular projection (2D problem) [30, 114]. In particular, Eqs. 2.8, 2.9 represent the equivalent model for vacancy absorption/emission at spherical pore absorbing/emitting vacancies isotropically (3D representation). The different dimensionality of the problem yields a different expression for ζ relative to [114].

The pressure of the gas in the bubble is evaluated considering the hard sphere equation of state, in the formulation by Carnahan and Starling [116], reading

$$\frac{p_d V_d}{n_d kT} = \frac{1 + \widetilde{y} + \widetilde{y}^2 - \widetilde{y}^3}{(1 - \widetilde{y})^3} \tag{2.10}$$

where n_d (atom bubble^{-1}) is the number of atoms per dislocation bubble, $\widetilde{y} = \pi/6 \, (\delta_{HS}^3 \upsilon)$ (/) is the packing fraction, υ (atom m^{-3}) is the atomic density in the bubble, i.e., the ratio between the average number of atoms per bubble and the bubble volume, and δ_{HS} (m) is the hard sphere diameter for xenon. The latter is calculated according to Brearley and MacInnes [117], considering a modified Buckingham interatomic potential and reading

$$\delta_{HS} = 4.45 \cdot 10^{-10} \left(0.8542 - 0.03996 \cdot \log \left(\frac{T}{231.2} \right) \right) \tag{2.11}$$

with the local temperature, T, expressed in K. The Carnahan-Starling equation of state is considered more suitable for the pressure ranges of interest in the present study, relative to other options such as the perfect gas law or the van der Waals equation of state [118, 119].

The equilibrium pressure is determined by the surface energy, γ (J m^{-2}), and the hydrostatic stress in the surrounding medium, σ_h (Pa) via the capillarity relationship, i.e.,

$$p_{d,eq} = \frac{2\gamma}{R_d} - \sigma_h \tag{2.12}$$

where $p_{d,eq}$ (Pa) is the equilibrium pressure and R_d the radius of a dislocation bubble.

---

[4]The radius of the Wigner-Seitz cell is determined by the relationship $4/3 \, \pi N_d \delta^3 = 1$.

As for the vacancy pipe diffusion coefficient along dislocations, D_v^d, in the absence of available data, I consider previous work on bulk diffusivity of defects in UO_2 [120] and on pipe diffusion of interstitials [121] to derive a tentative correlation for the vacancy diffusivity, as follows. I apply the assumption of the ratio between the vacancy diffusion coefficients at dislocations and in the bulk being the same as for interstitial atoms, i.e.,

$$\frac{D_v^d}{D_{v,bulk}} = \frac{D_i^d}{D_{i,bulk}} \ . \tag{2.13}$$

I use the bulk diffusion coefficient for vacancies and interstitials, $D_{v,bulk}$ and $D_{i,bulk}$ $(m^2\,s^{-1})$, from Andersson et al. [120], and the interstitial pipe diffusion coefficient, D_i^d $(m^2\,s^{-1})$ from the results by Murphy et al. [121]. The corresponding relations are as follows:

$$\begin{aligned}
D_{v,bulk}(T) &= 7.12 \cdot 10^{-7} \exp\left(\frac{-4.72\text{eV}}{k_B T}\right) \\
D_{i,bulk}(T) &= 1.2 \cdot 10^{-6} \exp\left(\frac{-4.70\text{eV}}{k_B T}\right) \\
D_i^d(T) &= 6.4 \cdot 10^{-2} \exp\left(\frac{-1.82\text{eV}}{k_B T}\right)
\end{aligned} \tag{2.14}$$

Combining Eqs. 2.13 and 2.14, I derive the following temperature-dependent correlation for D_v^d $(m^2\,s^{-1})$:

$$D_v^d(T) = 3.8 \cdot 10^{-2} \exp\left(\frac{-1.84\text{eV}}{k_B T}\right) \tag{2.15}$$

The above procedure must be regarded as a tentative approach to derive an approximate correlation for vacancy diffusivity in the dislocation core. More refined analyses that better characterize this parameter are of interest as a future development. Indeed, it can be noticed how the derived activation energy is compatible with the analysis by Murphy and co-authors, reported in [121]. The diffusion coefficients in Eqs. 2.14 and 2.15 are plotted in Figure 2.2.

Bubble coalescence

As the radius of coarsened bubbles at dislocations can become comparable with the average inter-bubble distance [50, 59], inter-connection of bubbles and the associated bubble coalescence need to be considered. Following [122], I consider intra-granular bubbles as a three-dimensional system of spheres, randomly distributed according to a Poisson distribution. Torquato [123] showed that inter-connection occurs when bubbles are sufficiently large and high in number, i.e., when their volume fraction (i.e., porosity) is sufficiently high, around 10%. This value is consistent with experimental SEM observations of intra-granular coarsened bubbles [50, 59],
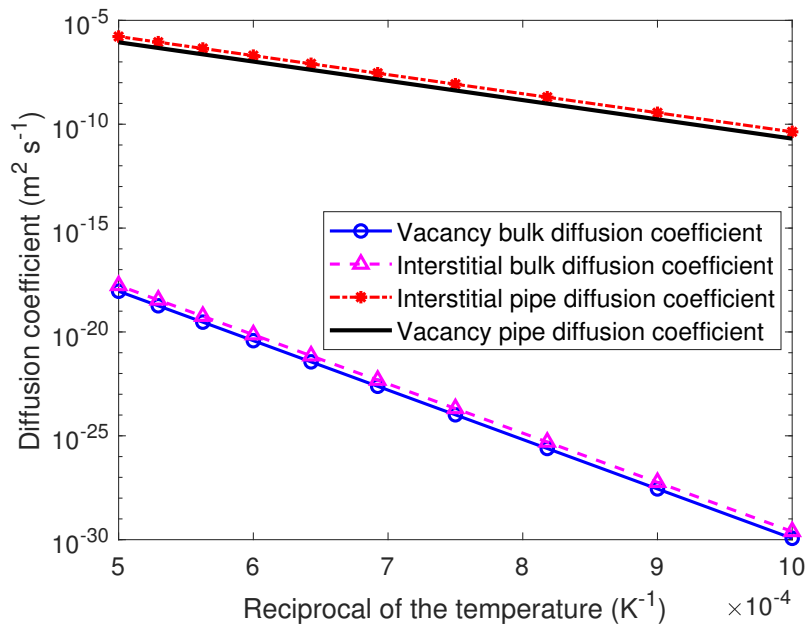
Figure 2.2: Adopted correlations for the diffusion coefficients of vacancies and interstitials in UO_2 as a function of the temperature.

supporting the inclusion of a bubble inter-connection description in the present model.

For the system of two populations of intra-granular bubbles considered in this work, i.e., one in the bulk of the grain and one associated with dislocations, two modes of inter-connection are modeled. In particular, I neglect coalescence between nanometric bulk bubbles, and account for coalescence between (i) two large bubbles along dislocations and (ii) one dislocation bubble and one bulk bubble.

The inter-connection between two large dislocation bubbles is modeled assuming that only pair interactions take place and considering bubbles as hard-spheres. The first assumption is made to overcome the need of knowing the non-trivial complete probability density function for a system of hard-spheres, which is replaced by the nearest-neighbor distribution function. The second assumption avoids the nonphysical possibility for two intra-granular bubbles to share the same region of a fuel grain. Following the work done in [124], the equation for the variation rate of the number density of dislocation bubbles due to coalescence can be obtained from [123] as

$$\frac{dN_d}{N_d} = -\frac{1}{2} \int_1^{1+\frac{dR_d}{R_d}} H(x)dx \tag{2.16}$$

where $x = r/2R_d$ is the normalized distance between two dislocation bubbles, N_d the dislocation bubble number density, and $H(x)$ is the nearest-neighbor distribution function for hard-spheres [123, 125, 126]. Equation 2.16 is reshaped as follows

$$\frac{dN_d}{dV_d} = -4\lambda^d N_d^2 \tag{2.17}$$

where V_d (m) is the bubble volume, and $\lambda^d = (2 - \xi)/[2(1 - \xi)^3]$ is a correction factor accounting for the hard-sphere assumption, with $\xi = \frac{4}{3}\pi R_d^3 N_d$ being the porosity associated with dislocation bubbles. As a consequence of coalescence, the number density of dislocation bubbles decreases while the total gas content remains the same, which corresponds to a higher number of gas atoms per bubble and consequently an increased average radius. It must be noticed that the current formulation of the interconnection model may need further investigations to estimate the impact of the array disposition of bubbles attached to dislocations, which may increase the probability of interaction, thus the growth rate [123].

As for the interaction between a dislocation bubble and a bulk bubble[5], I assume that all the bulk bubbles which belong to a sphere of volume $V_d^* = \frac{4}{3}\pi(R_d + R)^3$ are captured by the expanding dislocation bubble, transferring all their gas content to the latter. The probability that a small bubble is incorporated by a growing dislocation bubble is $N_b \cdot dV_d^*$, with $dV_d^* = 4\pi(R_d + R)^2 dR_d$. Consequently, the decrease in number density of bulk bubbles due to coalescence with dislocation bubbles is given by

$$\frac{dN_b}{dV_d^*} = -N_d \cdot N_b \tag{2.18}$$

2.3   Model formulation

Considering the mechanisms described in Section 2.2, the developed model of intra-granular bubble evolution extends the normal operating conditions model developed in [26] by adding consideration of a second population of bubbles along dislocations, which is subject to coarsening driven by vacancy absorption. Moreover, in line with the formulation of the re-solution parameter proposed by Setyawan and coauthors [113], I consider a *homogeneous* re-solution mechanism as proposed in [43]. While both small bubbles in the bulk and coarsening bubbles at dislocations are modeled, only the average size of each population is considered.

The system of coupled partial differential equations governing the evolution of fission gas atom concentrations is

$$\begin{cases} \dfrac{\partial c}{\partial t} = D\nabla^2 c - (\beta_b + \beta_d + \beta')c + \alpha_b\phi_b m_b + \alpha_d\phi_d m_d - 2(\nu_b + \nu_d) + y\dot{F} \\ \dfrac{\partial m_b}{\partial t} = 2\nu_b + \beta_b c - \alpha_b\phi_b m_b \\ \dfrac{\partial m_d}{\partial t} = 2\nu_d + (\beta_d + \beta')c - \alpha_d\phi_d m_d \end{cases} \tag{2.19}$$

---

[5]The present model does not account for bulk bubble mobility in isothermal conditions, since I focus on in-pile transients. Although experimentally observed to some extent [76], no clear consensus arises in the literature about it [52, 84]. A possible way of including bubble mobility in the present modeling framework is presented in [127].

where c (atom m^{-3}) is the concentration of single gas atoms, m_b (atom m^{-3}) the total concentration of gas in bulk bubbles, m_d (atom m^{-3}) the total concentration of gas in dislocation bubbles, and y (atom fission^{-1}) the fission yield. The coefficients are defined in Section 2.2, with the subscript b and d distinguishing between the parameters referring to bulk and dislocation bubbles, respectively. The evolution of bubble number densities is governed by

$$\frac{\partial N_b}{\partial t} = \nu_b - \alpha_n \phi_b N_b - N_d \cdot N_b \frac{\partial V_d}{\partial t}$$

$$\frac{\partial N_d}{\partial t} = \nu_d - \alpha_{n_d} \phi_d N_d - 4\lambda^d N_d^2 \frac{\partial V_d}{\partial t}$$

(2.20)

where the first term corresponds to nucleation, the second to re-solution and the third to coalescence. The average number of gas atoms per bubble for bulk and dislocation bubbles, respectively, is given by

$$n_b = \frac{m_b}{N_b}$$

$$n_d = \frac{m_d}{N_d}$$

(2.21)

Following[43], the correction of the re-solution rates accounting for the homogeneous mechanism – namely ϕ_b and ϕ_d – are calculated as

$$\phi_b = \frac{1}{n_b - 1}$$

$$\phi_d = \frac{1}{n_d - 1}$$

(2.22)

Solution of Eqs. 2.19-2.21 provides the number densities and average numbers of atoms per bubble of the two populations. As discussed in Section 2.2.5, dislocation bubbles are considered to absorb vacancies from the compressive-stress region next to the dislocation core when their internal energy exceeds the equilibrium value, while this relaxation mechanism is not considered for bulk bubbles (vacancy starvation [83, 85, 86]). The volume of dislocation bubbles (assumed to be spherical) is determined by their gas atom and vacancy contents according to the following relationship

$$V_d = n_d \omega + n_v^d \Omega \qquad (2.23)$$

where ω (m^3 atom^{-1}) is the volume of a fission gas atom, calculated consistently with the adopted equation of state[6], and Ω (m^3 vacancy^{-1}) is the vacancy volume. The volume of bulk bubbles (also assumed spherical) is calculated as (e.g., [26, 56])

$$V_b = n_b B \qquad (2.24)$$

---

[6]I assume that fission gas atoms diffuse via neutral complexes of defects (Schottky trios, i.e., one vacancy from the uranium sublattice and two vacancies from the oxygen sublattice [128]). Thus, when captured into a bubble, atoms bring about a contribution to the bubble volume.

where B (m^3) is the volume occupied by a fission gas atom in an intra-granular bubble. Finally, the fractional increment in fuel volume, V_f (m^3), due to intra-granular gaseous swelling[7] is computed as

$$\frac{\Delta V_f}{V_f} = N_d V_d + N_b V_b \qquad (2.25)$$

The formulation of the model calls for further considerations on the underlying assumptions. First, the evolution of dislocation density under irradiation is not modeled in this work. Rather, I consider a constant value, not dependent on temperature and/or burnup. On the other hand, Nogita and Une [129] found an exponential dependence of the dislocation density on the local burnup, analyzing the rim zone of light water reactor UO$_2$ fuel (i.e., where temperatures are relatively low throughout the irradiation). These experimental findings must be considered when the presented model is applied to high burnup conditions. It is worth noting that the inclusion of dislocations in fission gas behavior modeling is very challenging. In particular, the attempt of describing the evolution of dislocations under irradiation requires detailed modeling of point and extended defect evolution (e.g., [130–133]). Such models may account for dislocation evolution in a mechanistic fashion, yet they are featured by a complexity level which may not be compatible with requirements of engineering FPCs. While modeling dislocation evolution (especially accounting for the non-conservative motion at high temperatures) is of interest in perspective, it is out of the scope of the present work.

Considering a constant value for the dislocation density along with the simplified model for nucleation (Eq. 2.3) results in a "one-off" nucleation of dislocation bubbles, whose number density may then evolve due to irradiation-induced re-solution and interconnection. Although this is a significant simplification, I choose not to model explicitly nucleation of bubbles along dislocations to avoid the introduction of additional model parameters which may be affected by high uncertainties.

The new model generalizes the description of the intra-granular behavior of fission gas bubbles already presented in [26], extending it to the evolution of dislocation bubbles and the coarsening phenomenon. While preserving a physical foundation, the final model formulation entails a limited number of equations and parameters, which makes it suitable for incorporation in engineering-scale FPCs. The work presented in this Chapter is meant to complement the suite of models [25, 26, 34, 72] previously developed to account for FGB in fuel performance calculations, currently available in BISON [53], TRANSURANUS [12], and SCIANTIX [52]. In particular, the current model targets the behavior of intra-granular fission gas, indirectly modifying the grain-boundary FGB by affecting the diffusional flux of gas exiting the fuel grain. Finally, the gaseous swelling computed by the presented model adds to the one due to inter-granular bubbles, thus providing an additional deformation source to higher scale simulations, i.e., when considering the SCIANTIX code coupled to FPCs.

---

[7]It must be noted that the swelling I am referring to does not consider the contribution of fission products dissolved in the fuel matrix.

2.4 Model comparisons to experimental data

In this Section, I present the comparisons of model predictions to experimental data. I implemented the presented model in, and performed the simulations by, the SCIANTIX code [52], a meso-scale computer code presented in the Appendix.

2.4.1 Choice of model parameters

The nominal values of the parameters used in the model are summarized in Table 2.1, while in this Section I briefly discuss the choice of the most critical parameters.

The calculation and choice of the re-solution rate have been deeply discussed in Section 2.2. Resorting on very recent atomistic calculations which expand the legacy treatment by Turnbull [102], this estimation of the re-solution parameter is the most updated and complete option available in the open literature. As for the nucleation parameter for the bubble along dislocations, it is a model parameter roughly estimated from the ratio between the experimental bubble densities along dislocations and the dislocation density. Indeed, this parameter governs the initial bubble density at dislocations and plays a primary role in determining the evolution of this bubble population. Similarly, the average dislocation density in the grain has been taken as a constant value. Indeed, it is known that this parameter varies during irradiation, although its trend is most likely determined by a prompt-jump and a subsequent slow kinetics. The introduction of a more physic-based treatment of dislocation behavior represents one of the major challenges of the present model.

The diffusion coefficient is known for being one key parameter for fission gas behavior models and one of the most uncertain [2, 72]. The high uncertainties in its estimation, from both experimental (for the inherent issues in the determination of the fuel stoichiometry, the initial amount of gas in the sample, etc) and computational side (e.g., for the uncertainty in the Density Functional Theory (DFT) calculations due to the estimation of the U parameter, the calculation of entropies from empirical potentials) do not yield a definitive choice among the options available in the open literature. In this work, I chose to consider the correlation of Turnbull and co-workers [106, 134], since it is the more widely used in the community. Indeed, a study dedicated to this parameter influence on the results would complement the present work. As for the diffusion coefficient close to the dislocation core, it has been extracted from the only work in the open literature studying the parameter, based on molecular dynamics calculations [107].

Table 2.1: Nomenclature and corresponding values or correlations for the characteristic rates and parameters of the intra-granular bubble evolution model.

Symbol	Definition	Value	U.O.M.	Reference
a_s	Re-solution model parameter	$9.49 \cdot 10^{-24}$	m^3	[113]
b_1	Re-solution model parameter	$7.07 \cdot 10^{-2}$	m^{-1}	[113]
b_0	Re-solution model parameter	$9.18 \cdot 10^{-23}$	m^3	[113]
c	Re-solution model parameter	7.982	m^{-2}	[113]
d	Re-solution model parameter	$3.71 \cdot 10^{-2}$	m^{-2}	[113]
K	Number of bubbles nucleated or destroyed per dislocation	$1 \cdot 10^6$	bubble m^{-1}	Present work
B	Volume occupied by a fission gas atom in intra-granular bubbles	$4.09 \cdot 10^{-29}$	m^3	[26, 56, 135]
D	Diffusion coefficient of fission gas atoms in UO_2 $$D = D_1 + D_2 + D_3$$ $$D_1 = 7.6 \cdot 10^{-10} \exp\left(-4.86 \cdot 10^{-19}/k_B T\right)$$ $$D_2 = 5.46 \cdot 10^{-25} \sqrt{\dot{F}} \exp\left(-1.91 \cdot 10^{-19}/k_B T\right)$$ $$D_3 = 2 \cdot 10^{-40} \dot{F}$$		$m^2 s^{-1}$	[106]
D_d	Diffusion coefficient of xenon close to the dislocation core $$D_d = 7.74 \cdot 10^{-6} \exp\left(-1.21 \cdot 10^{-19}/kT\right)$$		$m^2 s^{-1}$	[107]
b_B	UO_2 Burgers vector magnitude	$3.85 \cdot 10^{-10}$	m	-
r_d	Dislocation core radius	$5 \cdot b_B$	m	E.g., [36]
γ	UO_2 gas surface energy	0.7	$J\,m^{-2}$	E.g., [21]
η	Number of bubbles nucleated per fission fragment	25	bubble per fission fragment	[21]
ρ_d	Average dislocation density in the fuel grain	$4 \cdot 10^{13}$	$m\,m^{-3}$	E.g., [50]
Ω	Vacancy co-volume	$4.09 \cdot 10^{-29}$	m^3	[135]

2.4.2   Experimental database

The database chosen to validate the model is the SEM experimental database by White and coworkers [50]. The database consists in measurements performed on 12 UO_2 Advanced Gas Reactor samples of fuel rods irradiated up to burnup between 9 and 21 $GW\,d\,t^{-1}$ in the Halden reactor. After the base irradiation, rods were subjected to power ramp or power cycle histories. SEM examinations were then performed at different radial positions, obtaining from 3 to 7 radial examinations on each sample, composing a wide database of local data for sizes and number densities of intra-granular bubbles, and of intra-granular swelling. Details about the irradiation conditions are given in Table 2.2 and a sketch of power ramps is provided in Figure 2.3.

The specific power, temperature, and hydrostatic stress for each SEM sample, needed as inputs for SCIANTIX simulations, are calculated values from the ENIGMA code [136]. The experimental data considered in this work in terms of intra-granular bubble radius, density, and resulting swelling refers to the second peak of the bi-modal intra-granular bubble size distribution as compiled by White and coworkers [50], which is deemed to be associated to dislocation bubbles.
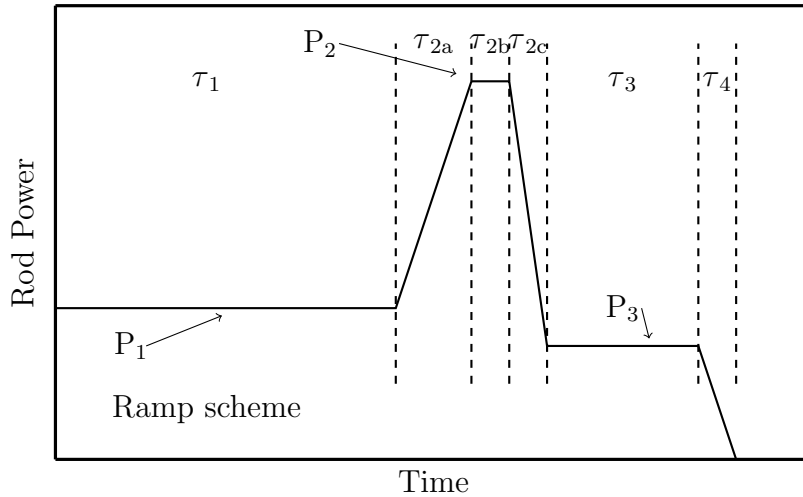
Figure 2.3: Schematic representation of a generic ramp test from the considered experiments [50]. For the meaning of the symbols, the reader is referred to Table 2.2.

Table 2.2: Detailed description of the power histories performed on the fuel samples of the considered SEM database [50].

Rod ID	P_1 (kW m^{-1})	τ_1	τ_{2a} (min)	P_2 (kW m^{-1})	τ_{2b} (min)	τ_{2c}	P_3 (kW m^{-1})	τ_3	τ_4
4000	14.0	12 d	1.52	40.0	30.0	100 s	14.0	99.0 min	SCRAM
4004	14.0	12 d	1.97	40.0	2.38	90 s	14.0	99.0 min	SCRAM
4005	14.0	12 d	1.32	40.0	2.0	-	SCRAM	-	-
4064	20.0	15 wk	47.0	43.0	0.0	-	SCRAM	-	-
4065	19.3	3 wk	47.0	41.8	0.0	-	SCRAM	-	-
	18.5	1 wk	65.0	36.9	0.0	40 s			
4135	13.0	8.0 min	40 s	36.9	80 s	40 s			
	13.0	0.0	40 s	36.9	80 s	40 s	16.0	28 d	6 h
4136	16.5	1 wk	63.0	36.0	0.0	-			
	36.0	0.0	2.0	39.0	0.0	40 s	16.0	27 d	6 h
4140	16.5	1 wk	65.0	36.0	0.0	40 s	16.0	27 d	6 h
4162	18.0	3 wk	45.0	40.0	0.0	40 s	18.0	6 min	-
4163	18.0	3 wk	45.0	35.0	0.0	40 s	18.0	41 h	-

2.4.3 Results

The comparisons of simulations to experimental data from [50] are reported in Figures 2.4-2.6 for the average bubble radius (Figure 2.4), number density (Figure 2.5), and corresponding gaseous swelling (Figure 2.6). Experimental data and simulation results for both quantities are collected in Table 2.3. For comparison, I include also the results obtained applying the model by Pizzocri et al. [26] (black symbols in Figures 2.4-2.6). It must be underlined that the model by Pizzocri and coworkers does not feature a description of bubble coarsening. Its inclusion is rather intended as to demonstrate how the available model is not able to represent the gaseous swelling due to coarsened bubbles, thus the step forward brought about by the model I developed.
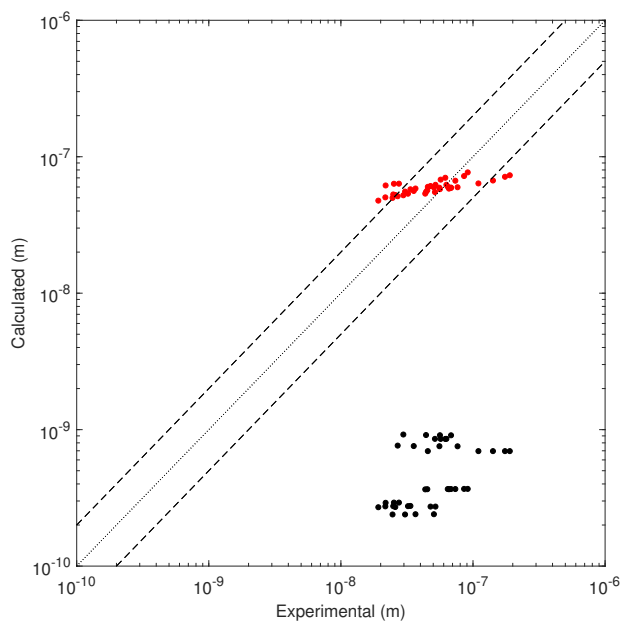
Figure 2.4: Comparisons of model predictions for bubble radius to experimental data from [50]. Each symbol corresponds to a local simulation for one of the SEM radial points in the experimental database. Both results obtained with the new transient model (red symbols) and with the previous normal operation model [26] (black symbols) are included.
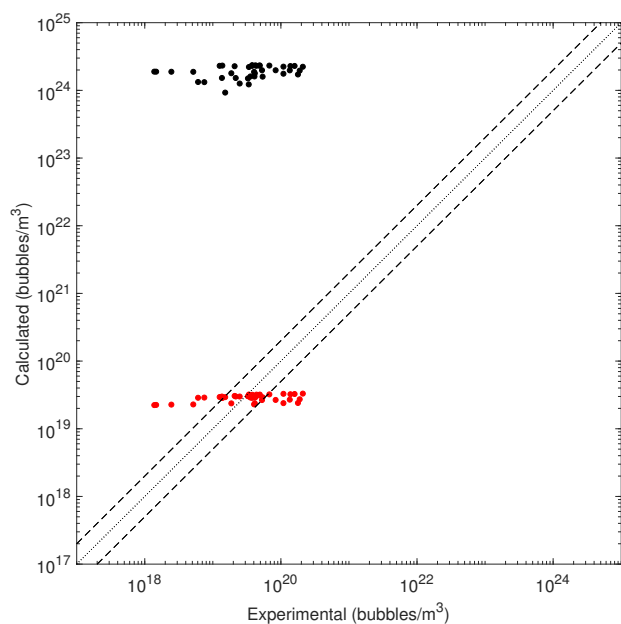
Figure 2.5: Comparisons of model predictions for bubble number density to experimental data from [50]. Both results obtained with the new transient model (red symbols) and with the previous normal operation model [26] (black symbols) are included.
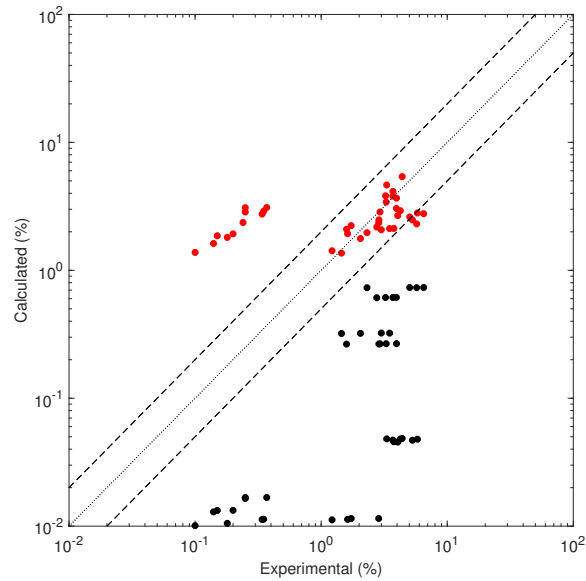
Figure 2.6: Comparisons of model predictions for bubble swelling to experimental data from [50]. Both results obtained with the new transient model (red symbols) and with the previous normal operation model [26] (black symbols) are included.

The overall agreement between experimental data and model predictions (red symbols in Figures 2.4-2.6) appears satisfactory for this initial application. In particular, sizes of tens to hundreds of nanometers for the coarsened intra-granular bubbles, and volumetric swellings of one to several percent, in these ramp-tested fuel samples are reproduced. Note that these values are orders of magnitude higher than bubbles sizes and swellings observed under normal operating conditions, and could not be captured with traditional models that do not include specific transient capabilities. This is confirmed by the comparison with the results obtained using the previous model (black symbols).

Calculations with the present model exhibit deviations of calculated bubble radii from the experimental data smaller than a factor of 2 for the majority of cases. As for the bubble number densities, the agreement with the experimental data is less satisfactory. This suggests that improvements may be needed in particular for the description of bubble nucleation along dislocations. Indeed, the model from [26] yields more evident deviations from the experimental data. For gaseous swelling, indeed, appreciable deviations are found, predominately on a subset of samples (labeled 4135, 4136, and 4140), which are featured by the smallest swelling values in the considered database. It is worth noting that White and coworkers commented these lower values of gaseous swelling as unexpected, however, no justification for these observations was provided.

Figure 2.7 illustrates results specific to a case chosen among those analyzed in this work, i.e. sample 4005–A. The evolution of bubble pressure during the ramp test is shown in Figure 2.7a: the initial rise due to the temperature increase triggers atom and vacancy absorption, which in turn promotes bubble volume increase. The volume

(a)

(b)
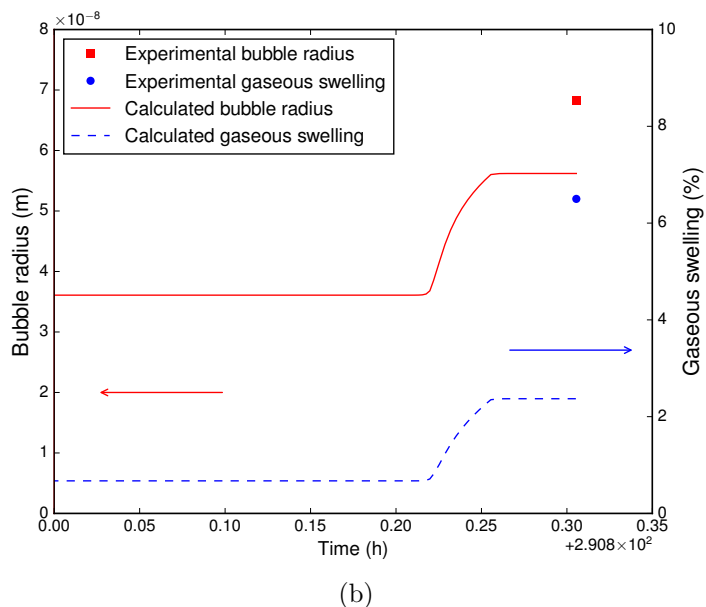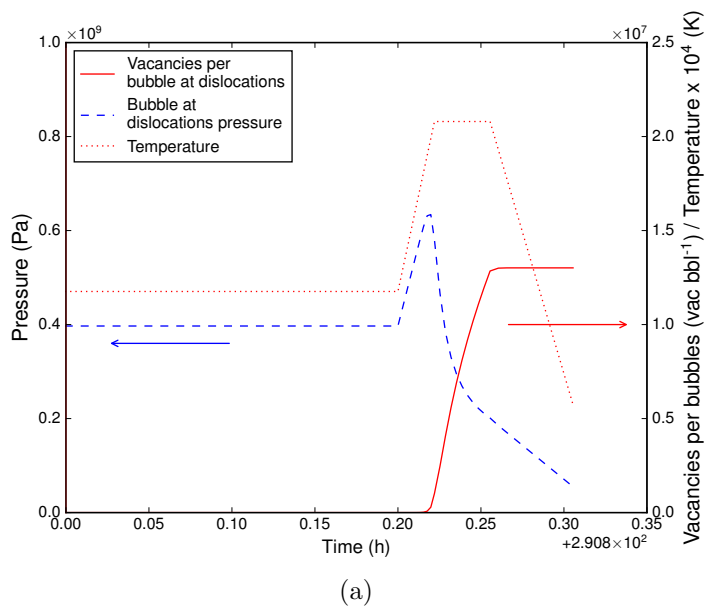
Figure 2.7: Predictions for the evolution of dislocation bubble pressure, number of vacancies (a), radius and associated gaseous swelling (b) during the ramp test for the simulation of the sample 4005–A from [50].

increase corresponds to a decrease in bubble pressure until the beginning of the holding phase (between 0.20 and 0.25h), when the trapping of gas atoms driven by the high temperature causes a small increase of bubble pressure. In Figure 2.7b, bubble coarsening is appreciable in the radius increase, which is a consequence of vacancy absorption and bubble coalescence. Gaseous swelling increases correspondingly.

Table 2.3: Comparison of calculated intra-granular bubble radius and gaseous swelling to experimental data for the analyzed fuel samples from [50]. A total of 40 samples is considered in the present work.

Sample ID	Bubble radius (nm)		Bubble density $\times 10^{-19}$ (bubble m^{-3})		Gaseous swelling (%)	
	Experimental [50]	Calculated	Experimental [50]	Calculated	Experimental [50]	Calculated
4000–A	91.2	77.0	1.38	2.79	4.39	5.35
4000–B	85.6	72.1	1.26	2.90	3.31	4.54
4000–C	73.5	65.9	2.09	3.02	3.7	3.62
4000–D	65.8	55.3	3.39	3.19	4.05	2.27
4004–A	64.4	57.6	3.80	3.16	4.25	2.54
4004–B	68.1	56.4	4.38	3.18	5.8	2.39
4004–C	45.1	52.5	13.8	3.24	5.29	1.96
4004–D	43.5	46.8	10.9	3.31	3.77	1.42
4005–A	68.2	56.2	4.90	3.19	6.5	2.37
4005–B	56.2	54.4	6.77	3.22	5.04	2.17
4005–C	44.1	50.2	15.9	3.27	5.72	1.74
4005–D	29.7	43.4	21.0	3.35	2.31	1.15
4064–A	61.7	73.7	3.77	2.64	3.71	4.43
4064–B	56.9	71.5	4.20	2.68	3.24	4.10
4064–C	62.9	65.4	3.78	2.77	3.95	3.25
4064–D	51.5	55.9	4.82	2.90	2.76	2.12
4065–A	189.9	80.4	0.14	1.77	3.96	3.86
4065–B	174.6	78.6	0.15	1.78	3.28	3.61
4065–C	141.6	74.3	0.25	1.78	2.93	3.05
4065–D	109.9	71.2	0.52	1.77	2.87	2.67
4065–E	45.5	67.7	4.04	1.76	1.59	2.28
4135–A	27.5	67.2	4.09	2.54	0.37	3.22
4135–B	25.2	67.1	3.57	2.54	0.25	3.21
4135–C	21.8	65.1	5.39	2.56	0.25	2.96
4136–A	52	68.4	0.61	2.34	0.35	3.13
4136–B	47.7	67.0	0.75	2.35	0.34	2.96
4136–C	33.6	63.3	1.52	2.37	0.24	2.52
4136–D	25.8	56.4	2.48	2.40	0.18	1.81
4136–E	19.2	48.7	3.37	2.42	0.10	1.17
4140–A	32.2	59.9	1.36	2.44	0.20	2.19
4140–B	24.9	59.0	2.17	2.44	0.15	2.10
4140–C	21.7	55.6	3.28	2.45	0.14	1.76
4162–A	50.6	65.8	5.28	2.09	2.86	2.49
4162–B	36.7	64.7	8.37	2.09	1.73	2.37
4162–C	30.6	61.6	13.5	2.09	1.62	2.04
4162–D	24.6	55.1	18.9	2.06	1.22	1.44
4163–A	76.4	69.3	1.87	1.47	3.49	2.06
4163–B	55.7	68.9	4.14	1.47	3.0	2.01
4163–C	35.6	65.3	10.9	1.44	2.05	1.68
4163–D	26.9	58.9	17.8	1.42	1.45	1.21

2.5 Closing remarks

In this Chapter, I presented a model describing intra-granular fission gas behavior in UO$_2$ that accounts for the bubble coarsening phenomenon under in-pile, high temperature transient conditions, and the corresponding contribution to gaseous fuel swelling. In particular, the model considers the role of dislocations as a source of vacancies and preferential growth along dislocations as the mechanism for bubble coarsening. This theory finds support in the experimental observations showing coarsened bubbles associated with dislocations [50, 57, 58, 65]. It also appears to be a straightforward conceptual extension to dislocation defects of the established behavior at grain boundary defects.

The model extends a previous work published by the authors [26] on intra-granular bubble evolution under normal operating conditions. A multiscale approach was adopted in that the model is informed with parameters derived through atomistic calculations for irradiation-induced re-solution and defect diffusivities. The model combines a mechanistic description of bubble evolution to a limited complexity and is intended for application in engineering FPCs.

The stand-alone model was applied to simulations of local fission gas behavior for the experimental database by White and coworkers. Comparisons to experimental data showed an overall satisfactory agreement between calculated values and experimental data in terms of both bubble radius and associated gaseous swelling, while comparisons in terms of bubble number density were less satisfactory. In particular, sizes of tens to hundreds of nanometers for the coarsened intra-granular bubbles, and volumetric swellings of one to several percent, in these ramp-tested fuel samples were reproduced. These values are orders of magnitude higher than bubbles sizes and swellings observed under normal operating conditions, and could not be captured with traditional models that do not include specific transient capabilities.

The model has been implemented into Idaho National Laboratory's FPC BISON and is going to be made available to TRANSURANUS via its coupling with SCIANTIX. In this framework, the work presented in this Chapter has been presented at the DOE/EURATOM I-NERI 2019 review meeting [137]. Model application to the simulation of other experimental conditions for which bubble coarsening has been observed, such as post-irradiation annealing and high burnup, is left to future work. Future work will also include the application of the model to integral fuel rod thermo-mechanics simulations. Model comparisons to detailed cluster dynamics simulations is also of interest in perspective. Moreover, future improvements may include the coupling to a model for dislocation density evolution under irradiation, and the development of a more detailed model of bubble nucleation at dislocations. Finally, the physics-based approach to the description of intra-granular gas behavior considered in the present model may be applied to other types of oxide fuels, such as U-Pu Mixed Oxides (MOX) fuels both in light water or fast reactor conditions, provided that model parameters are updated to comply with the specific material and reactor peculiarities.

CHAPTER 3. MODELING HIGH BURNUP STRUCTURE IN OXIDE FUELS

"His front wheel struck the edge of the shell, flipped the turtle like a twiddly-wink, spun it like a coin, and rolled it off the highway. [...] But at last its legs waved in the air, reaching for something to pull it over. [...] And as the turtle crawled on down the embankment, its shell dragged dirt over the seeds. The turtle entered a dust road and jerked itself along, drawing a wavy shallow trench in the dust with its shell"

J. Steinbeck, *The Grapes of Wrath*, 1939

Abstract

Local high irradiation damage at low temperatures promotes a restructuring in the original microstructure of nuclear fuels, leading to the formation of High Burnup Structure (HBS). This restructuring strongly affects the thermo-mechanical performance of the overall nuclear fuel rod in both normal operating and accident conditions. Therefore, FPCs need to be provided with proper models accounting for HBS effects. In this Chapter, I present a model describing the HBS formation, the progressive intra-granular xenon depletion in UO_2, and the HBS inter-granular porosity evolution under irradiation. The HBS formation is tackled employing the Kolmogorov-Johnson-Mel-Avrami (KJMA) formalism for phase transformations. The coefficients of the KJMA correlation have been fitted to experimental data on the restructured volumetric fraction as a function of the local effective burnup. To this end, I employed available experimental data and novel data extracted in this work. The HBS formation model is coupled to a description of the intra-granular fission gas behavior, to estimate the evolution of the retained xenon in order to consistently compute fission gas retention and its effect on the fuel matrix swelling. As for HBS porosity collecting the gas diffusing from the grains, its evolution is accounted for exploiting a second-order Fokker-Planck expansion of the cluster-dynamics master equations governing the problem, considering nucleation of pores, gas absorption due to the diffusional flow from the grains, size-dependent re-solution of pores due to their interactions with fission fragments, vacancy absorption, and pores coalescence. Model predictions on xenon local retention, matrix fuel swelling, and porosity evolution are compared to experimental data and to models available in FPCs.

3.1 Introduction

In nuclear fuels, where substantial irradiation damage (e.g., local burnups above 45/50 MWd kg$_U^{-1}$) is accompanied by a limited possibility of recovering the damage (i.e., local temperatures below 1000°C), a dramatic change occurs to the as-fabricated microstructure. The initial microstructure, usually featured by micrometric grain sizes, is gradually replaced by the appearance of sub-micrometric, re-structured grains alongside micrometric pores, of roughly spherical shape. This phenomenon is referred to as High Burnup Structure, or rim effect, since it was historically observed and postulated to be limited to the restructuring observed in the outer region of LWR fuel pellets [51, 138–141]. Indeed, this phenomenon has been observed in fuel types other than UO$_2$, e.g., in Pu-rich islands of heterogeneous MOX fuel [140, 142–144], in the rim zone of FBR U-Pu oxide [145, 146], in U-Pu carbides [147], and in U-Mo fuels [148].

Despite intensive experimental and modeling activities for decades, the formation mechanisms of HBS are still debated [2, 51, 141, 149, 150]. HBS formation is ascribed either to a re-crystallization [79, 129, 151–156] or a polygonization [157–162] process[8]. Indeed, commonly observed features encompass the build-up of dislocations [153], the depletion of intra-granular fission gas [140, 143, 163], the formation of pristine, sub-micrometric grains [159], and development of a novel porosity [93, 164].

The (economically) appealing interest in increasing the target burnup of LWR rods constitutes a strong driving force in developing models describing HBS behavior to be included in FPCs. In fact, the development of HBS porosity brings about an additional fuel swelling source, which must be properly represented to predict UO$_2$ thermo-mechanical performance at high burnups [2, 5]. Moreover, HBS development concurs in determining both thermal conductivity [165] and elastic modulus [166]. Finally, the fission gas stored in HBS porosity plays a major role in determining FGR and fuel fragmentation (and consequent relocation) during Loss of Coolant Accident (LOCA) [167–170] and Reactivity Initiated Accident (RIA) [171] conditions.

Several models, either semi-empirical or mechanistic, have been conceived to describe HBS effects in the framework of FPCs. In the following, I detail the state-of-the-art of models focused on HBS formation, intra-granular fission gas depletion, and on the porosity development available in the open literature, with a special perspective on FPC application.

Lassmann et al. [172] developed a pragmatic, empirical model to account for intra-granular Xe depletion, decreasing its concentration with an exponential law as a function of burnup (not considering by any means the effect of temperature) and needing as an input parameter the HBS formation threshold. This approach represents the legacy treatment of HBS in the TRANSURANUS FPC code [12]. In a recent work, Jernkvist [173] adopted the same concept as the one by Lassmann to describe xenon depletion, while combining it to a threshold value estimated by

---

[8]Re-crystallization entails the formation of sub-grains localized in re-crystallization nuclei in the original grains, and the subsequent growth of re-crystallized sub-grains. On the contrary, the polygonization process is the subdivision of original grains, due to the formation of dislocation cells and subsequent birth of new boundary domains into the original grain volume.

the theoretical model of Rest [174]. The development of HBS porosity is tackled assuming dislocation punching as the driving force, and is described through a simple and pragmatic evolution equation governed by the pore pressure difference with respect to an empirical pressure threshold. The model has been made available to the FRAPCON/FRAPTRAN codes [175]. Lemes et al. [176] extended the model by Lassmann, including the treatment of Kr and complementing it with a mixed empirical and mechanistic description of the porosity development. As for the porosity evolution, the model is a combination of empirical correlations and of the model by Blair and co-workers [177] for considering pore interactions local burnups exceeding 100 MWd kg_U^{-1}. The model is implemented in the DIONISIO code [178].

The model by Khvostov and coworkers [32, 179] describes the HBS restructuring through a Kolmogorov-Johnson-Mel-Avrami (KJMA) relationship, introducing also the idea of "effective burnup" in the description of HBS, i.e., to weight differently the burnup accumulation at high and low temperatures in the description of HBS formation. The semi-empirical description of HBS formation is then paired to a description of pore evolution at grain boundaries. There, the gas diffused from the grains can be accommodated in existing pores or originate new ones, contributing to pore growth together with the trapping of point defects. To this aim, the model considers an increase of point defects diffusivity at grain boundaries, dependent amongst others on the local degree of restructuring. Finally, pore coalescence based on probabilistic considerations and a-thermal fission gas release mechanisms are accounted for. The overall model is grafted in the GRSW-A model [32] and integrated in the FALCON code [180]. The concept of effective burnup was integrated into the Lassmann model by Holt et al. [181], introducing also a more physically-sound temperature threshold in the definition of effective burnup with respect to the one originally proposed by Khvostov. This model is the standard treatment of the HBS formation/depletion in TRANSURANUS, in combination with an empirical (linear) swelling model [182].

Blair and coworkers [177] developed a steady-state model describing the xenon depletion in HBS grains, considering in a physically-sound manner the main intra-granular behavior processes and focusing on the effects of grain boundary diffusivity and re-solution. Moreover, they proposed a model for porosity evolution based on the work by Khvostov and coauthors [179], introducing a scaling factor to grain-boundary diffusivity of non-restructured UO_2 to obtain acceptable results, justified by the increased grain boundary density observed when HBS is formed. The main limits of the model are the lack of description of HBS formation and the steady-state formulation, which prevents its application to transient conditions.

Noirot proposed a model accounting for HBS formation based on an empirical estimation of the dislocation density evolution [33]. In this model, the evolving dislocation density is fitted on the data by Nogita and Une [183]. The size-distribution of dislocation density is assumed to be a square pulse, and two thresholds of dislocation densities are employed to estimate the fraction of HBS restructuring. The porosity evolution is tackled considering a nucleation of pores proportional to the degree of local restructuring, and ascribing pore growth to the absorption of gas diffused from the restructured grains and to vacancy inflow to compensate pore over-pressurization. The phenomena are modeled by the classic formalism of diffusion-limited reactions

in the mean-field approximation. No pore interconnection is considered in the model, whereas a multiplication factor enhancing vacancy diffusivity, similarly to the work by Blair and coauthors [177], is considered. The description is plugged in the MARGARET code, which provides a mechanistic description of fission gas behavior, and is integrated into the ALCYONE code [184, 185].

Pizzocri et al. [186] proposed a semi-empirical model describing HBS formation and xenon depletion, representing HBS development as a progressive shrinkage of the average grain size of fuel from the original micrometric to the sub-micrometric size as a function of the local effective burnup. Xenon depletion is reproduced solving an intra-granular diffusion problem featured by a decreasing domain size, resulting in an accelerated diffusion towards the grain boundaries. The model is available in the SCIANTIX code [52].

Besides the aforementioned empirical and semi-empirical models, more mechanistic models have been developed to describe HBS formation. Rest [174] proposed a mechanistic model considering the evolution of cellular dislocation networks as re-crystallization nuclei and their interaction with intra-granular bubbles. Based on thermodynamics considerations, i.e., comparing the free energies of the original and re-structured phases, he derived a threshold for HBS formation as a function of the local fission density. It must be noticed that the proposed model cannot account for the observed restructuring starting from the grain boundaries and accompanied by the formation of high-angle grain boundary grains [187]. Moreover, a comprehensive description of porosity evolution – holding for non-restructured and restructured fuel – is included [188].

Veshchunov and Shestak [131] proposed a model accounting for the evolution of point, line, and volume defects under irradiation. The key parameter determining HBS formation is the predicted dislocation density, which is compared to a threshold inferred from experimental data [183] to declare HBS formation. Albeit featuring a consistent description of defects evolution, the transition from original to restructured microstructure is step-wise, thus likely failing to properly describe the gradual xenon depletion experimentally observed. Moreover, the assumption of mean-field concentration of vacancies and interstitials might be questionable when applied to HBS, due to high concentrations of defects and sinks. Furthermore, the evolution of HBS porosity is grafted in a more general model holding for UO_2 porosity evolution under different conditions [189], and considers the pore interaction with vacancies and gas atoms diffusing from the grains. Yet, the growth of pores is ascribed to vacancy precipitation and was the object of further publications [37, 189, 190]. In the latest work, the authors propose dislocation punching as the leading mechanism for pore growth at high burnups. Moreover, they account for the pore coarsening observed at ultra high burnups via a triple collision interconnection model, considering a polydispersed pore distribution. The model is available in the MFPR code [31].

Whereas the previous models deal mostly with UO_2, combining the predictions by ALCYONE and image analysis techniques, Bouloré et al. [144] developed a probabilistic model to estimate HBS formation in MIcronized MASterblend (MIMAS) MOX fuel for LWRs, based on xenon Electron Probe Micro Analysis (EPMA) measurements. This model allows estimating the portion of restructured fuel at a certain burnup, as well as the retention of fission products in the HBS region. This

work is a unique model in the open literature of application of HBS modeling in MIMAS MOX fuel.

In this work, I propose a novel model describing HBS formation, intra-granular xenon depletion, and porosity evolution. The HBS formation – i.e., the increase of fuel volume that underwent restructuring as a function of the local effective burnup – is described through the KJMA formalism for phase transitions [191, 192]. I derived the coefficients of the KJMA expression fitting the functional form to experimental data on the restructured volume fraction as a function of the local effective burnup. The data employed are a combination of available data in the literature [193] and novel data on UO_2 I extracted through image analysis and fuel performance simulations of recently published experimental results [187]. The HBS formation is paired to a mechanistic model describing intra-granular fission gas behavior in presented in Chapter 2, providing the evolution under irradiation of the intra-granular bubble population, accounting for bubble nucleation, gas atom trapping into and irradiation-induced re-solution from bubbles, along with diffusion to the grain boundaries. Estimating the evolving concentrations of retained gas into the grain allows us to consistently calculate the fuel matrix swelling, i.e., the swelling due to solid fission products and to inert fission gas atoms found in the fuel matrix and in intra-granular bubbles, up to high burnups. The porosity evolution is tackled considering a Fokker-Planck approximation of the master equations governing the gas evolution at grain boundaries. The Fokker-Planck expansion yields a model featured by a limited number of equations, tracking the evolution of pore average size, pore-distribution variance, pore number density, yet considering in a mechanistic fashion the phenomena determining pore evolution, i.e., irradiation-driven re-solution and gas trapping. Because the pores are generally over-pressurized, I consider the vacancy absorption by the pores as a further mechanism of growth, together with the immobile pores coalescence by interconnection and impingement. I implemented the model in the stand-alone, open-source, meso-scale computer code SCIANTIX [52], which is described thoroughly in the Appendix to this thesis.

I present the stand-alone validation of model predictions, comparing the predicted xenon intra-granular concentration as a function of local burnup to available EPMA data [140, 143, 163] and to a number of models available in the open literature and meant for application in FPCs [172, 176, 186]. I showcase the capabilities of the developed modeling approach to account for the experimentally observed modification of fuel matrix swelling as HBS forms. In particular, I compare the results obtained considering the present model to the experimental data by Spino and coauthors [101]. Finally, I compare the model predictions in terms of pore number density, average radius, and resulting swelling to the experimental data by Cappia and co-workers [164], as well as to models available in FPCs. The comparison to more refined and mechanistic models, e.g., the model by Veshchunov and co-workers available in the MFPR code [37, 131, 190], is of sure interest in perspective, but is left as a part of an extensive comparison between the SCIANTIX and MFPR codes.

The presented model features several originalities. First, it represents HBS formation due to polygonization in a continuous and smooth manner as a function of the local effective burnup, and consistently accounts for the intra-granular fission gas behavior during the formation process. The consistent description of the kinetics

of intra-granular fission gas behavior and fuel gaseous swelling, together with the formulation grounded on a physical basis – for both grain subdivision and fission gas depletion – results in a model which founds a wider applicability, in terms of operating conditions and fuel types, than state-of-the-art models conceived for fuel performance codes. Second, it provides a description of HBS porosity whose foundations lie on the master equations of cluster dynamics. This allows including the effects due to the pore size distribution on the trapping and re-solution rates, constituting a step forward with respect to the available single-size models [32, 33, 177, 188, 189] in both degree of the physical description and the resulting, intrinsic preparedness of the model for application to different operating conditions. These aspects are combined to the needs of models to be included in fuel performance codes by industries and research, i.e., ensuring an acceptable computational burden and an optimal numerical stability. Finally, the inclusion of the developed model in the SCIANTIX code will make it available as an open-source tool to the interested public.

The outline of the Chapter is hereafter briefly outlined. In Section 3.2, I present the extraction of new data on HBS formation, which are exploited in Section 3.3, where I present the formulation of the model for HBS formation and intra-granular depletion. The model tackling the porosity evolution is presented in Section 3.4. The comparison to experimental results and available model predictions are presented in Section 3.5, whereas I draw the conclusions in Section 3.6.

3.2   Derivation of data on High Burnup Structure formation

In this Section, I present the extraction of novel data on the progressive formation of HBS based on the experimental results by Gerczak and coauthors [187]. In particular, I are interested in quantifying the restructured portion of fuel volume and correlating it to the local effective burnup. As a complementary and independent data-set, I report the experimental results on HBS-restructured volume fraction available in the open literature, and published by Noirot and coauthors [193].

3.2.1   Simulation of the analyzed fuel sample

The fuel sample considered in [187] was taken from a commercial fuel rod irradiated in the H.B. Robinson Pressurized Water Reactor (PWR). The mother fuel rod characteristics, listed in Table 3.1, together with the irradiation history reported in [187, 194] were used to build the input for a TRANSURANUS [12] simulation. The calculated fuel central and outer temperatures for the analyzed specimen are reported in Figure 3.1, together with the input linear heat rate, as a function of the specimen average burnup.

The calculations of radial burnup and effective burnup exploits the TUBRNP

Table 3.1: Relevant characteristics of the considered fuel rod, taken from [187].

Characteristic	Value/Material
Cladding material	Zircaloy–4
Cladding outer diameter (mm)	10.77
Cladding inner diameter (mm)	9.25
Pellet-cladding gap (µm)	95
Pellet diameter (mm)	9.06
Pellet height (mm)	6.93
Dish volume (%)	1
^{235}U enrichment (%)	2.9
Active fuel height (mm)	3660
Fuel pin height (mm)	3860
Specimen (radial average) burnup (MWd kg$_U^{-1}$)	72
Measured Fission Gas Release (%)	2.1

burnup model of TRANSURANUS[9] [172, 195] and are reported in Figure 3.2 as a function of the relative pellet radius. The effective burnup is a concept introduced by Khvostov and coauthors [179] to account for the build up of irradiation damage at "low temperatures", i.e., at temperatures at which defects annealing is suppressed. In this work, rather than adopting the original formulation as proposed in [179], I chose the definition of effective burnup as proposed more recently by Holt and coauthors [181]

$$bu_{eff} = \int f(T - \bar{T}) dbu \tag{3.1}$$

where $f(\bar{T})$ is the Heaviside step function, T (°C) the local temperature, and $\bar{T}$ is a threshold temperature assumed equal to 1000°C. The estimation of the local (effective) burnup would allow us to complement the information regarding the analyzed experimental data, i.e., providing each analyzed radial position with the corresponding burnup value.

3.2.2 Extraction of novel data on HBS volume coverage

Gerczak and coworkers [187] investigated the HBS formation through advanced electron microscopy techniques. In particular, their analysis was focused on the correlation between progressive polygonization and grain boundary surfaces orientations. They showed how low-angle grain boundaries form starting from intra-granular patches and/or from the original high-angle grain boundaries of the as-fabricated

---

[9]The version of the code employed in this work is the v1m3j18.
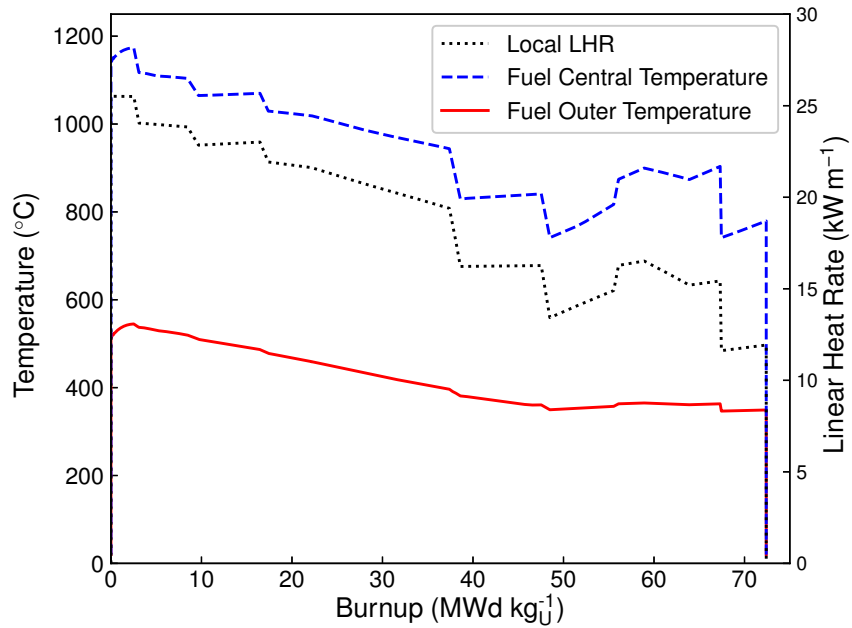
Figure 3.1: LHR and calculated fuel pellet outer and central temperatures as a function of burnup for the considered specimen.
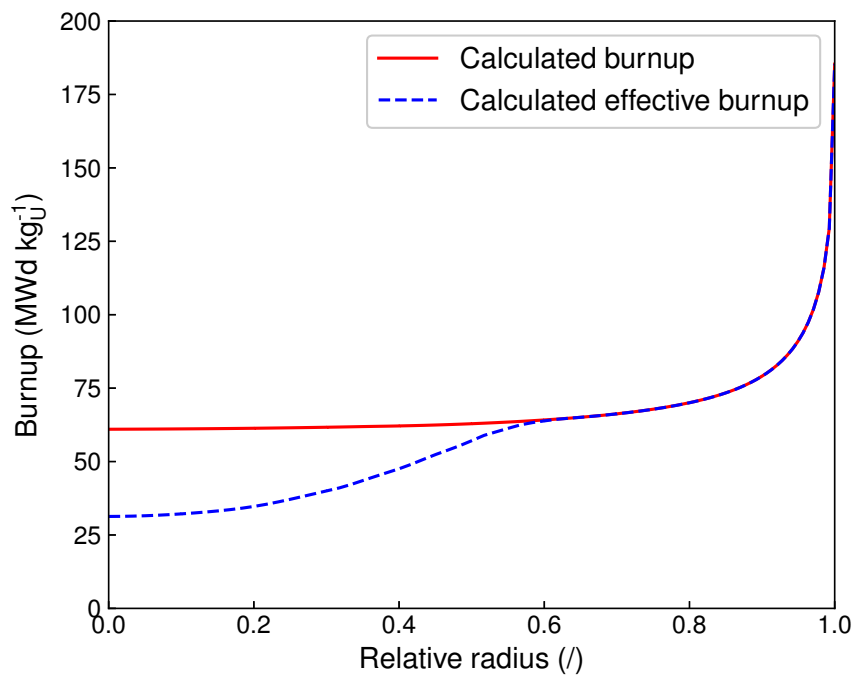
Figure 3.2: TRANSURANUS estimation of local and effective burnup as a function of the relative radial position for the considered fuel pellet.

Table 3.2: Measured fraction of re-crystallized area, estimated volumetric fractions and local burnup in the selected locations from the work by Gerczak et al.[187]. The effective and local burnup in the considered radial positions coincide, as shown in Figure 3.2.

Relative radius (/)	Effective burnup (MWd kg_U^{-1})	HBS-covered area (/)	(Estimated) HBS-covered volume (/)
0.63	64.7	0.15	0.22
0.82	71.2	0.41	0.54
0.94	88.4	0.54	0.69
0.95	90.8	0.61	0.76
0.99	129.4	1.00	1.00

microstructure. Moreover, they showed that low-angle grain boundaries are gradually transforming into high-angle grain boundaries moving towards the pellet periphery, i.e., where HBS development is complete. In the aforementioned work, the authors reported Electron Backscatter Diffraction (EBSD) scans of a fuel pellet microstructure, taken at various distances from the pellet outer radius.

In this work, I present the results of further image analysis applied to the aforementioned experimental results, to quantify the HBS surface and volumetric coverage in the examined samples. The image analysis has been performed on the images taken from Figure 10 of the mentioned paper [187], and reported in Figure 3.3 for the sake of completeness. I considered a subset of the reported images, focusing on the data obtained at relative radii equal to 0.63, 0.82, 0.94, and 0.95. I assume the image at 0.99 relative radius as representative for the complete restructuring process. This assumption is corroborated by the observed grain size, whose measurement yields approximately 200 nm, roughly corresponding to the observed, asymptotic grain size in the HBS [93, 159].

I measured the area covered by HBS in the analyzed locations by the ImageJ software. In particular, I converted to a binary image each analyzed image and quantified the area enclosed by low- and high-angle grain boundaries in the visible sub-domains. The ratio of the selected area to total area of the sample – having discarded the voids and visible porosity – results in the local HBS surface coverage. The results are collected in Table 3.2, in which I report also an estimation of the volumetric fraction and the estimation of the local effective burnup according to TRANSURANUS predictions.

As for the data presented in the work by Noirot et al. [193], the results considered in this work refer to post irradiation examinations of a standard-grain, UO_2 disc irradiated in the Halden Reactor up to an average burnup level of 76 MWd kg_U^{-1}. The specifications of the fuel manufacturing, as well as the irradiation conditions are reported in [193, 196]. As the irradiation temperature of the sample is presumed to be below 1000°C throughout the whole irradiation [193, 196], the local burnup estimation is a direct measurement of the effective burnup defined by Eq. 3.1.

To estimate the burnup as function of the radial position, I employed the information reported in [193] about the sample irradiation, namely

(a) r/r$_o$ ~ 0.99

15 um

(b) r/r$_o$ ~ 0.95

15 um

(c) r/r$_o$ ~ 0.94

15 um

(d) r/r$_o$ ~ 0.82

15 um

(e) r/r$_o$ ~ 0.63

15 um

(f) r/r$_o$ ~ 0.44

15 um

(g) r/r$_o$ ~ 0.35

15 um

LAGBs from 2-5° are shown in green, LAGBs 5-15° in yellow, and HAGBs 15-65° in purple.

	Min	Max
purple	15°	65°
yellow	5°	15°
green	2°	5°
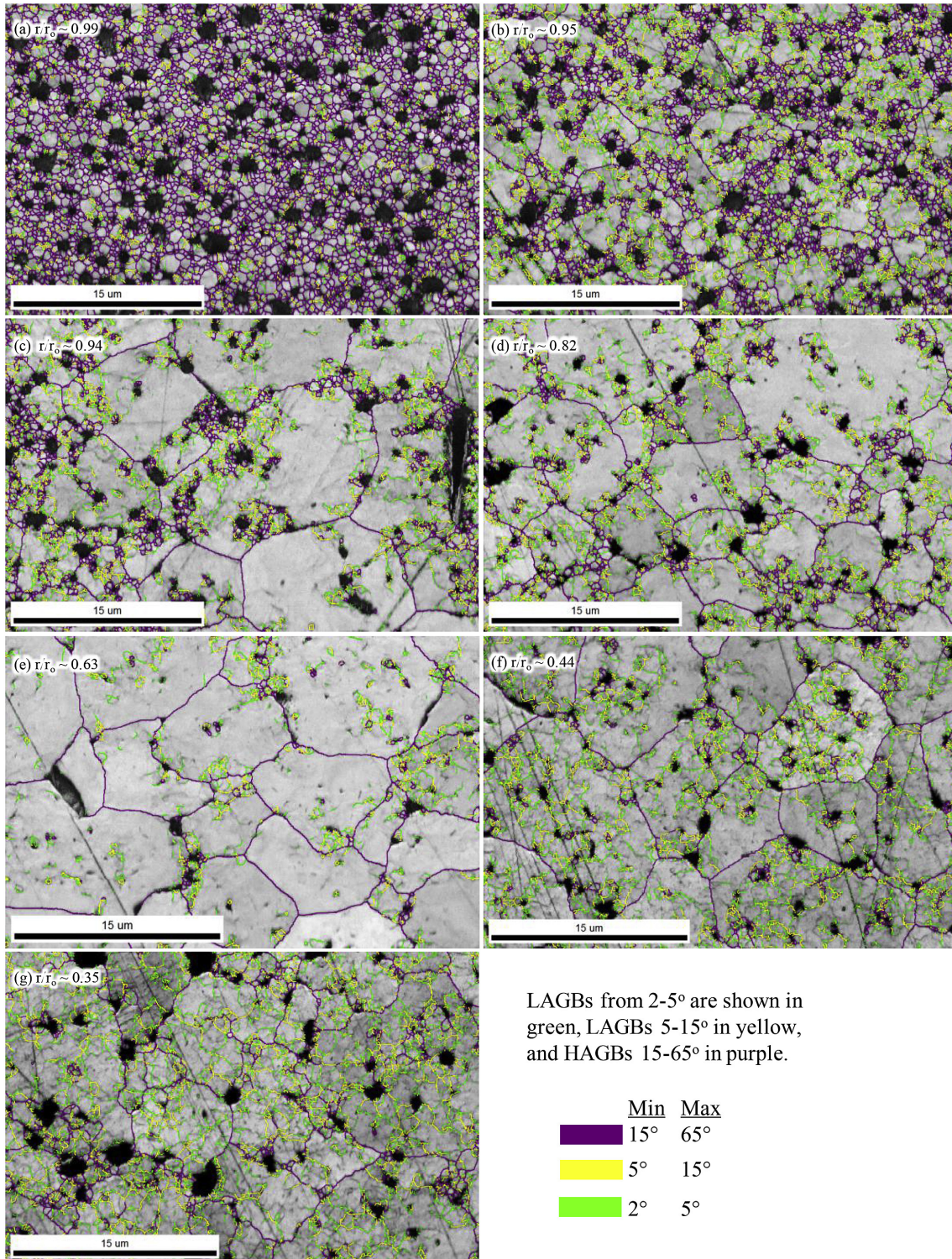
Figure 3.3: Grain boundary misorientation map overlaid on image quality map for locations r/r$_0$ 0.99 to 0.35, (a) through (g). Taken from [187].

Table 3.3: Measured fraction of re-crystallized area, estimated volumetric fractions and local burnup in the selected locations of the sample taken from [193].

Relative radial position (/)	Effective burnup (MWd kg$_\text{U}^{-1}$)	HBS-covered area (/)	(Estimated) HBS-covered volume (/)
0.30	72.4	0.41	0.55
0.66	77.3	0.46	0.60
0.97	83.8	0.49	0.62

(i) the average burnup of the sample is equal to 76 MWd kg$_\text{U}^{-1}$, and

(ii) the burnup at the periphery of the sample is 19% higher than in the center,

to carry out a constrained numerical optimization[10] estimating the burnup at the considered radial positions of the sample. The results of the optimization, in terms of local burnups, together with the experimental data on HBS covered area reported in [193] and estimated volumetric fractions are reported in Table 3.3.

3.3 Formulation of the model for High Burnup Structure formation and fission gas depletion

In this Section, I detail the formulation of the model accounting for HBS formation and intra-granular fission gas behavior. The development of HBS is described through a semi-empirical model, linking the fraction of restructured fuel to the local effective burnup. I employed the data derived in Section 3.2 to derive this model. On the other hand, the behavior of intra-granular fission gas in the restructured volume is described via an available model in the open literature [26]. This model has been tailored for HBS modeling and integrated with the description of HBS restructuring.

3.3.1 Modeling HBS formation

I employed the data extracted from [187, 193], presented in Section 3.2, to fit an expression for the HBS formation rate as a function of effective burnup. In particular, I chose the functional form of the Kolmogorov-Johnson-Mehl-Avrami formalism, which is suitable to model generic restructuring phenomena and phase transitions.

The KJMA approach has been already proposed in HBS modeling [179, 192], relying on the original formulation by Kolmogorov [191], reading

$$\alpha_r = 1 - \exp\{-K_A \cdot t^{\gamma_A}\} \tag{3.2}$$

---

[10]The method I chose to carry out the optimization is the Generalized Reduced Gradient method implemented in the Excel solver, using as guess solutions the average burnup.
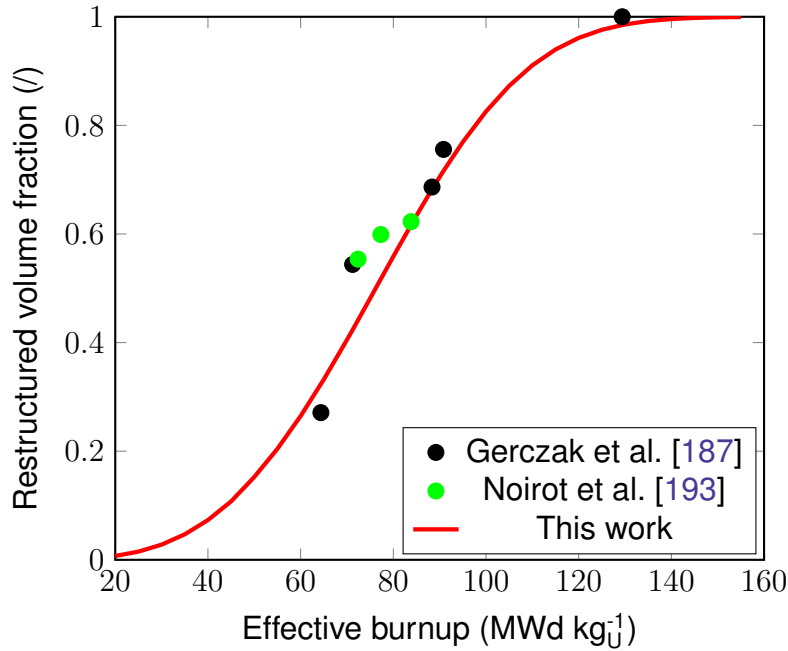
Figure 3.4: Experimental measurements derived from [187, 193] on the fraction of restructured fuel volume and KJMA relationship as a function of local effective burnup.

where α_r (/) is the restructured volume fraction, K_A (s$^{-\gamma}$) is the transformation rate constant, γ_A (-) is the so-called Avrami constant, and t (s) the time. It is interesting to notice that a similar expression has been adopted by Bouloré and coworkers [144] to evaluate the HBS restructuring rate in MIMAS uranium-plutonium mixed oxide fuel, based on statistical considerations.

In this work, I preserve the functional form of the KJMA relationship, whereas I considered the local effective burnup in place of the time and determined the two constants – K and γ – by a least-square fitting of the experimental data presented in Table 3.2 and 3.3. The fitting procedure yields $K_A = 2.77 \times 10^{-7}$ and $\gamma = 3.35$, expressing the effective burnup in MWd kg$_U^{-1}$[11], namely

$$\alpha_r = 1 - \exp\left\{-2.77 \times 10^{-7} \cdot (bu_{eff})^{3.35}\right\} \tag{3.3}$$

The experimental data, together with a plot of the resulting correlation, are shown in Figure 3.4.

It must be noticed that, although resulting from a fitting procedure, the coefficients I derived for Eq. 3.2 retain a physical meaning, which is a direct consequence of the KJMA theoretical formulation [197]. In fact, the value of the power to which the burnup variable is taken (i.e., the Avrami constant, γ_A) provides information about

---

[11]I carried out a linear fitting taking the natural logarithm of Eq.3.2, obtaining a coefficient of determination for the regression (R^2) equal to 0.81.

the nature of the phase transition. A transformation featured by a constant, bulk nucleation rate of the second phase – in the present work, HBS is representing the second phase – and by a bulk growth has a power equal to 4 [197]. On the other hand, if the nucleation sites are preformed, or if transformation happens on grain boundaries in presence of a constant nucleation rate, the power is equal to 3 [197].

In this work, I obtain from the fitting procedure an Avrami constant between 3 and 4. This value advocates a mixed nature of the transformation, i.e., with contributions from bulk nucleation and growth, and from bulk growth from preformed sites combined to a transformation occurring at grain boundaries. In the work by Khvostov and coauthors [179], the Avrami constant was taken equal to 3, i.e., only the latter mechanism was considered. The presence of this mechanism is corroborated by experimental observations and theoretical predictions [79, 93, 150]. This would not account for the formation of HBS following intra-granular patches, which has also been reported in several experimental works [140, 150, 162, 193]. Indeed, the value obtained in this work accounts for all the mentioned contributions, being adherent to the different experimental findings.

For the sake of completeness, I discuss the validity of the hypotheses underlying the KJMA formalism for phase transformation, namely, constant temperature during the transformation, random and homogeneous formation of secondary phase nuclei. The experimental data considered in this work [187], coherently with other recent results [198], corroborate the hypothesis of homogeneous formation of the HBS grains in the original microstructure volume, whereas the random disposition of the nuclei is questionable. In fact, the grain boundaries of the as-fabricated microstructure, as well as the intra-granular fission gas bubbles, appear to be a preferred source for the formation of grain sub-domains. As for the hypothesis of constant temperature, the assumption is holding in the sense that, introducing the effective burnup as defined in Eq. 3.1, all the temperatures below this threshold count in the same way to determine the time of the transformation (i.e., the effective burnup).

3.3.2   Modeling fission gas depletion in the HBS

As the model is conceived to be included in fuel performance codes, I adopt the classical representation employed in such codes to describe fission gas diffusion, i.e., I represent the single grain as an equivalent spherical domain, employing the concept of an "effective" diffusion equation [2, 5, 21, 26, 199].

Equation 3.3 is adopted to evaluate the volume fraction that underwent HBS restructuring. Beside, the model considers a "two phases" material, one pertaining to the original microstructure and one to HBS, as sketched in Figure 3.5. These two "phases" are featured by different grain sizes, i.e., the original microstructure usually by a micrometric size, whereas the HBS is assumed to be formed at a radius equal to 150 nm (in line with experimental data, e.g., by Ray and coworkers [159]). It is worth to underline that this modeling approach can be naturally extended to heterogeneous U-Pu mixed oxide fuels, featured by "regions" with different Pu content, resulting in local higher fission densities along the fuel pellet.

No HBS   HBS

Original grain   Sub-micron grain in HBS
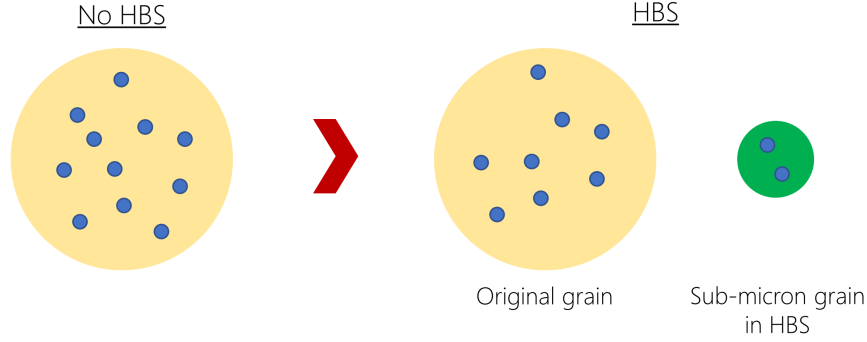
Figure 3.5: Representation of the modeling approach to intra-granular fission gas behavior accounting for HBS progressive formation, which introduces a second type of (much smaller) grains.

In both domains, the intra-granular gas behavior is described through the mechanistic model presented by Pizzocri and coauthors [26]. This model allows for the calculation of intra-granular fission gas bubble nucleation, growth due to gas atom trapping, destruction due to the interaction with fission fragments, along with considering a net diffusion of gas atoms towards the grain boundaries. The equations – which are applied in both the original and HBS domains – read

$$
\begin{cases}
\dfrac{\partial c}{\partial t} = D\nabla^2 c - g_n c + b_n m - 2\nu + y\dot{F} \\[2mm]
\dfrac{\partial m}{\partial t} = 2\nu + g_n c - b_n m \\[2mm]
\dfrac{\partial N}{\partial t} = \nu - b_n N
\end{cases}
\tag{3.4}
$$

where D $(\mathrm{m^2\,s^{-1}})$ is the single gas atoms diffusion coefficient, c (at m^{-3}) is the concentration of gas retained in dynamic solution, m (at m^{-3}) is the concentration of gas in the bubbles, N (bubble m^{-3}) is the bubble number density, g_n (s^{-1}) is the trapping rate, b_n (s^{-1}) is the re-solution rate, ν (bubble m^{-3} s^{-1}) is the bubble nucleation rate, y (atoms per fission) is the fission gas yield, and $\dot{F}$ (fission m^{-3} s^{-1}) is the fission rate density. The average number of atoms in a bubble, n (/), and the associated radius, R (m), and the resulting swelling, $\left(\dfrac{\Delta V}{V_0}\right)_{\mathrm{ig}}$ (/), are defined as

$$
\begin{aligned}
n &= \frac{m}{N} \\[2mm]
R &= (B_{ig} n)^{1/3} \\[2mm]
\left(\frac{\Delta V}{V_0}\right)_{\mathrm{ig}} &= \frac{4}{3}\pi R^3 N
\end{aligned}
\tag{3.5}
$$

where $B_{ig} = (3\Omega/4\pi)^{(1/3)}$ (m) and Ω (m^3) is the volume occupied by a fission gas atom inside intra-granular bubbles in UO$_2$.

Following Speight [200], we adopt the so-called quasi-stationary approach, i.e., I consider trapping and re-solution to be in equilibrium. Thus, I solve for the total gas concentration in the grain $c_t = c + m$ (at m^{-3}) and simplify Eqs.3.4 into

$$\begin{cases} \dfrac{\partial c_t}{\partial t} = D_{eff} \nabla^2 c_t + y\dot{F} \\ \dfrac{\partial N}{\partial t} = \nu - b_n N \end{cases} \tag{3.6}$$

where $D_{eff} = D \cdot b/(b+g)$ (m^2 s^{-1}) is the "effective" diffusion coefficient. It must be underlined that this approach, i.e., solving a single equation considering an "effective" diffusion coefficient (Eq.3.6) instead of solving Eqs.3.4, is the approach currently adopted in state-of-the-art fuel performance codes [2, 5] and holds in the majority of normal-operating and accident conditions [201]. However, it presents limitations in modeling rapid transients to relatively high temperatures such as postulated reactivity-initiated accidents (RIA) [201].

As HBS is progressively forming, two intra-granular problems are solved, one for each "phase", considering two different integration domains, characterized by their own grain size (e.g., micrometric in the as-fabricated region and sub-micrometric in the restructured region). Henceforth, the overall concentration of gas in the considered domain[12], c_t^*, is evaluated as

$$c_t^* = (1 - \alpha_r) \cdot c_t^{NR} + \alpha_r \cdot c_t^{HBS} \tag{3.7}$$

where the superscripts NR and HBS refer to the quantities evaluated solving the intra-granular problem in the non-restructured and HBS sub-domains, respectively. The same concept is applied to estimate each concentration. It is worth noticing that this concept of a weighted average is employed also in the MARGARET code [33]. Eventually, as HBS forms during irradiation, an increasing portion of the material is covered by the restructured microstructure. Thus, I consider a sweeping of gas concentration from the original to restructured region, namely

$$\left.\frac{\partial c_t^{HBS}}{\partial bu_{eff}}\right|_R = \frac{1}{\alpha} \frac{d\alpha}{dbu_{eff}} \left(c_t^{NR} - c_t^{HBS}\right) + \frac{\alpha - 1}{\alpha} \frac{\partial c_t^{NR}}{\partial bu_{eff}} \tag{3.8}$$

where the first term of the right hand side of Eq.3.8 represents the effective gas transfer between the two regions due to restructuring. In deriving Eq.3.8, we made the assumption of splitting the evolution of the intra-granular gas concentrations accounted by Eqs.3.6 from the restructuring effects, which are described by Eq.3.8[13].

---

[12]In engineering-scale fuel performance codes, fission gas behavior models are called in each integration point of the fuel computational mesh (e.g., [5, 12, 53]).

[13]This treatment is conceptually similar to the treatment of the so-called grain boundary sweeping, i.e., the transfer of gas from the interior of the grains to the grain boundaries due to grain growth (e.g., [72]).

Moreover, we assumed that the total concentration of gas in the considered reference volume is conserved during the restructuring.

The combination of increasing HBS volume ratio and smaller grain size of HBS allows for a consistent description of fission gas depletion as HBS is formed. In fact, as the effective burnup builds up, an increasing fraction of the volume is affected by HBS (Eq.3.3). This increases the weight of intra-granular behavior in the HBS sub-domain, which is characterized by a fast diffusion to the grain boundary associated with the sub-micrometric grain size (the diffusion rate being D/a^2).

Rather than attempting to mechanistically describe HBS formation, whose sequence of phenomena is still debated, the presented approach provides a robust model which accounts for HBS formation and gas depletion in a consistent manner, still preserving a degree of complexity in line with FPC requirements.

3.3.3 Modeling fuel matrix swelling

A consistent estimation of fuel matrix swelling, i.e., the swelling due to solid fission product compounds, to fission gas atoms retained in dynamic solution in the matrix, and to the intra-granular fission gas bubbles[14], must account for the evolution of the gas concentrations as HBS forms as described in Section 3.3.2. It is worth noticing that a direct measurement of the solid swelling rate is not feasible, for the interaction with concurrent phenomena taking place in UO_2 under irradiation which affect fuel density variation (such as densification, sintering, and fuel gaseous swelling).

The total matrix swelling[15], $\left(\dfrac{\Delta V}{V_0}\right)_{\mathrm{m}}$ (/), may be expressed as follows

$$\left(\frac{\Delta V}{V_0}\right)_{\mathrm{m}} = \left(\frac{\Delta V}{V_0}\right)_{\mathrm{ig}} + \left(\frac{\Delta V}{V_0}\right)_{\mathrm{s}} + \left(\frac{\Delta V}{V_0}\right)_{\mathrm{sg}} \tag{3.9}$$

where the subscripts "ig", "s", and "sg" refer to the swelling due to intra-granular bubbles (as defined in Eq. 3.5), to the solid fission products, and to the concentration of gas in dynamic solution, respectively. The swelling due to gas in dynamic solution is calculated as

$$\left(\frac{\Delta V}{V_0}\right)_{\mathrm{sg}} = c^* \cdot \frac{a_L^3}{4} \tag{3.10}$$

where c^* is the overall concentration of gas as single atoms retained in dynamic solution with the matrix (i.e., not in intra-granular bubbles) and a_L (m) is the

---

[14]It must be clarified that, in this Chapter, the contribution to matrix swelling due to intra-granular bubbles accounts for the swelling due to nanometric bubbles. The dislocation bubble behavior, outlined in Chapter 2, may originate an additional component of swelling which is not included in the matrix swelling calculation.

[15]The swelling due to HBS porosity is treated separately, in the subsequent part of the Chapter.

UO_2 lattice parameter. In this work, following [98, 202], I assume that fission gas atoms are bounded in UO_2 to a Schottky trio (i.e., a neutral complex of defects made of an uranium and two oxygen vacancies). Thus, the associated increment of volume assigned to every gas atom in dynamic solution is three times the average atomic volume in UO_2, equal to $a_L^3/12$.

As for the swelling due to solid fission products, I rely on the theoretical considerations by Olander [1], who proposed a swelling rate due to fission product compounds not soluble in the UO_2 fluorite structure equal to 0.32% per atom percent burnup. Nonetheless, it must be noticed that solid swelling rate strongly depends on the local chemical speciation, which is governed by the local oxygen potential, whose variation with burnup determines the phases in which elements are found [203]. For example, the previous value obtained by Olander entails considering that all the created Mo is in metallic inclusions, while it is known that as burnup increases Mo can be found as ceramic precipitate or dissolved in the fuel matrix [203], determining higher fuel swelling rates (evaluated by Olander as 0.45% per at.%). A more recent and detailed assessment on the basis of various atomic scale calculations (Middleburg et al. for UO_2 [204], Ducher et al. for UC [205] and Klipfel et al. for UN [206]) accounts for the local environment of each fission product that is also dependent on the evolving stoichiometry.

Although I consider a constant value as a function of burnup, in line with state-of-the-art approaches (such as in the MATPRO FSWELL correlation [175]), a shift towards higher values of the swelling rate would be more adherent to the physical behavior of fission products. Finally, it must be underlined that state-of-the-art models for fuel solid swelling do not take into consideration the contribution brought about by irradiation damage, such as the formation of dislocation loops. This contribution is expected to be significant especially at low burnups and to contribute to the swelling rate decreasing associated with HBS formation and could be assessed by means of an extended version of the MFPR-F code when it would also model the anionic point defects.

3.4 Formulation of the model for High Burnup Structure porosity evolution

In this Section, I present the derivation of a model describing the evolution of inter-granular porosity in the HBS. The model is derived starting from the Cluster Dynamics (CD) master equations governing the inter-granular gas behavior, enforcing a Fokker-Planck expansion in the phase space of the problem (i.e., cluster sizes) to come up with a model tracking the evolution of the three first central moments, i.e., integral pore number density, mean size and variance of the distribution. On top of this, vacancy absorption due to pores over-pressurization and pore interconnection by impingement are accounted for and integrated. Together with the HBS formation and intra-granular model presented in Section 3.3, this model provides an integral description of FGB in the HBS, ready to be included in FPCs.

3.4.1   Fokker-Planck approximation of CD master equations

In order to describe the evolution of HBS pores, I employ a cell model (e.g., [28, 135]), i.e., a regular 3D array of spherical Wigner-Seitz cells is associated to the pore pattern. A 2D sketch of the representation is provided in Figure 3.6. The evolution of HBS pores is described by the master equations of cluster dynamics (e.g., [68, 207, 208]) which accounts for the phenomena of pore nucleation, re-solution, gas precipitation from the grain boundaries – as sketched in Figure 3.7. In the following, I assume that re-solution events lead to the destruction of the pore (i.e., an *heterogeneous* re-solution modeling approach). The formulation of the master equations reads

$$
\begin{cases}
\dfrac{\partial c_{gb}}{\partial t} = \kappa - 2\nu_P - \displaystyle\sum_{n=2}^{\infty} \beta_n c_n + \sum_{n=2}^{\infty} n\alpha_n c_n \\[2ex]
\dfrac{\partial c_2}{\partial t} = \nu_P - \alpha_2 c_2 \\[2ex]
\dfrac{\partial c_3}{\partial t} = \beta_2 c_2 - \alpha_3 c_3 \\[1ex]
\vdots \\[1ex]
\dfrac{\partial c_n}{\partial t} = \beta_{n-1} c_{n-1} - \alpha_n c_n
\end{cases}
\tag{3.11}
$$

where c_{gb} (at m^{-3}) is the gas concentration at the grain boundaries, c_2, c_3,...,c_n (at m^{-3}) are the number density of pores containing 2,3,..n atoms, κ (at m^{-3} s^{-1}) is the gas arrival rate from the interior of the grains, ν_P (pores m^{-3} s^{-1}) is the pore nucleation rate, β_n and α_n (s^{-1}) represent the probability of gas precipitation into and re-solution from HBS pores. The expression of the HBS pore re-solution rate
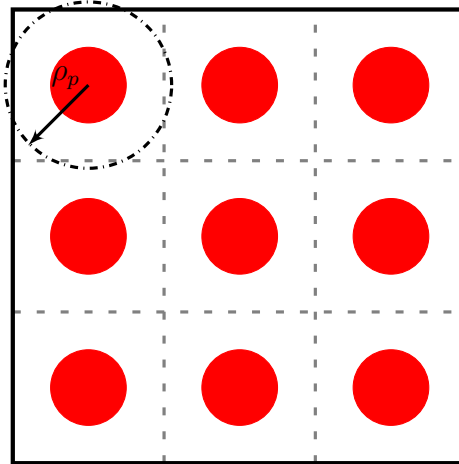
Figure 3.6: Sketch of the model employed in this work to represent HBS pore growth, based on [28].
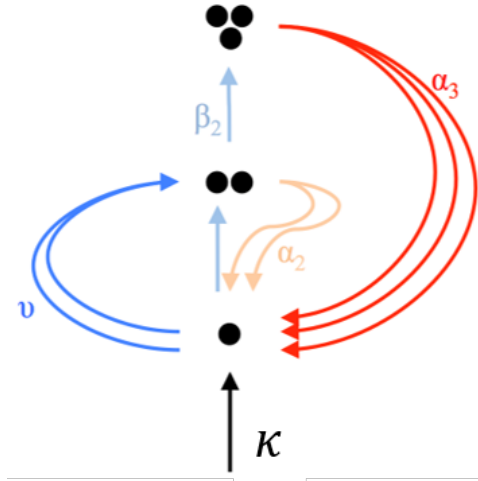
Figure 3.7: Schematization of the phenomena accounted by the CD master equations.

is taken from Veshchunov and Tarasov [23] and considers a size-dependent process, namely

$$\alpha_n = 2 \cdot 10^{-23} \dot{F} \left(\frac{3d_V}{3d_V + R_n^P} \right) \left(\frac{\delta_V}{\delta_V + R_n^P} \right) \tag{3.12}$$

where R_n^P (m) is the radius of a cluster (pore) containing n atoms, d_V (m) is the critical distance from the pore surface allowing atom re-solution, and δ_V (m) is thickness of the re-solution layer around the pore. It should be noticed that the present model does not consider a re-solution back into the grains of the gas atoms ejected from HBS pores. Whereas this assumption might be questionable when considering standard grain size fuel, HBS fuel is featured by such small (i.e., hundreds of nanometers) grains that the gas atoms would be re-soluted very close to the grain boundaries. One might consider those gas atoms as already affected by the grain boundary diffusion, thus always on the grain boundaries.

Following Gosële [209], I evaluated the precipitation rate of gas atoms from the grain boundaries into the pores as

$$\beta_n = 4\pi D_{gb}^{SA} c_{gb} R_n^P \left(1 + 1.8\xi^{1.3} \right) \tag{3.13}$$

being D_{gb}^{SA} (m^2 s^{-1}) the grain-boundary diffusivity of single gas atoms. The original formulation by Ham [105] was corrected by Gösele [209] to account for the competitions between sinks on the precipitation rate. In fact, the local porosity ξ (/) – considering spherical pores – is evaluated as

$$\xi = \frac{4\pi}{3} N_p \left(R_{\bar{n}}^P \right)^3 \tag{3.14}$$

where the total number density of pores, N_p (pores m^{-3}), is defined as

$$N_p = \sum_{n=2}^{\infty} c_n \tag{3.15}$$

and $R_{\bar{n}}^P$ is the number-averaged radius of the distribution. As for the nucleation rate, in the light of the great uncertainties associated to this parameter (e.g., [56, 75]), I chose not to model it explicitly. Rather, I consider it as proportional to the local restructuring rate, i.e., to the derivative of Eq. 3.3 with respect to the local effective burnup. The proportionality constant is a model parameter. Finally, given the appreciable shift in the tilt angle of grain boundaries observed during the HBS formation [187, 198] – which can be ascribed to primary recrystallization [129, 152, 153] – I introduce a preliminary modification of the diffusion coefficient of gas atoms (and vacancies) at grain boundaries. Based on the information extracted from the experimental work of Gerczak and co-workers [187] and reported in Figure 3.3, and considering the dependence of the grain boundary diffusion coefficient on the tilt angle proposed by Peterson [210], I propose the following correction for the grain boundary diffusion coefficient of atoms and vacancies

$$D' = D'(T) \cdot \frac{\sin\left[4° \cdot (1 - \alpha_r) + 40° \cdot \alpha_r\right]}{\sin(4°)} \tag{3.16}$$

where D' is the gas atom or vacancy diffusion coefficient at the grain boundaries, and the correction term considers a weighted average between the average tilt angle observed in the non-restructured region (i.e., 4°) and the average tilt angle observed in the fully restructured region (i.e., 40°). This modification allows for an enhanced diffusivity of species at grain boundaries and the correction factor spans roughly between 1 and 10, at beginning and end of restructuring, respectively. The modification is consistent with the conclusions of the analyses on gas behavior in the HBS by Baron and co-workers [211] and by Blair and co-workers [177], although they proposed an enhancement of the diffusivity about two and four orders of magnitude, respectively.

Since the solution of Eq. 3.11 is unpractical for application to FPCs [207, 208], I focus on the evolution of the first three central moments of the cluster distribution instead of solving the set of (hundreds of) thousands of coupled equations given by 3.11. In particular, in addition to the integral of the pore size distribution, N_p, I consider the following two quantities

$$A = \sum_{n=2}^{\infty} c_n n$$

$$\tag{3.17}$$

$$B = \sum_{n=2}^{\infty} c_n \left(n - \bar{n}\right)^2$$

which are related to the mean and variance of the distribution, $\bar{n}$ and M^2, by

$$
\bar{n} = \frac{A}{N_p}
$$

$$
M^2 = \frac{B}{N_p}
$$

(3.18)

To express the time evolution of the quantities appearing in Eqs. 3.17 and following Clement and Wood [207], I consider a second order Fokker-Planck expansion of the coefficients of Eqs. 3.11 in the phase space of the problem, i.e., with respect to the cluster size, reading

$$
\alpha_n \approx \alpha(\bar{n}) + \left.\frac{\partial \alpha_n}{\partial n}\right|_{\bar{n}} (n - \bar{n}) + \frac{1}{2}\left.\frac{\partial^2 \alpha_n}{\partial n^2}\right|_{\bar{n}} (n - \bar{n})^2
$$

$$
\beta_n \approx \beta(\bar{n}) + \left.\frac{\partial \beta_n}{\partial n}\right|_{\bar{n}} (n - \bar{n}) + \frac{1}{2}\left.\frac{\partial^2 \beta_n}{\partial n^2}\right|_{\bar{n}} (n - \bar{n})^2
$$

(3.19)

Combining Eqs. 3.11, 3.17, and 3.19, one obtains the following simplified model, able to estimate the evolution of the distribution (number-averaged) mean size and variance, together with pore number density and gas stored at grain boundaries[16]

$$
\begin{cases}
\dfrac{\mathrm{d}N_p}{\mathrm{d}t} = \nu_P - \alpha_{\bar{n}} N_p - \dfrac{1}{2}\alpha'' B \\[2ex]
\dfrac{\mathrm{d}A}{\mathrm{d}t} = 2\nu_P + \beta_{\bar{n}} N_p - \alpha_{\bar{n}} N_p - \alpha' B + B\left(\dfrac{\beta''}{2} + \bar{n}\alpha''\right) + \dfrac{\bar{n}^2}{2}\alpha'' A \\[2ex]
\dfrac{\mathrm{d}B}{\mathrm{d}t} = \beta_{\bar{n}} N_p - \alpha_{\bar{n}} N_p + B\left(2\beta' + 3\alpha'\bar{n}\right) - 3\bar{n}B(\beta'' + \alpha'') + \\[2ex]
+ \dfrac{B}{2}\left(1 - 2\bar{n}\right)\beta'' - \bar{n}^2\beta'' A - \dfrac{3}{2}\bar{n}^3 A\alpha'' + \nu_P\left(\bar{n} - 2\right)^2 \\[2ex]
\dfrac{\mathrm{d}c_{gb}}{\mathrm{d}t} = \kappa - \dfrac{\mathrm{d}A}{\mathrm{d}t}
\end{cases}
$$

(3.20)

The formulation of the model constituted by Eqs. 3.20 embraces the fundamental physical phenomena governing the gas transfer to the HBS pore under irradiation and during restructuring, i.e., gas diffusion from the interior of the grains, atoms re-solution, and gas atoms trapping. This is in-line with available models conceived for FPC application (e.g., [33]). The novelty of the model I propose in this work lies

---

[16]In the following, the first and second derivative of the parameters with respect to the cluster size will be indicated, e.g., focusing on the re-solution parameter, as α' and α'', respectively.

in the intrinsic consideration of the effects brought about by the evolution of the pore-size distribution. In fact, these effects are embedded in the derivatives of the re-solution and trapping parameters through the Fokker-Planck expansion. Albeit not calculating the complete pore-size distribution, the Fokker-Planck expansion is known to be a satisfactory approximation when the cluster size is large [71] – which is the case of developed HBS porosity. Moreover, the presented model allows for tracking the evolution of the distribution mean size and variance, thus one can assume a certain shape of the pore-size distribution (e.g., log-normal [164]) and compute the evolution of the distribution under irradiation. This feature results as a unique capability offered by the present model for HBS modeling in FPCs, and was proved to be a necessary condition for the correct estimation of HBS pore fracturing under LOCA conditions [212].

3.4.2 Pore size calculation

HBS pores are strongly over-pressurized [140, 196, 213], mainly because of the substantial inflow of fission gas atoms coming from the depleted HBS grains. Thus, they will tend to relieve the pressure by absorbing vacancies by the surrounding medium. A consistent treatment of the vacancy absorption mechanism would require extending the master equations exposed above to a two reacting species CD model. This extension – which is pursued in other fields or by dedicated CD tools [68, 71] – would hinder the applicability of the Fokker-Planck procedure exposed above, calling for a multidimensional Fokker-Planck expansion whose computation would increase the computational burden significantly. Thus, I chose to model the vacancy absorption as it was governed by the mean size of the distribution, rather than consider it, class by class, in the master equations. This is in turn affecting the moments calculation, since the average pore radius is needed in Eqs.3.19-3.20 and depends on the number of vacancies calculated as follows. Albeit being a simplification of the full procedure, the developed approach allows estimating the vacancy absorption in a grounded manner and results in-line with the single size model described by Eqs. 3.20.

As discussed above, I assume HBS pore to be spherical. Thus, the mechanical equilibrium size is set by the following capillarity relationship

$$p_{eq}^P = \frac{2\gamma}{R_{\bar{n}}^P} - \sigma_h \qquad (3.21)$$

where p_{eq}^P (Pa) is the equilibrium pressure, γ (J m^{-2}) is the surface energy, and σ_h (Pa) is the hydrostatic stress (considered negative if the medium is under compression). Since pores are in non equilibrium, they tend to equilibrate absorbing or emitting vacancies. The rate of variation of pore volume is defined via

$$\frac{\mathrm{d}V_{\bar{n}}^P}{\mathrm{d}t} = \omega \frac{\mathrm{d}\bar{n}}{\mathrm{d}t} + \Omega \frac{\mathrm{d}n_{vp}}{\mathrm{d}t} \qquad (3.22)$$

where $V_{\bar{n}}^P$ (m^3) is the pore volume, ω (m^3) is the atomic volume for xenon, and Ω (m^3) is the vacancy volume. The content of gas atoms is calculated solving Eqs. 3.20, whereas the vacancy absorption/emission rate $\mathrm{d}n_{vp}/\mathrm{d}t$ is calculated as [114]

$$\frac{\mathrm{d}n_{vp}}{\mathrm{d}t} = \frac{2\pi D_{gb}^v \rho_P}{k_B T \zeta}(p^P - p_{eq}^P) \tag{3.23}$$

where n_{vp} (/) is the number of vacancies per pore, D_{gb}^v (m^2 s^{-1}) the vacancy diffusion coefficient at grain boundaries, ρ_P (m) is the radius of the Wigner-Seitz cell [17] assigned to each pore, k_B (J K^{-1}) is the Boltzmann constant, T (K) is the local temperature, and ζ (/) is a dimensionless factor calculated as

$$\zeta = \frac{10\psi(1+\psi^3)}{-\psi^6 + 5\psi^2 - 9\psi + 5} \tag{3.24}$$

where $\psi = R_{\bar{n}}^P/\rho_P$ is the ratio between the radii of the pore and of the cell. To evaluate the pore pressure, I employ the Hard Sphere (HS) Equation of State (EoS) as proposed by Carnahan and Starling [116], namely

$$\frac{p^P V_{\bar{n}}^P}{\bar{n}k_B T} = \frac{1 + \widetilde{y} + \widetilde{y}^2 - \widetilde{y}^3}{(1-\widetilde{y})^3} \; . \tag{3.25}$$

The reduced density – $\widetilde{y}$ – is calculated as presented in Section 2.2.5, $\widetilde{y} = \pi/6\,(\delta_{HS}^3 \upsilon)$ (/) where υ (atom m^{-3}) is the atomic density in the pore and δ_{HS} is Xe HS diameter.

The pore growth due to vacancy and gas atom absorption may trigger another mechanism of growth, i.e., interconnection by impingement. Since I widely described this phenomenon in a previous Chapter of the work – see Section 2.2.5, in the following I report only the final equation governing the variation rate of HBS pores due to interconnection, reading

$$\frac{\mathrm{d}N_P}{\mathrm{d}V_P} = -4\lambda^P N_P^2 \tag{3.26}$$

where $\lambda^P = (2-\xi)/[2(1-\xi)^3]$ is a correction factor limiting the interconnection rate when high local porosity are achieved and accounting for the non-superposition of HSs. A consistent treatment of the interconnection between polydispersed pores would entail the inclusion of additional, non-linear terms in the CD master equations (Eq.3.11), as shown e.g. in [208]. Nevertheless, this inclusion would require the solution of the overall system of equation, invalidating the Fokker-Planck expansion. Indeed, the solution of the CD master equations is not feasible for application to FPCs of the present model, thus I decided to consider the interconnection as it

---

[17]The radius of the Wigner-Seitz cell – see Figure 3.6 for a sketch of the system – is determined from the relationship $4/3\,\pi N_P \rho_P^3 = 1$.

would happen among monodispersed spheres featured by the average radius of the distribution.

The model presented in this Section allows for a consistent description of the evolution of HBS porosity and presents various original contributions with respect to the state of the art. First, the foundation of the modeling approach lies on the master equations of cluster dynamics. This allows including the effects due to the pore size distribution on the trapping and re-solution rates, constituting a step forward with respect to the available single-size models [32, 33, 177, 188, 189]. Second, the introduction of the dependence of grain boundary diffusivity on the tilt angle of grain boundaries physically embodies a feature often introduced artificially in HBS porosity modeling (e.g., [33, 177]) to reproduce experimental data. Third, the developed approach allows for tracking the evolution under irradiation of the pore-size distribution mean size and variance. These figures, combined with the assumption of a pore-size distribution *a priori* known, enables a consistent calculation of the evolution of the pore-size distribution under irradiation. Thus, the model can be plugged upon mechanistic models which need as input the distribution of HBS pore pressures to estimate micromechanics phenomena, such as grain boundary loss of cohesion in accident transients [212].

3.5 Results and Discussion

In this Section, I present the results of the presented model, comparing the predictions, in terms of local xenon retention as a function of effective burnup, to available experimental data and to several models available in the open literature and conceived for application to FPCs. The presented results were obtained implementing the model into the SCIANTIX code [52]. I showcase the capability of the model to account for matrix (macroscopic) swelling modification as HBS formation occurs. Finally, I compare the predictions of the model for the porosity evolution to recent experimental data, in terms of pore number density, mean radius, and gaseous swelling.

3.5.1 Choice of model parameters

The expressions of parameters mentioned in Section 3.3 and employed in SCIANTIX are reported in Table 3.4, while in this Section the choice of the most critical parameters is discussed.

For the diffusion coefficient in the non-restructured volume, the expression chose is taken from Turnbull and co-workers [106, 134] and the reader is referred to the discussion on its adoption in Section 2.4.1. For the diffusion coefficient in the restructured zone, I adopt the expression proposed by Pizzocri et al. [186], which envisages only an a-thermal contribution, different than the a-thermal component suggested by

Turnbull. To this regard, the HBS is supposed to form only in the fuel portion that experiences temperatures below a given threshold (around 1000°C) typical for the rim zone of LWR fuel. Applying both the thermal and irradiation-enhanced components of Turnbull diffusion coefficient expression under such conditions does not influence the results, since the a-thermal component dominates in such temperature ranges where the HBS forms. Moreover, as demonstrated by Brémier and Walker [214], the diffusion coefficient in the restructured zone must be different than the accepted values for the non-restructured region to explain the asymptotic concentration of gas retained in the matrix. As for the grain boundary diffusivity, the correlation (denoted as "low D") proposed by Olander and Van Uffelen [215] is employed, as it is one of the few available correlations for this parameter in the open literature. The transport of vacancies along the grain boundaries is accounted through an expression complementing the coefficient proposed by R. White [30] with an a-thermal factor, as suggested by Matzke [216] and as considered also by Jernkvist [173]. This latter parameter is as uncertain as the diffusion coefficient of gas atoms along the grain boundaries, being normally extracted by diffusional creep measurements. It represents an important parameter, governing the kinetics of pore growth, but it must be underlined that it does not concur in determining the asymptotic size of the pores (cfr Eq.3.23).

As for the re-solution rate of intra-granular bubbles, in this Chapter I employ

Table 3.4: Expressions of the model parameters.

Parameter	Expression/Value	Reference
D^{NR}	$D^{NR} = D_1 + D_2 + D_3$	[106]
	$D_1 = 7.6 \cdot 10^{-10} \exp(-4.86 \cdot 10^{-19}/k_B T)$	
	$D_2 = 5.64 \cdot 10^{-25} \sqrt{\dot{F}} \exp(-1.91 \cdot 10^{-19}/k_B T)$	
	$D_3 = 2 \cdot 10^{-40} \cdot \dot{F}$	
	k_B (J K^{-1}), Boltzmann constant	
	T (K), local temperature	
D^{HBS}	$D^{HBS} = 4.5 \cdot 10^{-42} \cdot \dot{F}$	[186, 214]
g_n	$g_n = 4\pi D N R(n)$	[105]
b_n	$b_n = 2\pi \mu_{ff} \dot{F} \left(R(n) + R_{ff} \right)^2$	[102]
	$\mu_{ff} = 6.0 \cdot 10^{-6}$ m, fission fragment track length	[102]
	$R_{ff} = 1.0 \cdot 10^{-9}$ m, fission fragment track radius	[102]
ν	$\nu = 2 \cdot 25 \cdot \dot{F}$	[21, 26]
B_{ig}	$4.09 \cdot 10^{-29}$ m^3	E.g., [26]
a	$5.47 \cdot 10^{-10}$ m	-
D_{gb}^{SA}	$D_{gb}^{SA} = 1.3 \cdot 10^{-7} \exp\left(-4.52 \cdot 10^{-19}/k_B T\right)$	[215]
D_{gb}^{v}	$D_{gb}^{v} = 8.86 \cdot 10^{-6} \exp(-5.75 \cdot 10^{-19}/k_B T) + 10^{-39}\dot{F}$	[30, 216]
ν_P	$\nu_P = 5 \cdot 10^{17}$ dα/dbu_{eff}	This work
d_V	$d_V = 1$ nm	[23]
δ_V	$\delta_V = 1$ nm	[23]
γ	$\gamma = 1$ J m^{-2}	[135]

the expression proposed by Turnbull [102], differently than in the previous Chapter. The same calculations considered in the following Section have been carried out also employing the correlation provided by Setyawan and co-workers [113] (I chose to not report them here for the sake of brevity). Due to the low temperatures experienced by the fuel in the conditions in which HBS develops in LWRs, the intra-granular bubbles do not reach sizes at which the two approaches to model irradiation-induced re-solution deviate substantially, thus the retained xenon concentration is not changing considerably employing the correlation by Turnbull or by Setyawan and co-workers. On the other hand, the re-solution of the HBS inter-granular pores is accounted for following the model by Veshchunov and Tarasov [23]. In fact, the model by Turnbull would predict an indefinite increasing of re-solution probability with the bubble size, while recent lower length scale calculations demonstrate an attenuation of re-solution with increasing bubble radii.

Lastly, the nucleation of HBS pores is evaluated as a constant value, proportional to the local degree of restructuring. Indeed, this approach reflects the experimental findings [93, 163, 164] but calls for a future, mechanistic refinement.

3.5.2   Xenon depletion

In Figure 3.8, I compare the intra-granular concentration of xenon predicted by SCIANTIX simulations, considering the present model, to several experimental data obtained by different authors [140, 143, 163] via EPMA. Considering the huge scattering of the experimental data, due to different irradiation conditions and initial fuel specifications, the agreement is deemed satisfactory, although some appreciable deviation can be noticed against the experimental data. For the sake of completeness, it must be underlined that xenon is accompanied by other gases in determining the overall gas behavior (namely, krypton and helium). In this work, I draw a special attention on xenon since it was the subject of the most intensive experimental investigations.

For the sake of comparison, I report also the results obtained by the several state-of-the-art models employed in FPCs, namely the model by Lassmann et al. [172], by Lemes et al. [176], and by Pizzocri et al. [186]. The models by Lassmann and Lemes, the latter being an extension of the former, represent pragmatic and purely empirical approaches to account for fission gas depletion as HBS forms, considering an exponential decay of retained gas concentration with burnup. Indeed, they are directly fitted on a subset of the reported EPMA data, i.e., those by Walker [163]. Moreover, they consider a threshold for HBS formation solely dependent on burnup, discarding the effect of temperature, which is instead considered in this work via the effective burnup concept. In Figure 3.8, predictions of those models considering different burnup thresholds are reported, showing how this parameter impacts the maximum xenon retention and the subsequent depletion. In this Figure, burnup and effective burnup coincide since the data were taken from the rim zone of commercial UO_2 fuel, where the fuel local temperature remains below 1000°C.

On the other hand, the model proposed by Pizzocri et al. [186] represents a step

forward with respect to the aforementioned ones, as it is not purely empirical. This model represents HBS formation by a gradual reduction of the grain size, which may be a questionable representation of the underlying physical processes. Differently from the present model results, the predictions obtained through this model and shown in Figure 3.8 are obtained considering a xenon production rate adjusted to the experimental data at low burnups to Walker data [163], to obtain a maximum xenon retention in line with experimental data. Finally, the model by Pizzocri et al. does not consider the evolution of intra-granular fission gas bubbles, employing a fixed value for intra-granular bubble density and radius, and disregards volume changes due to irradiation damage in the lattice. This results in an inconsistent estimation of gas partition between bubbles and dynamic solution, preventing a consistent calculation of matrix swelling due to single gas atoms and intra-granular bubbles, in addition to affect the "effective diffusion" representation.

The present model also accounts for the observed delay in xenon depletion (thus HBS formation) when considering higher grain sizes in the original microstructure, as shown in Figure 3.8 and coherently with several experimental observations [153, 193].
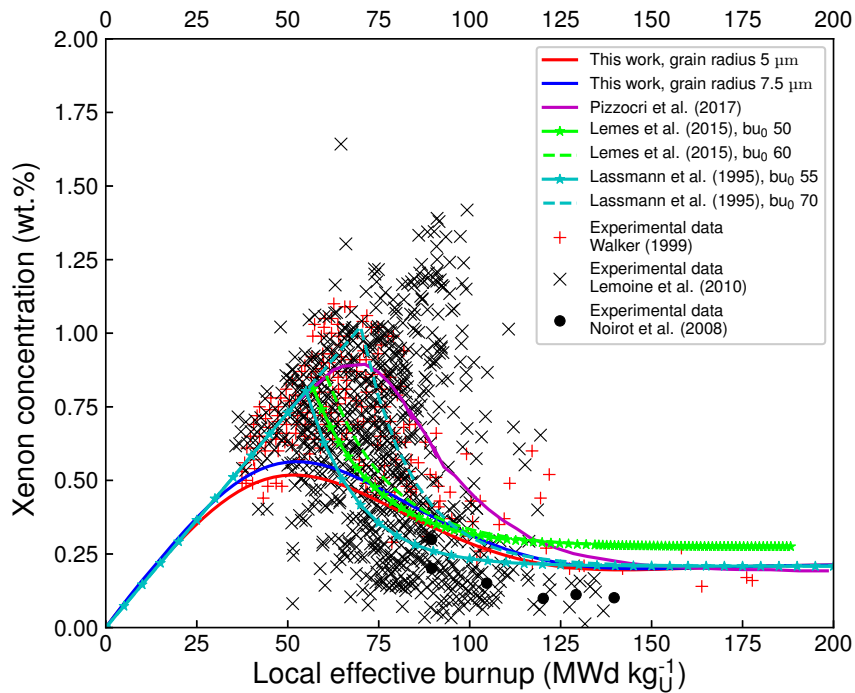
Figure 3.8: Comparison of various data on intra-granular xenon concentration obtained via EPMA (red crosses from Walker [163], black crosses from Lemoine et al. [143], and black dots from Noirot et al. [140]) to the predictions of the presented model. For the sake of comparison, the prediction obtained with other state-of-the-art models employed in fuel performance codes are included, namely from Pizzocri et al. [186], Lemes et al. [176], and Lassmann et al. [172].
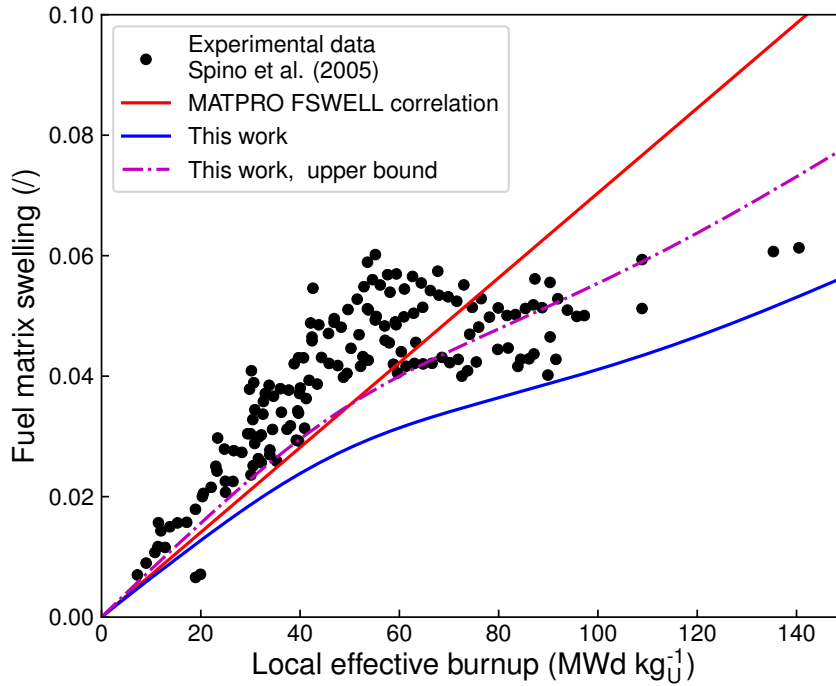
Figure 3.9: Comparison of predicted results on matrix fuel swelling to data elaborated by Spino et al. [101], based on Xe retention data obtained through EPMA by Walker [163].

3.5.3 Fuel total matrix swelling

In Figure 3.9, I compare the predictions obtained on the fuel total matrix swelling (as defined in Section 3.3.3) as a function of effective burnup to the data compiled by Spino et al. [101]. The matrix swelling predicted by the MATPRO FSWELL model – which is employed in several state-of-the-art fuel performance codes to evaluate the swelling due to solid fission products (e.g., in TRANSURANUS [12], BISON [53], FRAPCON/FRAPTRAN [175]) – is included for comparison and discussion.

The results obtained through the present model, both with the nominal and upper solid fission products swelling rates, demonstrate the impact of the matrix depletion of fission gas as HBS progressively forms. The depletion of fuel matrix, starting predominantly around 60 MWd kg_U^{-1}, causes a decrease of the fuel matrix swelling rate[18], in accordance with the elaboration presented by Spino et al. [101] and based on EPMA results on Xe retention. The agreement of the predicted trend of matrix swelling with the considered data is encouraging. As for the absolute value, the matrix swelling obtained with the nominal swelling rate ascribed to solid fission products (solid blue line in Figure 3.9), i.e., 0.32% per atom percent burnup[19] [1], and

---

[18]As discussed in Section 3.3.3, the removal of irradiation damage (i.e., dislocation loops) associated to the formation of pristine HBS grains might contribute to the lower swelling rate observed in this burnup range.

[19]The conversion adopted in this work from atom percent burnup to MWd kg_U^{-1} is 1 at.% = 9.38

considering the volume occupied by xenon in dynamic solution and intra-granular bubbles is somewhat underestimating the data reported and the values predicted via the MATPRO FSWELL model. On the other hand, the results obtained considering the upper bound of the solid swelling rate – 0.45% per atom percent burnup [1] – yields a better agreement with the considered data and with the MATPRO FSWELL model.

However, it must be noticed that the interpretation by Spino and coworkers of the data by Walker [163] entails a likely overestimation of the volume occupied by xenon atoms in intra-granular fission gas bubbles. To estimate the swelling due to intra-granular bubbles, the authors assume intra-granular bubbles to be in equilibrium and to obey the van der Waals equation of state [101]. The applicability of both the assumptions is questionable. On one hand, intra-granular bubbles forming under irradiation are far from being in equilibrium [80, 217, 218], thus, considering equilibrium bubble, the estimated radii are overestimated. On the other hand, the applicability of van der Waals equation of state to intra-granular bubbles is debatable, due to the high gas densities reached in intra-granular bubbles [80, 217]. This calls for the consideration of more advanced equations of state, e.g. the modified hard sphere equation of state proposed by Ronchi [219]. Based on these considerations, I postulate that the data presented by Spino and coauthors in [101] and reported in Figure 3.9 may somewhat be an overestimation of the actual portion of fuel matrix swelling ascribed to intra-granular gas.

3.5.4   HBS porosity

In Figures 3.10-3.12, I compare the model predictions in terms or pore number density, mean radius, and resulting gaseous swelling to the recent experimental data on HBS porosity in UO_2 obtained by Cappia and co-workers [124, 164]. The calculated quantities have been obtained considering an irradiation history representative for the conditions met in the periphery of a fuel pellet in PWRs, namely a temperature of 723 K, a fission rate density equal to $2 \cdot 10^{19}$ fiss $m^{-3} s^{-1}$, and a hydrostatic stress equal to 20 MPa representative for pellet-cladding mechanical interaction. Considering the uncertainty of model parameters and the modeling approach which must ensure a compatibility with the computational requirements of FPCs, the agreement between the predicted results and the experimental results is deemed encouraging. As a general trend, the agreement between the calculated quantities and the experimental data is very satisfying until 130 MWd kg_U^{-1}, whereas above this value more discrepancies arise. In particular, the overestimation of pore number density and underestimation of pore average radius beyond 150 MWd kg_U^{-1} (Figures 3.10 and 3.11) suggest how the growth of the HBS pores might be somehow underestimated at ultra high burnups. In fact, the slope of the pore radius calculation does increase around the aforementioned burnup value, yet the high radii experimentally observed cannot be reproduced. As for the resulting gaseous swelling, the experimental data
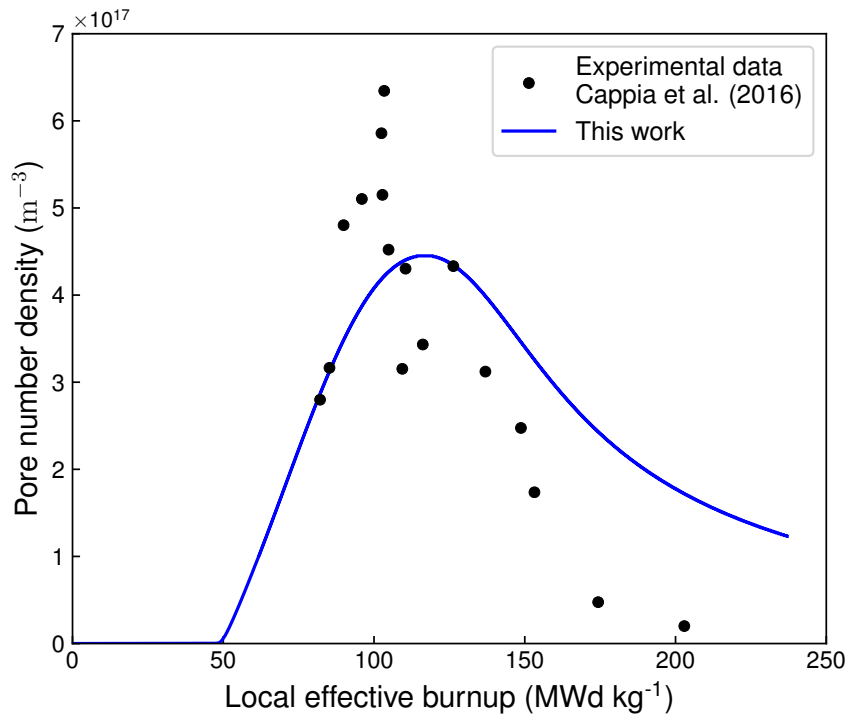

MWd kg_U^{-1}.

Figure 3.10: Comparison of experimental data on HBS pore number density taken from Cappia and co-workers [124, 164] to model predictions.
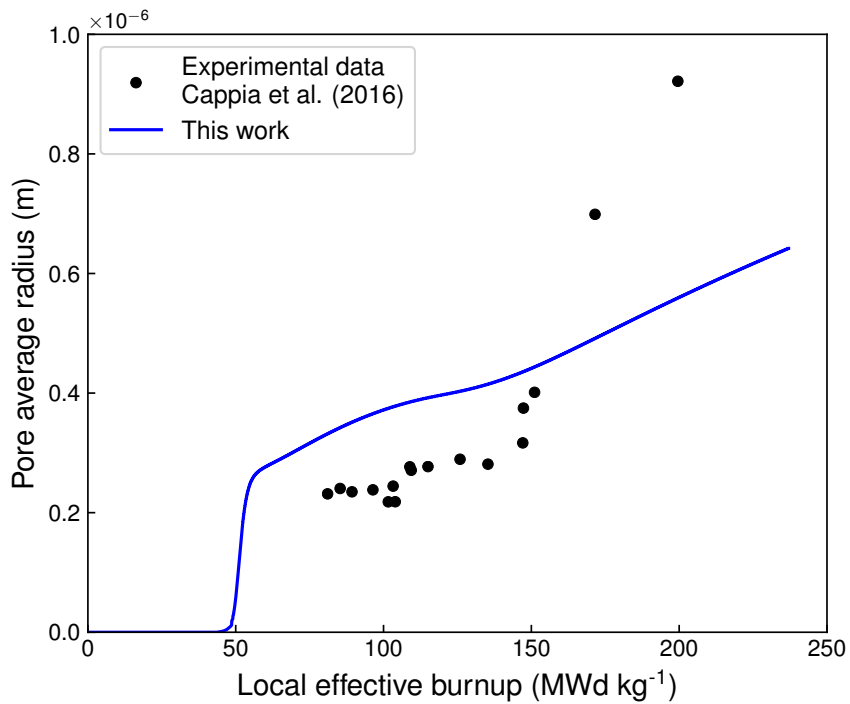

Figure 3.11: Comparison of experimental data on number-averaged pore radius taken from Cappia [124] to model predictions.
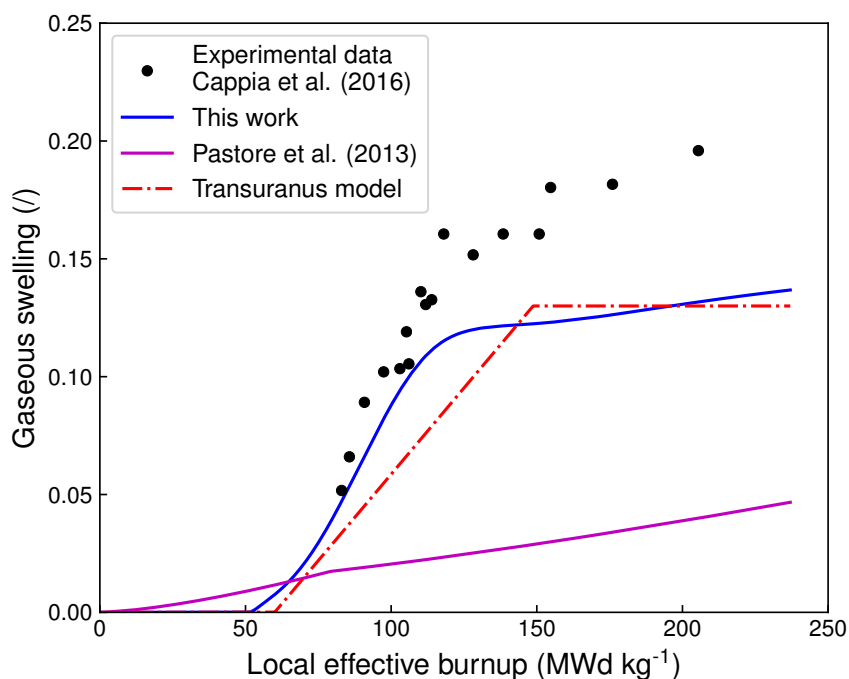
Figure 3.12: Comparison of experimental data on HBS gaseous swelling (i.e., on local porosity) taken from Cappia and co-workers [124, 164] to model predictions. For the sake of comparison, I include the predictions of state-of-the-art models available in industrial FPCs, namely the correlation-based model of TRANSURANUS accounting for HBS porosity [182], and the mechanistic model by Pastore et al. [34] accounting for gaseous swelling in low-medium burnup conditions.

are generally underestimated, while the same considerations apply for the pore evolution at ultra high burnups.

Indeed, the step forward brought about by the present modeling approach is depicted in Figure 3.12, where I compare the predictions of the proposed model to models included in state-of-the-art FPCs accounting for gaseous swelling and/or for HBS pore swelling. In particular, the comparison includes the correlation-based model available in TRANSURANUS to account for HBS porosity [182] and the mechanistic model by Pastore and co-workers [34], which accounts for conventional gaseous swelling. Although not directly conceived for HBS, the comparison to the latter model underlines the importance of a dedicated model for the HBS porosity description as the one developed in this thesis work. As for the former model, available in the TRANSURANUS code, it was derived as a pure fit of experimental data of porosity as a function of local burnup, and its predictions are in-line with those obtained by the developed, physics based model. In the light of these promising results, the presented model has been made available to the TRANSURANUS code via a developed coupling scheme with SCIANTIX. The coupled code suite will be subsequently validated against integral irradiation experiments including high burnup rods, to assess the impact of the HBS porosity model on the overall fuel rod performance.

3.6   Closing remarks

In this Chapter, I presented a novel model describing HBS formation, fission gas depletion, and porosity evolution in UO_2, conceived for application in fuel performance codes. The model is featuring a semi-empirical, yet physically-sound, description of HBS formation, described through the KJMA approach for phase transformation. I fitted the KJMA functional form to two sets of independent experimental data available in the open literature. In particular, the volume fraction of restructured fuel was correlated to the local effective burnup, i.e., the burnup accumulated below 1000°C, which was chosen as a lumped figure embodying the effect of irradiation damage and prevented annealing of the damage itself.

As for the HBS porosity evolution, the model is based on a Fokker-Planck expansion of the cluster dynamics master equations describing the pore behavior at grain boundaries. The Fokker-Planck approximation is truncated at the second order, yielding a model featured by a limited number of equations – thus compatible with the requirements of FPCs – yet allows estimating the evolution of pore number density, mean size and variance of the pore size distribution. In this framework, the evolution of the pores is accounting in a physically-based manner the phenomena determining the pore size, i.e., fission gas absorption, gas atoms re-solution, vacancy absorption to compensate for pore non equilibrium, and pore interconnection.

The model provides a consistent and continuous description of HBS formation, associated intra-granular fission gas behavior, and porosity evolution. In fact, the intra-granular fission gas behavior in the re-structured and original microstructure is described through a previously developed mechanistic model [26]. This modeling approach allows us to evaluate the evolution under irradiation of the intra-granular concentration of fission gas in the matrix and trapped into bubbles, together with the estimation of the diffusional flux towards the grain boundaries. The consistent, physically-grounded description of the kinetics of intra-granular gas behavior, fuel restructuring, and pore evolution paves the way to a wide applicability of the model in terms of operating conditions and fuel types, especially if compared to other state-of-the-art models used in industrial fuel performance codes, which constitutes the objective of my modeling effort. In this regard, the present model is compatible with the requirements, in terms of numerical stability and computational burden, for its inclusion in fuel performance codes, while preserving a degree of physical perspective on the considered phenomena, which is an improvement compared to the state-of-the-art models included in FPCs.

Comparison of the stand-alone model predictions to experimental data indicates a good agreement in terms of retained intra-granular xenon concentration, also when compared to semi-empirical models available in the open literature. The model can reproduce the experimentally observed delay in xenon depletion – connected to a delayed HBS formation – when the original microstructure is featured by larger grain sizes. The results in terms of matrix fuel swelling predicted by the model are well reproducing the experimentally observed change in fuel matrix swelling rate at high burnup, as a consequence of the depletion of the xenon retained in dynamic solution with the matrix. Moreover, the comparison to experimental data on HBS porosity

shows a satisfactory agreement in terms of pore number density and average radius. Albeit slightly underestimating the resulting gaseous swelling, the model ensures a substantial step forward with respect to the state-of-the-art models in the estimation of HBS porosity. The model has been implemented into the SCIANTIX code and will be distributed open-source. The present work will be complemented in the future by an integral assessment of the overall model on fuel performance simulations, namely via the TRANSURANUS-SCIANTIX code suite, of high burnup rods.

The developed modeling approach paves the way to the analysis of HBS in other oxide fuel concepts. Indeed, the "two phases" modeling strategy applied to describe HBS formation and intra-granular behavior finds a natural application to MIMAS MOX fuels, thus an analysis of this type of fuels is of interest in perspective. As for FBR U-Pu oxide, few experimental data are available in the open literature on the HBS in such conditions. The trends would suggest a possible delay in HBS formation as a function of the local burnup and a different asymptotic grain size in the restructured zone, with a consequent lower xenon retention.

As for the porosity evolution, the underestimated pore growth at ultra high burnups calls for additional modeling efforts. A possible development path could entail the consideration of higher order pore interactions during the interconnection process, as made by Veshchunov and co-workers [37, 190] introducing a three-body scheme, or considering the interaction of a population of polydispersed spheres in the two-body scheme. Moreover, in the light of the substantial uncertainties on model parameters and input quantities for the porosity model (e.g., the local fission rate), a sensitivity and uncertainty analysis of the model outputs to the aforementioned quantities would help to investigate the deviations between calculated and experimental data.

CHAPTER 4. MULTISCALE MODELING OF FISSION GAS BEHAVIOR IN U$_3$SI$_2$ UNDER LWR CONDITIONS

"Ho sceso, dandoti il braccio, almeno un milione di scale"

E. Montale, *Satura – Xenia II*, 1971

Abstract

In this Chapter, I present a model of fission gas behavior in U$_3$Si$_2$ under light water reactor conditions for application in engineering FPCs. The model includes components for intra-granular and inter-granular behavior of fission gases. The intra-granular component is based on cluster dynamics and computes the evolution of intra-granular fission gas bubbles and swelling coupled to gas diffusion to grain boundaries. The inter-granular component describes the evolution of grain-boundary fission gas bubbles coupled to fission gas release. Given the lack of experimental data for U$_3$Si$_2$ under LWR conditions, the model is informed with parameters calculated via atomistic simulations. In particular, fission gas diffusivities are derived through density functional theory calculations, and the re-solution rate of fission gas atoms from intra-granular bubbles through binary collision approximation calculations. The developed model is applied to the simulation of an experiment for U$_3$Si$_2$ irradiated under LWR conditions available from the literature. Results point out a credible representation of fission gas swelling and release in U$_3$Si$_2$. Finally, I perform a sensitivity analysis for the various model parameters. Based on the sensitivity analysis, indications are derived that can help in addressing future research on the characterization of the physical parameters relative to fission gas behavior in U$_3$Si$_2$. The developed model is intended to provide a suitable infrastructure for the engineering scale calculation of fission gas behavior in U$_3$Si$_2$ that exploits a multiscale approach to fill the experimental data gap and can be progressively improved as new lower-length scale calculations and validation data become available.

4.1 Introduction

Accident tolerant fuel systems are being considered worldwide to replace the UO_2–zirconium system conventionally employed in LWRs, in order to withstand a severe accident for a considerably longer period of time than the traditional design, while preserving or improving performance under normal operation conditions [220–223]. In this context, the United States Department of Energy has accelerated research in this area, promoting the Fuel Cycle Research and Development Advanced Fuel Campaign (AFC). The goal of the Accident Tolerant Fuel (ATF) program of the AFC is to guide the selection of promising fuel concepts to start a test rod irradiation in a commercial reactor by 2022.

Focusing on the nuclear fuel, uranium silicides are potential candidates to substitute uranium dioxide in LWR. Among uranium silicides, compounds such as U_3Si, U_3Si_2, and U_3Si_5 emerge, thanks to their interesting thermophysical properties and high uranium densities [224, 225]. Those characteristics make these compounds attractive from the economic and safety point of view.

A wide experience exists worldwide in using uranium U_3Si and U_3Si_2 as fuel for research and test reactors [226–231]. On the other hand, to the best of the authors' knowledge, only one experiment has been carried out for U_3Si_2 under power reactor conditions [232][20].

Based on the experience with research and test reactors, potential concerns about the adoption of uranium silicides in commercial reactors are related to the progressive amorphization of the crystalline structure under irradiation and high swelling rates [234–236]. In particular, amorphization of U_3Si_2 has been observed in research reactor conditions [237, 238], where fuel temperatures are lower compared to LWR conditions. However, recent studies carried out on U_3Si_2 with Xe ion implantation [239–242] suggest that U_3Si_2 would remain crystalline under irradiation in LWR conditions. The polycrystalline structure of U_3Si_2 irradiated at power reactor temperatures finds confirmation in the post-irradiation metallographic images in [232].

Given the aggressive schedule, the AFC is carrying out comprehensive experiments to characterize the innovative fuel systems, as well as computational analyses to investigate the proposed materials. In this framework, given the importance of fission gas swelling and release in the thermo-mechanical performance of nuclear fuel rods, the accurate modeling of fission gas behavior as part of engineering fuel rod analysis is of the utter importance [1]. Mechanistic modeling of fission gas behavior calls for the description of complex processes, both within the fuel grains and at the grain boundaries. Intra-granular behavior involves gas bubble evolution and swelling coupled to gas atom diffusion to grain boundaries. Grain-boundary processes

---

[20]In addition, a new experiment is underway in the framework of the ATF–1 tests series of the AFC/ATF program, with two rodlets of U_3Si_2 pellets with ZIRLO® cladding being irradiated in the Idaho National Laboratory Advanced Test Reactor (ATR) under LWR conditions. The first non–destructive and metallography examinations demonstrated a good performance under irradiation of the U_3Si_2 fuel, at least at the low burnup (less than 20 GWd tHM^{-1}) targeted [233?].

include precipitation, growth and coalescence of lenticular bubbles contributing to fuel swelling, and the eventual gas venting from the grain boundaries leading to thermal FGR. Venting occurs after extensive gas bubble growth and interconnection, driven by gas atom and vacancy diffusion to the bubbles [1].

Rest [47] proposed a model for FGB in U_3Si_2, tailored for research reactor conditions, where fuel amorphization occurs. In the aforementioned work, the nucleation of fission gas bubbles was described as related to the amorphization process itself. This latter aspect constitutes a limitation to the application of the model in the analysis of U_3Si_2 in LWR conditions. Miao et al. [42] adopted the GRASS-SST rate theory model [243], calibrating it with a combination of experimental data on U_3Si_2 from research reactors and density functional theory calculations. They studied fission gas swelling in U_3Si_2 under LWR conditions, simulating an idealized fuel rod irradiated at constant power (average linear heat rate equal to 20 kW m^{-1}) for about 3 years. Moreover, they developed a steady-state gaseous swelling correlation based on the rate theory model to be included in the BISON FPC [53]. The GRASS-SST model is based on rate theory and calculates fission gas bubble size distributions considering the evolution of clusters of fission gas atoms of different sizes explicitly. While such a level of complexity provides valuable insight into the physical details, a simpler approach that only targets the average bubble size and number density may allow for a more efficient application in engineering codes, while still providing accurate calculation of the quantities of interest for the fuel rod thermo-mechanical analysis, i.e., bubble swelling and FGR.

In this work, I propose a multiscale model of fission gas swelling and release in U_3Si_2 under LWR conditions for application in engineering fuel analysis. The model includes components for intra-granular and grain-boundary behavior of fission gases. The intra-granular component describes the evolution during irradiation of the average size and number density of intra-granular fission gas bubbles coupled to gas diffusion to grain boundaries. The grain-boundary component is based on the modeling approach originally developed for UO_2 in [34], and describes the evolution of inter-granular fission gas bubbles coupled to fission gas release from the grain boundaries to the fuel rod free volume. Experimentally derived values for important modeling parameters, such as the lattice diffusion coefficient of gas atoms and the rate of irradiation-induced re-solution of gas atoms from intra-granular bubbles, are unavailable at this time for U_3Si_2 under LWR condition. To overcome this limitation, I adopt a multiscale modeling approach (e.g., [38, 39, 41, 244]), whereby the engineering scale model is informed with parameters extracted at the lower-length scale via atomistic simulations. In particular, the fission gas atom and point defect diffusivities are calculated through DFT calculations, and the re-solution rate through Binary Collision Approximation (BCA) calculations.

For an initial assessment of the model, I analyze the U_3Si_2 irradiation experiment from [232] and compare the results to the experimental data of gaseous swelling and fission gas release. Finally, I performed a sensitivity analysis to assess the importance of the various model parameters on the calculated fission gas swelling and release, and to derive recommendations for future research on the characterization of the physical parameters.

Extensive model validation will be performed as more substantial experimental

data for U_3Si_2 under LWR conditions become available. The work is intended to provide an initial framework for the engineering analysis of fission gas behavior in U_3Si_2 that is able to exploit lower-length scale modeling for the fundamental parameters. Such a multiscale approach is particularly beneficial to accelerate progress in modeling new fuel concepts such as U_3Si_2, for which experimental data is limited. The developed model can be progressively improved as new lower-length scale calculations and validation data become available.

The outline of the Chapter is as follows. In Section 4.2, I present the lower-length scale calculations for the derivation of model parameters. In Section 4.3, I describe the new engineering fission gas behavior model for U_3Si_2. In Section 4.4, I apply the model to the simulation of an irradiation experiment for U_3Si_2 irradiated at temperatures compatible with LWR conditions. In Section 4.5, I present the sensitivity analysis. Finally, in Section 4.6, I draw the conclusions and discuss perspectives.

4.2 Lower-length scale calculations

In this Section, I present the methodology and the results of the lower-length scale calculations for the derivation of the parameters used in the engineering scale model. The DFT calculations employed to derive fission gas and point defect properties in U_3Si_2 are presented in Section 4.2.1, while the calculation of the re-solution rate is presented in Section 4.2.2.

4.2.1 Density functional theory calculations of defects and fission gas properties

The fission gas model derived in this Chapter requires the diffusion rates of Xe atoms and uranium vacancies in U_3Si_2. I rely on density functional theory calculations to provide initial estimates of these rates. The full results of the DFT calculations are presented elsewhere [245]. Here, I briefly outline the computational methodology and the key results used in the fission gas model presented in Section 4.3.

The approach and underlying model are the same as those described in [42], but the calculations were performed on $2 \cdot 2 \cdot 3$ instead of a $2 \cdot 2 \cdot 2$ U_3Si_2 supercells and a few assumptions regarding entropies were slightly modified. The reason for increasing the size of the supercell is to improve the accuracy of, in particular, migration barriers in the **c** lattice direction of U_3Si_2. However, none of these updates in the methodology give rise to substantial changes as compared to [42]. As an example, the predicted barriers decrease by a few tenths of an eV compared to the earlier results [42]. The DFT calculations were performed with the Vienna Ab initio Simulation Package (VASP) [246, 247] and the Projector Augmented-Wave (PAW) method for the core electrons. The exchange-correlation potential was described

by the Perdew-Burke-Ernzerhof (PBE) potentials and a Hubbard U parameter was added for the uranium 5f electrons [248], which follows the same methodology as used by Noordhoek et al. [249], Middleburgh et al. [250], and Miao et al. [42]. Migration barriers were calculated using the Nudged Elastic Band (NEB) [251]. The energy cut-off for the plane-wave expansion of the wavefunctions were set to 500 eV and sampling in reciprocal space was performed on $2 \cdot 2 \cdot 2$ Monkhorst-Pack meshes. All defect structures were fully relaxed (volume and atomic positions), while migration barriers were calculated for the volume fixed at that of the initial state.

Diffusion in U_3Si_2 is anisotropic due to its tetragonal crystal structure, which results in unique diffusion rates in the basal **a-b** plane and along the **c** axis. The migration barriers of vacancies and Xe atoms were calculated for a range of possible mechanisms, see [245] for additional details. Here I am only concerned with the fastest diffusion rate of Xe and uranium vacancies. For both of these species the highest diffusivity is obtained for vacancy mechanisms along the **c** axis. The Xe diffusion mechanism refers to a Xe atom occupying a U 2a trap site in the U_3Si_2 crystal structure, with an assisting U 2a vacancy providing the diffusion pathway. A schematization of the aforementioned diffusion process is provided in Fig. 4.1. The rate limiting step is given by the U 2a vacancy migrating from one side of the cluster to the other in order to initiate a new step. The intra-cluster step for the Xe atom has a much lower barrier, similar to Xe migration in UO_2 [252]. In addition to the Xe-vacancy cluster migration rate, the diffusion coefficient is a function of the relative concentration of mobile Xe clusters, which is determined by the binding energy of a U 2a vacancy to a Xe atom occupying a U 2a trap site and the concentration of U 2a vacancies in the bulk. The concentration of vacancies in bulk U_3Si_2 is estimated from the U 2a Frenkel reaction and assuming close to perfect U_3Si_2 stoichiometry, which is here assumed to imply an equal concentration of interstitials and vacancies such that the vacancy formation energy is equal to half of the U 2a Frenkel energy. It is also important to point out that the U 2a substitutional position is the most favorable trap site for Xe. The fastest uranium vacancy migration mechanism also involves a U 2a vacancy moving along the **c** axis of the U_3Si_2 crystal structure. The rate applicable to the present study is the uranium self-diffusion rate, which in addition to the vacancy migration properties also includes the concentration of vacancies obtained from the formation energy discussed above in the context of binding to the Xe trap site. These two mechanisms are assumed to provide the most relevant rates governing fission gas behavior in the present study. Note that anisotropy in diffusion may also affect these rates, however, the evaluation of this aspect is left as future work.

The defect formation and migration energies used to estimate diffusion properties are listed in Table 4.1.

In order to predict the actual diffusion rates, the entropies that correspond to the energies discussed above as well as the attempt frequencies for migration must be estimated. Those values require calculations of phonons in U_3Si_2 as well as in U_3Si_2 containing defects, which is a much more challenging and time consuming task than the energies. For this reason, approximations based on experience from other materials such as UO_2 have been resorted[40]. Note that these assumptions are

Table 4.1: The point and Xe defect properties used to estimate the diffusion rates in U_3Si_2.

	Energy (eV)	Entropy (k_B)	Attempt frequency (s^{-1})
U 2a Frenkel reaction	2.55	5	N/A
U 2a vacancy formation	1.275	2.5	N/A
U 2a migration along **c** axis	1.22	N/A	$5 \cdot 10^{12}$
Binding of U 2a vacancy to Xe in a U 2a site	-0.90	0	N/A
Migration of the bound Xe-U 2a vacancy cluster	1.62	N/A	$5 \cdot 10^{12}$

meant to give an order of magnitude result rather than an exact value. The U 2a Frenkel entropy was set to 5 k_B, the binding entropy of a vacancy to the Xe atom in U 2a trap site to 0 k_B and the attempt frequency for all migration events to $5 \cdot 10^{12}$ s^{-1}. These values are also summarized in Table 4.1.

The final diffusion rates are calculated from

$$D = vj^2 Z \exp\left(-G_a/(k_B T)\right)/6 \qquad (4.1)$$

where v is the attempt frequency (s^{-1}), j the jump distance (m), and Z (-) the
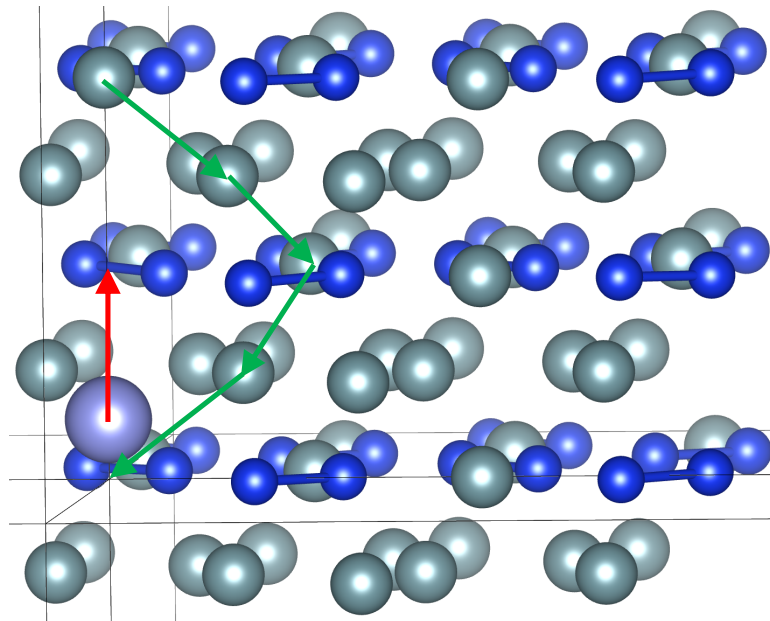

Figure 4.1: Xe diffusion mechanism in U_3Si_2 involving a Xe atom in a uranium vacancy trap site and a second uranium vacancy assisting diffusion in the **c** direction. The red arrow indicates the migration step of the Xe atom, but the rate-limiting step corresponds to diffusion of the assisting uranium vacancy from one side of the cluster to the other as shown by green arrows.

number of sites available for the Xe atom or vacancy to jump to, G_a (eV) is the activation free energy given by the migration enthalpy and the defect formation and binding energies and entropies. The resulting activation energies and pre-exponential factors for diffusion are listed in Table 4.2.

The diffusion model above only applies to intrinsic diffusion, which implies regimes where the thermal concentration of point defects dominates over irradiation induced defects. Estimation of the latter contribution would require a combination of extensive MD simulations of cascades and cluster dynamics modeling. This is beyond the present scope and must be left as future work. Neglecting the contribution of irradiation-enhanced diffusion is expected to lead to an underestimation of the diffusion rates at low temperature.

4.2.2 Intra-granular re-solution calculation

The re-solution rate, or rate of fission gas knock-out from bubbles, is a key parameter for calculation of intra-granular fission gas concentrations. The balance between absorption by bubbles and knock-out leads to a pseudo steady-state concentration of mobile fission gas atoms within the grain that ultimately leads to growth of grain-face bubbles, interconnection, and fission gas release. The full results of the calculation of re-solution in uranium silicide will be presented elsewhere, with a brief overview of the methodology given below in order to provide a reference for the values utilized in Section 4.3.

The total re-solution rate at which atoms are knocked back into the fuel can be calculated by,

$$\dot{R}\left(\mathrm{s}^{-1}\right) = \dot{F} \int \alpha_0(R_b) n(R_b) f(R_b) dR_b, \tag{4.2}$$

where R_b is the bubble radius, $\dot{F}$ is the fission rate density, α_0 is the re-solution parameter, n is the number of atoms in a bubble, and $f(R_b)$ is the bubble concentration distribution function,

$$N\left(\mathrm{m}^{-3}\right) = \int f(R_b) dR_b. \tag{4.3}$$

Here, N is the total concentration of bubbles in the sample.

Using Equation 4.2, the physics of re-solution can be distilled in a single re-solution parameter for a given fuel type, α_0, effectively separating environmental variables such as fission rate, temperature, and the bubble concentration distribution. The re-solution parameter has units of knocked-out atoms per atoms in the bubble per fission, and essentially gives the probability of any given atom in a bubble to be knocked-out per fission.

The first conceptual model of fission gas re-solution was the so called homogeneous model presented by Nelson in 1969 [253]. The homogeneous model treats the collision of fission fragments ballistically, with gas atoms being knocked out of a gas

bubble due to a collision with the fission fragments, or indirectly through a damage cascade produced by an adjacent fuel atom. In contrast to the chipping out process described by Nelson, Turnbull's model of re-solution published in 1971 was based on the assumption of total-destruction of the fission gas bubble by passing fission fragments [102].

The apparent conflict between the two re-solution theories lies directly with the difference of oxide nuclear fuel; calculations by Blank and Matzke showed that the poor thermal conductivity of UO_2 results in a very large, localized thermal spike around the passing fission fragment, on the order of 2000 K [254, 255]. The large temperature gradient results in a strong thermo-mechanical pulse, causing mixing of the lattice and destruction of nearby bubbles [256]. The same calculations performed for uranium carbide, which benefits from a metallic-like thermal properties [254] showed a corresponding thermal spike on the order of 50 K, with effectively no resulting thermo-mechanical pulse. In light of the differences between UO_2 and UC, it is easy to see why Turnbull's theory has seen success in oxide fuels, while Nelson's theory has seen success in non-oxide fuels [257]. As a first approximation, the thermal conductivity of the fuel can be used as an indicator of the energy transfer mechanism, with poorly conducting fuels (here only UO_2) suffering from large heterogeneous re-solution, and highly conducting fuels (UC, UN, $U_3Si_{1,2,5}$) exhibiting homogeneous re-solution behavior.

Modern calculations of re-solution have focused on UO_2 through utilization of MD simulations [110, 112, 258], but ultimately suffer from the high computational cost of MD. In light of the above discussion, re-solution in fuels with good thermal behavior can be modeled using the homogeneous model, allowing less computationally expensive models and codes to capture the re-solution behavior.

Recently, the BCA has been utilized to calculate the re-solution rate in uranium carbide fuels for a wide range of bubble sizes [257]. Benefiting from the simplification of the collision kinematics to a two-body problem, the code 3D Oregonstate TRIM (3DOT) utilizes the Transport of Ions in Matter (TRIM) algorithm [259] to capture the full cascade behavior of fission fragments interacting with fission fragments in fuel.

Utilizing the techniques provided in Matthews et al. [257], the re-solution parameter for U_3Si_2 was calculated for a variety of different conditions such as bubble shape, surface energy, bubble radius, and temperature. Beyond a general decrease in α_0 as a function of radius, many of the parameters that go into the BCA calculations result in minimal deviation in the re-solution parameter α_0. As a result, a simple correlation provided in Table 4.2 can be utilized for these studies. Further parametric studies on the impact of parameters in the 3DOT simulation is left as future work.

4.3   Engineering-scale fission gas behavior model

Considering that U_3Si_2 under LWR conditions retains a polycrystalline structure, fission gas behavior is modeled as consisting of two main stages for intra-granular and inter-granular behavior, by analogy with UO_2 (e.g., [1, 18, 21, 30, 34, 260]. The

intra-granular component of the model (Section 4.3.1) includes the fundamental mechanisms of nucleation and re-solution of intra-granular fission gas bubbles, gas atom trapping from the matrix into the bubbles, and gas atom diffusion to grain boundaries. The inter-granular component (Section 4.3.2) also adopts a mechanistic but relatively simple approach that encompasses grain-boundary bubble growth with inflow of gas atoms and vacancies, bubble coalescence, and fission gas release from the grain boundaries. The modeling approach is based on the concepts originally developed for UO_2 in [26, 34]. However, the current model is tailored to the specific physical mechanisms and material properties for U_3Si_2.

4.3.1   Intra-granular fission gas behavior model

The intra-granular component of the model provides calculation of the gas diffusion rate to grain boundaries and of the intra-granular fission gas bubble swelling. The latter is computed based on a description of intra-granular bubble evolution in terms of number density and average size. As discussed in Chapter 3, detailed description of gas bubble evolution can be accomplished by employing cluster dynamics approaches to calculate the entire bubble size distribution and the evolution of the distribution over time. However, these detailed modeling approaches are computationally intensive and simpler models are normally used for engineering FPC applications. The procedure I adopt in this Chapter follows that exposed in Chapter 3, yet I present it tailored for application to intra-granualr gas behavior in U_3Si_2.

Following Clement and Wood [207], I derive the model starting from the detailed cluster dynamics representation, but I simplify the problem by considering only the moments of the size distribution of the clusters. Assuming that bubbles include all clusters containing two or more gas atoms, I define the total concentration of bubbles N (m^{-3}) and the mean of the size distribution $\bar{n}$ (/), respectively

$$N = \sum_{n=2}^{\infty} c_n \tag{4.4}$$

$$\bar{n} = \frac{\sum_{n=2}^{\infty} n c_n}{N} \tag{4.5}$$

where c_n (at m^{-3}) is the number density of atom clusters (or bubbles) containing n atoms (with c_1 indicating the concentration of single gas atoms). The detailed

cluster dynamics formulation of the master equations considered here is [261]

$$
\begin{cases}
\dfrac{\partial c_1}{\partial t} = D\nabla^2 c_1 + G - 2\nu + \alpha_2 c_2 - \displaystyle\sum_{n=2}^{\infty}\beta_n c_n + \sum_{n=3}^{\infty}\alpha_n c_n \\[2ex]
\dfrac{\partial c_2}{\partial t} = D_2\nabla^2 c_2 + \nu - (\beta_2 + \alpha_2)c_2 + \alpha_3 c_3 \\[1ex]
\vdots \\[1ex]
\dfrac{\partial c_n}{\partial t} = D_n\nabla^2 c_n + \beta_{n-1} c_{n-1} - (\beta_n + \alpha_n)c_n + \alpha_{n+1}c_{n+1}
\end{cases}
\tag{4.6}
$$

where α_n (s^{-1}) represents the probability per second that an atom is re-solved from a cluster containing n atoms, β_n (s^{-1}) the probability per second that a single atom is trapped by a cluster containing n atoms, D_n (m^2 s^{-1}) is the diffusion coefficient of the cluster containing n atoms, ν (at m^{-3} s^{-1}) is the nucleation rate of fission gas dimers, and G (at m^{-3} s^{-1}) is the production rate of gas atoms.

A schematic of the master equations governing the bubbles' nucleation, growth due to single atom trapping and shrinkage due to re-solution of single atoms in the fuel matrix is reported in Figure 4.2.

The re-solution of gas atoms from the intra-granular bubbles into the fuel matrix is modeled as an irradiation-driven mechanism. Accordingly, I express the re-solution rate for U$_3$Si$_2$ as

$$
\alpha = \alpha_0 \dot{F}
\tag{4.7}
$$

where α_0 (m^3) is a coefficient, which can in principle depend on the cluster size, and $\dot{F}$ (m^{-3} s^{-1}) is the fission rate.

The trapping of gas atoms into intra-granular bubbles is modeled as a purely diffusion-driven process, and the trapping rate is calculated according to the formu-
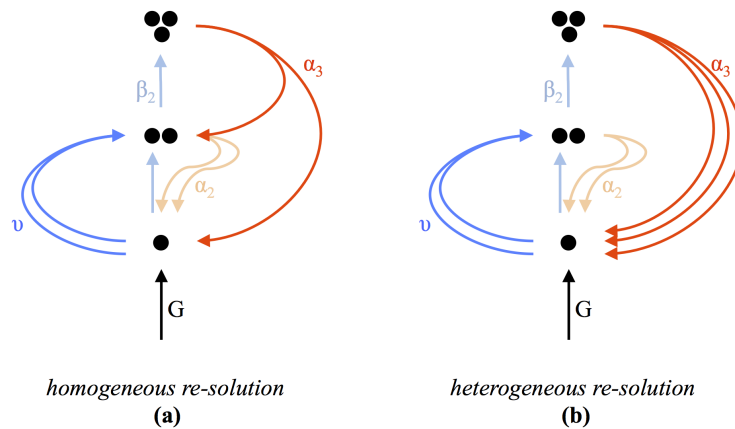

Figure 4.2: Sketch of the mechanisms of cluster dynamics considering (a) homogeneous and (b) heterogeneous re-solution.

lation by Ham [105], considering immobile and dilute clusters

$$\beta_n = 4\pi D R_n c_1 \tag{4.8}$$

where D is the single gas atom diffusion coefficient in the fuel matrix, R_n (m) is the cluster size, and c_1 is the concentration of atoms in the matrix.

The nucleation of bubbles in U_3Si_2 is modeled as a diffusion-dependent process, consisting of dimer formation upon interaction of single gas atoms driven by atom diffusion in the matrix (so-called homogeneous nucleation [56, 154]). The resulting nucleation rate can be expressed as [101]

$$\nu = 8\pi D R_{sg} f_n c_1^2 \tag{4.9}$$

where D is the diffusion coefficient of single gas atoms in the fuel matrix, R_{sg} (m) is the radius of a gas atom, and f_n (-) is the nucleation factor.

Combining Eqs. 4.5-4.6, I derive a single-size model consisting of expressions for the time evolution of N and $\bar{n}$, as follows. After algebraic summation, a first order Taylor expansion in the phase space is performed, namely

$$(\beta_n, \alpha_n, c_n) = (\beta(n), \alpha(n), c(n)) \approx (\beta_{\bar{n}}, \alpha_{\bar{n}}, c_{\bar{n}}) + \frac{\partial(\beta, \alpha, c)}{\partial n} dn... \tag{4.10}$$

Introducing the further assumption that the nucleation process occurs on a faster time scale compared to the growth process (i.e., $dN/dt \approx 0$ in the equation for $d\bar{n}/dt$), leads to

$$\begin{aligned} \frac{dN}{dt} &= \nu - \alpha_2 c_2 = \nu - \alpha_2 \phi N \\ \frac{d\bar{n}}{dt} &= \beta_{\bar{n}} - \alpha_{\bar{n}} \end{aligned} \tag{4.11}$$

where I account for the fact that homogeneous (one by one atom) re-solution in fact results in complete bubble destruction if the re-solution event occurs for a dimer. The factor $\phi = c_2/N$ represents the fraction of dimers over the total number of bubbles. The term $\alpha_2 \phi$ represents the probability per second of bubble destruction applied to the total number density of clusters, N. A bubble of size $\bar{n}$ will require on average $\bar{n} - 1$ homogeneous re-solution events before being destroyed. Considering this, in the single-size approach I estimate ϕ as

$$\phi = \frac{1}{\bar{n} - 1} \tag{4.12}$$

I define the total concentration of gas in bubbles, m (at m^{-3}), as

$$m = \bar{n} N \tag{4.13}$$

With the approximations of Eq. 4.10 and considering Eqs. 4.13 and 4.11, Eqs. 4.6 reduce to

$$
\begin{cases}
\dfrac{\mathrm{d}N}{\mathrm{d}t} = \nu - \alpha\phi N \\[2mm]
\dfrac{\partial c_1}{\partial t} = D\nabla^2 c_1 - \beta_{\bar{n}}N + \alpha\phi m + G - 2\nu \\[2mm]
\dfrac{\partial m}{\partial t} = 2\nu + \beta_{\bar{n}}N - \alpha\phi m
\end{cases}
\tag{4.14}
$$

Note that I introduced the additional assumption of immobile bubbles, with the diffusion term being considered for single gas atoms only. Differently from previous formulations of the single-size homogeneous model [56], the evolution of the bubble number density, N, considers also a term of bubble destruction, which corresponds to dimers affected by a homogeneous re-solution event. Moreover, homogeneous nucleation is consistently considered as a process of formation of dimers rather than considering nucleation at the average bubble size, which in previous work has been deemed as "the Achilles heel of the single-size method because it implies essentially instantaneous growth of dimers" to the average bubble size [56]. Hence, the model derived from a detailed cluster dynamics approach retains important bubble-distribution related effects in a formulation that in its final form only includes equations for the average quantities. Furthermore, the present model includes gas diffusion to grain boundaries in conjunction with bubble evolution.

The set of coupled partial differential equations (Eqs. 4.14) is solved using the recently developed PolyPole-2 algorithm [201], extended to the solution of the 3-equation system. Details of this extension are not given here for brevity, however, the concept of the algorithm is the same as described in [201].

The solution of Eqs. 4.14 provides the bubble number density, the rate of single gas atom diffusion to grain boundaries, and the average number of atoms per bubble. While for UO$_2$ substantial experimental data is available, including data on the gas density in intra-granular bubbles that can be used to determine the average bubble size given the average number of gas atoms per bubble in a simple way [26, 56], such information is missing for U$_3$Si$_2$ under LWR conditions. Therefore, I developed a physics-based approach to model intra-granular bubble growth considering the interactive gas atom and vacancy absorption at the bubbles, as follows.

Intra-granular fission gas bubbles are assumed spherical. The mechanical equilibrium of a spherical bubble is governed by the Young-Laplace equation

$$
p_{eq} = \frac{2\gamma}{R_b} - \sigma_h
\tag{4.15}
$$

where p_{eq} (Pa) is the equilibrium pressure, γ (J m^{-2}) is the U$_3$Si$_2$/gas specific surface energy and σ_h (Pa) is the hydrostatic stress (considered negative if the medium is under compression). In general, the bubbles are in a non-equilibrium state and tend to the equilibrium condition by absorbing or emitting vacancies. The bubble volume

is calculated through

$$\frac{\mathrm{d}V_b}{\mathrm{d}t} = \omega\frac{\mathrm{d}\bar{n}}{\mathrm{d}t} + \Omega\frac{\mathrm{d}n_{iv}}{\mathrm{d}t} \tag{4.16}$$

where V_b (m^3) is the bubble volume, ω (m^3) is the van der Waals atomic volume for xenon, and Ω (m^3) is the vacancy volume. The variation rate of the number of atoms per bubble, $\mathrm{d}\bar{n}/\mathrm{d}t$, is obtained from Eqs. 4.13 and 4.14. The vacancy absorption/emission rate at the bubble, $\mathrm{d}n_{iv}/\mathrm{d}t$, is calculated based on [114] as

$$\frac{\mathrm{d}n_{iv}}{\mathrm{d}t} = \frac{2\pi D_{ig}^v \delta_b}{k_B T \zeta}(p - p_{eq}) \tag{4.17}$$

where n_{iv} (/) is the number of vacancies per intra-granular bubble, D_{ig}^v (m^2 s^{-1}) is the intra-granular vacancy diffusion coefficient, δ_b (m) is the radius of the equivalent Wigner-Seitz cell[21] (e.g., [28]) surrounding a bubble, k_B (J K^{-1}) is the Boltzmann constant, T (K) is the local temperature, and ζ (/) is a dimensionless factor calculated as [262]

$$\zeta = \frac{10\psi(1 + \psi^3)}{-\psi^6 + 5\psi^2 - 9\psi + 5} \tag{4.18}$$

where $\psi = R_b/\delta_b$ is the ratio between the radii of the bubble and of the cell. The present model for vacancy absorption/emission at intra-granular bubbles is a reformulation of the Speight and Beere model for behavior at grain boundaries of bubbles of circular projection (2D problem) [30, 114]. In particular, Eqs. 4.17, 4.18 represent the equivalent model for vacancy absorption/emission at spherical bubbles in the bulk (3D problem). The different dimensionality of the problem yields a different expression for ζ relative to [114]. Eq. 4.18 was first derived in [262] for the problem of pore growth in the UO$_2$ high burnup structure.

Considering a rearranged formulation of the van der Waals equation of state[22] and Eq. 4.16, the pressure of the gas in the bubble is

$$p = \frac{k_B T}{\Omega}\frac{\bar{n}}{n_{iv}} \tag{4.19}$$

The intra-granular bubble radius is

$$R_b = \sqrt[3]{\frac{3V_b}{4\pi}} \tag{4.20}$$

---

[21]The radius of the Wigner-Seitz cell is determined from the relationship $4/3\ \pi N\delta_b^3 = 1$.

[22]For xenon, the actual van der Waals equation of state can be reduced to Eq. 4.19, neglecting the pressure correction due to xenon covolume (e.g., [1]).

Finally, the fractional volume change due to intra-granular fission gas swelling is calculated as

$$\left(\frac{\Delta V_f}{V_f}\right)_{ig} = V_b N \tag{4.21}$$

4.3.2 Inter-granular model

The inter-granular component of the model for fission gas behavior in U_3Si_2 is based on the model originally developed for UO_2 in [34, 72], assuming that the same qualitative assumptions for gas behavior at grain boundaries apply to UO_2 and U_3Si_2. In particular, I consider the development of a population of lenticular bubbles at grain faces, bubble coalescence during bubble growth, and fission gas release following saturation of the grain boundaries [30, 34]. These similarities to UO_2 appear coherent when considering that both materials exhibit a polycrystalline structure under LWR conditions. They are also corroborated by the evidence from the metallographic images of U_3Si_2 irradiated at power reactor temperatures from [232].

The inter-granular model allows for the concurrent calculation of fission gas swelling due to grain-boundary bubbles and FGR through a direct description of bubble evolution [34]. The main features of the model are the following.

The absorption rate of gas at the grain-boundary bubbles is assumed to equal the arrival rate of gas at the grain boundaries [30, 215]. An initial number density of grain-boundary bubbles, $N_{gf,0}$, is considered, and further nucleation during the irradiation is neglected (one-off nucleation, e.g., [30]). All grain-boundary bubbles are considered to have, at any instant, equal size and equal lenticular shape of circular projection. The flux of gas atoms from the grain boundaries to the grain interior by irradiation-induced re-solution of grain-boundary bubbles is neglected, in line with [34, 64]. Grain-boundary bubble growth (or shrinkage) by inflow of gas atoms from within the grains and concomitant absorption (or emission) of vacancies from the grain boundaries is considered. The bubble growth/shrinkage rate is calculated as

$$\frac{dV_{gf}}{dt} = \omega\frac{dn_g}{dt} + \Omega\frac{dn_v}{dt} \tag{4.22}$$

where V_{gf} (m^3) is the bubble volume, ω (m^3) the van der Waals' volume of a fission gas atom, n_g (/) the number of fission gas atoms per bubble, Ω (m^3) the atomic (vacancy) volume in the bubble, and n_v (/) the number of vacancies per bubble. The gas atom inflow rate at the bubble, dn_g/dt, is obtained from Eq. 4.14. The vacancy absorption/emission rate at the bubble, dn_v/dt, is calculated using the model of Speight and Beere [114]

$$\frac{dn_v}{dt} = \frac{2\pi D_{gb}^v \delta_{gb}}{k_B T S}\left(p - p_{eq}\right) \tag{4.23}$$

where D_{gb}^v (m^{2}s^{-1}) is the vacancy diffusion coefficient along grain boundaries, δ_{gb} (m) the thickness of the diffusion layer in grain boundaries, and the parameter S (-)[23] depends on the fraction of grain faces covered by bubbles (fractional coverage) as detailed in [30]. The pressure of the gas in the bubble, p (Pa), is calculated based on the van der Waals equation of state as [30]

$$p = \frac{k_B T}{\Omega} \frac{n_g}{n_v} \tag{4.25}$$

The mechanical equilibrium pressure, p_{eq} (Pa), is given by the sum of the bubble surface tension force and the hydrostatic stress in the surrounding medium (analogous to Eq. 4.15). Given the volume (Eq. 4.22) of a lenticular bubble of circular projection, the bubble radius of curvature is

$$R_{gf} = \left(\frac{3 V_{gf}}{4\pi\varphi\left(\theta\right)} \right)^{1/3} \tag{4.26}$$

where $\varphi = 1 - 1.5 cos\left(\theta\right) + 0.5 cos^3\left(\theta\right)$ is the geometric factor relating the volume of a lenticular bubble to that of a sphere, and θ is the bubble semi-dihedral angle.

Grain-boundary bubble coalescence is described using an improved model of White [30, 34]. The variation rate due to coalescence of the bubble number density, N_{gf} (m^{-2}), is calculated as a function of the variation rate of the bubble projected area on the grain face, $A_{gf} = \pi R_{gf}^2$ (m^2). More details are given in [34]. A lower limit $N_{gf,low} = 10^{10}$ m^{-2} is set.

Under the above assumptions, the fractional fuel volume change due to grain-boundary fission gas swelling is calculated at each time step as

$$\frac{\Delta V}{V} = \frac{1}{2} \frac{3}{r_{gr}} N_{gf} V_{gf} \tag{4.27}$$

where V (m^3) is the fuel volume, r_{gr} (m) the grain radius, and $3/r_{gr}$ represents the grain surface to volume ratio.

Thermal FGR is modeled based on a principle of grain face saturation. More precisely, after the fractional coverage attains a saturation value, $F_{c,sat}$, further bubble growth is compensated by gas release in order to maintain the constant coverage condition

$$\frac{\mathrm{d}F_c}{\mathrm{d}t} = \frac{\mathrm{d}\left(N_{gf} A_{gf}\right)}{\mathrm{d}t} = 0 \qquad if\ \ F_c = F_{c,sat} \tag{4.28}$$

---

[23]As mentioned above, the parameter S depends on the geometrical representation of the emission/absorption phenomena. For behavior on a surface (grain boundary), the expression for S reads [30]

$$S = -\frac{(3 - F_c)(1 - F_c) + 2\ln F_c}{4} \tag{4.24}$$

where $F_c = N_{gf} A_{gf}$ (-) is the fractional coverage. Equation 4.24 is conceptually identical to Eq. 4.18, but considers an emission/absorption process constrained to a 2D geometry.

In the absence of specific experimental data for the saturation coverage in U_3Si_2, I choose $F_{c,sat} = \pi/4$, which corresponds to the theoretical, geometrical interlinkage condition for uniformly arranged bubbles of circular projection. This value has been used also for UO_2 [135], although more recent models generally adopt a lower value of 50% that is based on the empirical evidence available for UO_2 [30]. A specific investigation of the saturation coverage in U_3Si_2, e.g., by means of meso-scale techniques such as phase field modeling, would be useful to provide a more accurate saturation threshold. This improvement is being pursued in the near future. Also, at this stage, the model does not take into account the effect of as-fabricated porosity in fission gas behavior, i.e., gas trapping at fabrication pores.

Note that fission gas release and swelling are described as inherently coupled phenomena, as fission gas release from the grain faces counteracts bubble growth and thereby fission gas swelling.

4.3.3   Values for the model parameters

Nominal values and correlations used for the parameters of the model presented in Sections 4.3.1 and 4.3.2 are summarized in Table 4.2. These values are based either on the lower-length scale calculations performed in the present work (Section 4.2) or on information available from the literature. As significant uncertainties still exist in many of the parameters, a sensitivity analysis is performed in Section 4.5.

The adopted single gas atom diffusion coefficient, D is the one for the migration of Xe in a U (U 2a) vacancy assisted by a second U 2a vacancy along the c axis of the ideal U_3Si_2 unit cell. Indeed, this is the dominant mechanism over the temperatures of interest for LWR applications, as it is associated with a larger diffusivity compared to the other processes, as discussed in Section 4.2.1. For analogous reasons, for the intra-granular vacancy diffusion coefficient, D_{ig}^v, I chose the one for the U (U 2a) vacancy diffusion along the c-axis.

The nucleation factor, f_n, represents a sort of nucleation efficiency, i.e. the probability that, after impinging, two atoms actually form a dimer. For this parameter, I adopt a value within the accepted range for UO_2, e.g. [75]. Indeed, the nucleation factor is one of the most uncertain parameters (even for UO_2), and specific information for U_3Si_2 is missing. Investigation of the impact of this parameter on the results is included in the sensitivity analysis presented in Section 4.5.

To the best of my knowledge, no values for the grain-boundary vacancy diffusion coefficient, D_{gb}^v, for U_3Si_2 under LWR conditions are available at this time. As a preliminary approach, I choose to employ the intra-granular vacancy diffusion coefficient derived in Section 4.2.1 and reported in Table 4.2, multiplied by a scaling factor equal to 10^6. The magnitude of the scaling factor is related to atomic jump frequencies at grain boundaries, which are roughly 10^6 times higher than jump frequencies for lattice atoms [215].

For the semi-dihedral angle of grain-boundary bubbles, I tentatively use a value

Table 4.2: Values adopted for the parameters of the models.

Symbol	Value or expression	Reference
D	$D_0 \exp(-\Delta H_a/kT)$	Section 4.2.1 and Ref. [245]
	$D_0 = 5.91 \cdot 10^{-6} \text{ m}^2 \text{s}^{-1}$	
	$\Delta H_a = 4.41 \cdot 10^{-19} \text{ J}$	
f_n	10^{-4}	e.g., Veshchunov [75]
α_0	$2.80 \cdot 10^{-25} \left(\dfrac{5 \cdot 10^{-10}}{R_b} \right)^{0.23} \text{ m}^{-3}$	Section 4.2.2
γ	1.16 J m^{-2}	Miao et al. [42, 263]
D_{ig}^v	$D_{ig,0}^v \exp\left(-\Delta H_{a,ig}^v/kT\right)$	Section 4.2.1 and Ref. [245]
	$D_{ig,0}^v = 3.35 \cdot 10^{-6} \text{ m}^2 \text{s}^{-1}$	
	$\Delta H_a = 4.63 \cdot 10^{-19} \text{ J}$	
Ω	$4.09 \cdot 10^{-29} \text{ m}^3$	Kogai [135]
ω	$8.5 \cdot 10^{-29} \text{ m}^3$	-
D_{gb}^v	$10^6 \cdot D_{ig}^v$	Olander and Van Uffelen [215]
δ_{gb}	$5 \cdot 10^{-10} \text{ m}$	Kogai [135]
θ	$50°$	Assumption

of 50°, commonly accepted for UO_2 (e.g., [30]). Using a specific U_3Si_2 value, which can be derived from recent MD calculations of grain boundary and surface energies in [264], is planned for the near future.

4.4 Irradiation experiment simulation

In this Section, I present and discuss the simulation of the U_3Si_2 irradiation experiment from Shimizu [232]. To the best of the authors' knowledge, this is the only in-pile experiment on U_3Si_2 fuel under temperatures and irradiation conditions compatible with commercial LWRs and whose details and data are available in the open literature. The simulation is intended to demonstrate a physically meaningful representation of fission gas behavior of U_3Si_2 under LWR conditions with the model presented in Section 4.3. The more substantial validation of the model will require a larger amount of experimental data and will be the subject of future work as new experiments are performed, e.g., in the framework of the AFC.

Table 4.3: Irradiation conditions for the fuel slug labeled specimen #14 from the AI-7-1 irradiation experiment.

Irradiation conditions	
Fresh fuel stoichiometry (wt.%)	7.08
Linear heat rate ($\mathrm{kW\,m^{-1}}$)	37.4
Burnup ($\mathrm{GWd\,tU^{-1}}$)	6.0
Average centerline temperature (K)	1050
Average surface temperature (K)	850

4.4.1   Description of the analyzed experiment

The considered experiment, referred to as AI-7-1 [232], was performed by Atomics International to determine U_3Si_2 irradiation behavior characteristics, i.e., dimensional stability and fission gas release. The irradiation involved a single fuel rod. The fuel column (H30.5 cm, ⌀0.889 cm) was made of six slugs of 10% ^{235}U enriched, slightly hypo-stoichiometric U_3Si_2. The cladding was stainless steel (SS 304) and the gap between the fuel and the cladding was filled with sodium to provide efficient heat transfer. The fuel was irradiated to a maximum average burnup of 7.3 $\mathrm{GWd\,tU^{-1}}$ at a power of 46 $\mathrm{kW\,m^{-1}}$ with a maximum center and surface temperatures of 1230 K and 970 K, respectively.

In particular, in this work I focus on one of the slugs composing the fuel column, labeled as specimen #14, whose irradiation conditions are summarized in Table 4.3. I chose to focus on this slug for several reasons:

- The specimen did not crack under irradiation, allowing for a higher precision in determining the dimensional changes of the fuel.

- The thermocouple installed near the slug exhibited a stable behavior throughout the irradiation, enabling a proper estimation of local fuel temperature.

- After irradiation, the slug was sectioned and a metallographic image in the fuel central region was taken. Based on this metallographic image, an estimation of local fuel swelling due to fission gas bubbles was possible and has been performed [265].

Detailed PIE, have been produced during the experimental campaign. Those data have been complemented by recent image analyses to determine gaseous swelling and grain size [265]. The original PIE data reported by Shimizu on specimen #14, together with the recent data from image analysis according to [265], are reported in Table 4.4. This first set of experimental data is used here for comparison with model calculations.

Table 4.4: PIE and image analysis results for fuel slug #14 from the AI-7-1 irradiation experiment [232].

Quantity	Value	Reference
Final local fuel stoichiometry (wt.%)	6.79	[232]
Overall density variation (%)	-12.6	[232]
Specimen length variation (%)	3.0	[232]
Specimen diameter variation (%)	3.0	[232]
Fission gas release (%)	2.6	[232]
Final grain radius, 3D (µm)	28±7	[265]
Intra-granular gaseous swelling (%)	2.9	[265]
Inter-granular gaseous swelling (%)	9.2	[265]

4.4.2   Set-up of calculations

I performed the calculations using a stand-alone C++ code for the fission gas behavior model presented in Section 4.3. The irradiation conditions applied in my simulations are coherent with those reported in [232] and summarized in Table 4.3. In particular, I performed a local analysis for the centerline portion of the specimen, where local experimental data from image analysis [265] are available. Local temperature considered for the simulation is 1050 K (Table 4.3).

4.4.3   Results and discussion

In Figure 4.3, I compare the results of the simulations in terms of fission gas release and gaseous swelling to the experimental data. FGR is defined as the ratio of the released to generated gas, whereas gaseous swelling is calculated as defined in Section 4.3 and is the sum of the intra- and inter-granular contributions. FGR (dashed-blue line) exhibits an incubation behavior [266], with no release being observed until the grain-boundary bubble coverage attains a saturation level. Also, as fission gas swelling and release are described as inherently coupled in the model (Section 4.3.2), a change of the swelling rate can be observed at the onset of FGR. In particular, the swelling rate is reduced by loss of gas from the grain faces as FGR takes place. The agreement between calculations and the experimental results appears reasonable for a preliminary model. Note that the FGR comparison is not fully consistent, as the calculation refers to the centerline (hottest) portion of the specimen only. As expected, FGR is thus over-estimated.

In Figure 4.4, I report results specific to the intra-granular model (Section 4.3.1). In particular, the calculated number density and radius of intra-granular fission gas bubbles are shown. The results point out a lower number density and a higher
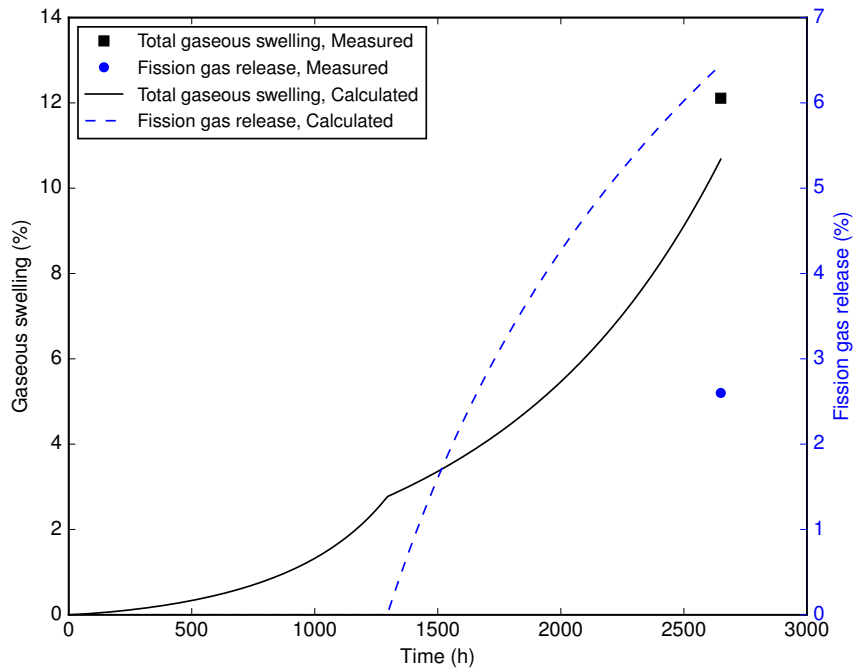
Figure 4.3: FGR and total gaseous swelling as a function of irradiation time for specimen # 14 of the AI-7-1 experiment. Calculation results and experimental data are included.
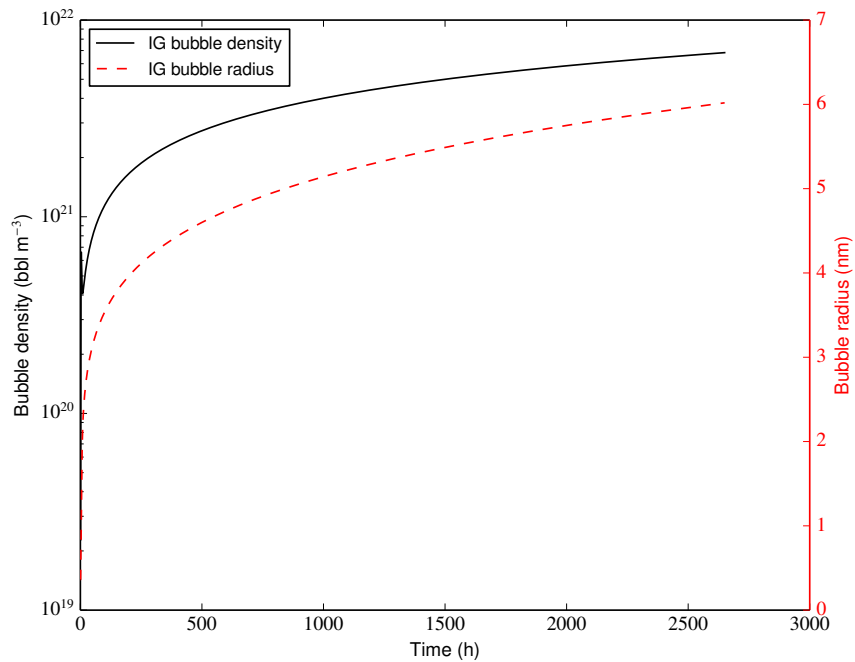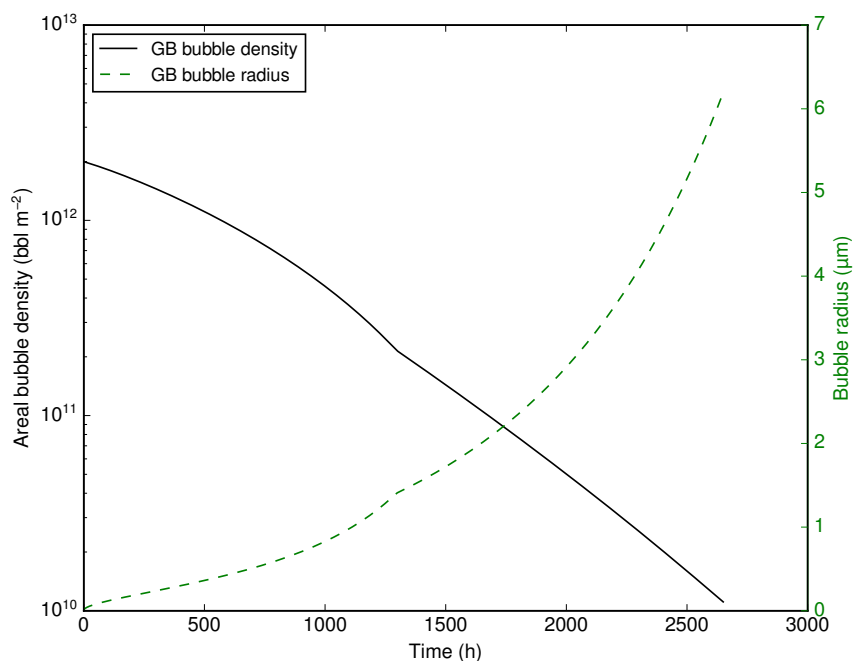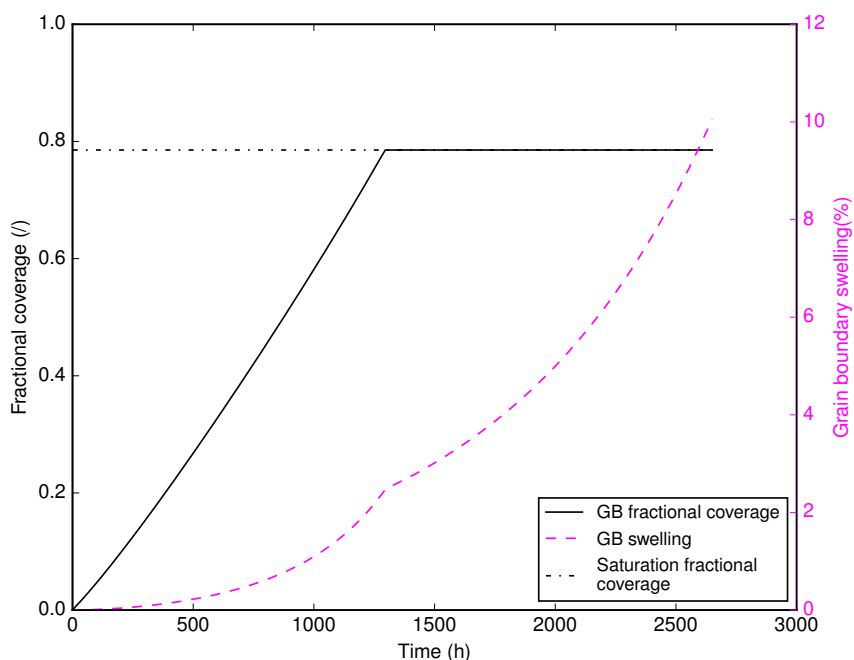

Figure 4.4: Calculated volumetric number density and radius of intra-granular (IG) bubbles as a function of irradiation time for specimen # 14 of the AI-7-1 experiment.

(a)

(b)

Figure 4.5: Calculated areal number density and radius of curvature (a) of grain-boundary (GB) bubbles as a function of time for specimen # 14 of the AI-7-1 experiment. Grain-boundary fractional coverage and swelling (b) as a function of time. The saturation fractional coverage of $\pi/4$ [135] is also reported.

radius of intra-granular bubbles compared to UO_2 under operational LWR conditions (e.g., [26, 56]). This appears consistent with the metallographic images from [232] and

Table 4.5: Parameters considered in the sensitivity analysis and corresponding ranges of variation.

Parameter	Nominal value	Scaling factor range
Intra-granular diffusion coefficient, atoms (m s^{-2})	$5.91 \cdot 10^{-6} \exp(-4.41 \cdot 10^{-19}/k_B T)$	$[0.1; 10]$
Intra-granular diffusion coefficient, vacancies (m s^{-2})	$3.35 \cdot 10^{-6} \exp(-4.63 \cdot 10^{-19}/k_B T)$	$[0.1; 10]$
Nucleation factor (/)	10^{-4}	$[10^{-5}; 10^2]$
Re-solution rate (s^{-1})	$2.80 \cdot 10^{-25} \left(\dfrac{5 \cdot 10^{-10}}{R_b} \right)^{0.23} \cdot \dot{F}$	$[0.1; 10]$
U$_3$Si$_2$/gas specific surface energy (J m^{-2})	1.16	$[0.5; 1.5]$
Inter-granular diffusion coefficient, vacancies (m s^{-2})	$10^6 \cdot D_{ig}^v$	$[10^{-2}; 10^2]$
Inter-granular bubbles initial number (bbl m^{-2})	$2 \cdot 10^{12}$	$[10^{-3}; 10^3]$
Inter-granular bubbles dihedral angle (deg)	50	$[0.5; 1.5]$
Saturation coverage of grain faces (/)	$\pi/4$	$[\dfrac{2}{\pi}; 1]$

with the higher diffusivities of gas atoms and vacancies in U$_3$Si$_2$ compared to UO$_2$ as indicated by the lower-length scale calculations performed in this work (Section 4.2).

Figure 4.5 reports results specific to the inter-granular model (Section 4.3.2). In Figure 4.5a, I report the time-evolution of the areal number density and radius of curvature of grain-boundary fission gas bubbles. The decrease in the bubble density is due to the progressive bubble coalescence during growth. Correspondingly, the bubble radius increases. The evolution during irradiation of grain-boundary fractional coverage and grain-boundary swelling are illustrated in Figure 4.5b. FGR commences at the attainment of saturation coverage (see Fig. 4.3), and the swelling rate correspondingly decreases.

4.5 Sensitivity analysis

The irradiation experiment simulation presented in Section 4.4 is complemented with a sensitivity analysis aimed at assessing the impact on the simulation results of the model parameters. This sensitivity analysis is essential for at least two reasons: (i) in view of the lack of data for U$_3$Si$_2$, in the selection of some parameters (i.e., nucleation factor, diffusion coefficient of vacancies at grain boundaries, inter-granular bubbles dihedral angle) assumptions were made; (ii) a sensitivity analysis can provide guidance for future research on characterization of the physical mechanisms and the associated engineering parameters, including both experimental and lower-length scale modeling efforts. In this Section, I present the methodology employed for the sensitivity analysis and discuss the results obtained.

The parameters considered in the sensitivity analysis are reported in Table 4.5

along with the considered nominal values and ranges of variation.

I performed the analysis for various temperatures, i.e., from 800 to 1200 K at intervals of 50 K. For the other boundary conditions (including irradiation time, fission rate, grain size) I adopted the same as in Section 4.4. For each one of the considered temperatures, I performed 10,000 simulations, randomly sampling the scaling factors in the ranges specified in Table 4.5, i.e., adopting a Monte Carlo approach. Uniform distributions were assumed for the parameters. The tool employed to carry out the sensitivity analysis is the RAVEN statistical analysis framework [267, 268], developed at INL. Considered figures of merit for the analysis are calculated fission gas release, intra-granular swelling and inter-granular swelling.

In Figures 4.6-4.8, I report the results of the sensitivity analysis in terms of Pearson correlation coefficient and normalized sensitivity coefficient on the three selected outputs, namely fission gas release, intra- and inter-granular swelling. The Pearson coefficient indicates how strong the correlation of a certain parameter is with respect to the chosen figure of merit, while the normalized sensitivity coefficient provides a measure of the relative variation of the figure of merit with respect to the variation of a specific parameter.

The re-solution rate and the intra-granular nucleation factor exhibit a strong correlation with FGR (Figure 4.6) on all the considered temperature range, being characterized by the highest Pearson coefficient. However, only the re-solution rate is associated with an appreciable sensitivity coefficient. Results suggests that the choice of the nucleation factor, which involved a strong assumption based on the experience on UO_2, has a low impact on the calculation.

As shown in Figure 4.7, the calculated intra-granular swelling results are mostly sensitive to the re-solution rate and specific surface energy, while the dominant parameters for the calculated inter-granular swelling (Figure 4.8) are the grain-boundary bubbles dihedral angle and saturation coverage. The estimation of the saturation coverage in U_3Si_2 through phase field techniques or experimental measurements, complemented by the recent MD calculations for grain boundary and surface energies [264], will be used to improve the presented inter-granular model in the near future.

In Figure 4.9, I show the sensitivity coefficients calculated at the same temperature as the simulation in Section 4.4, i.e., 1050 K. It is noted that the vacancy diffusion coefficients are associated with low sensitivity coefficients, indicating that both intra- and inter-granular bubbles rapidly reach the equilibrium pressure and size (Section 4.3) due to the high mobility of vacancies in U_3Si_2.
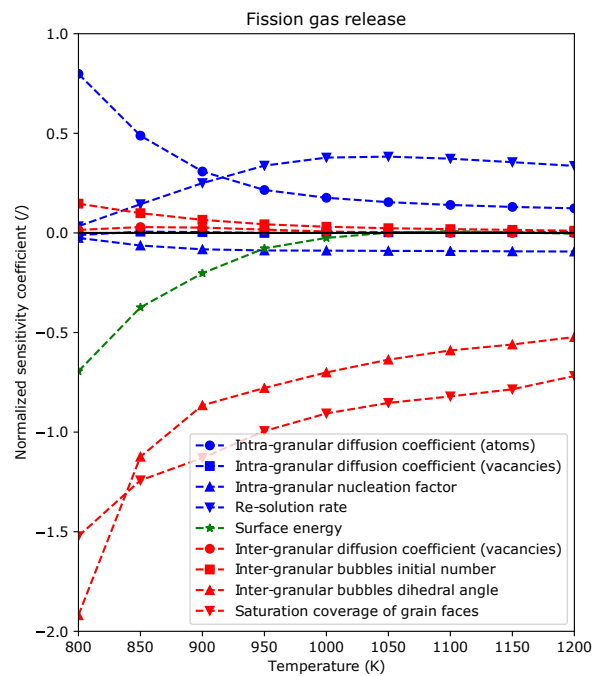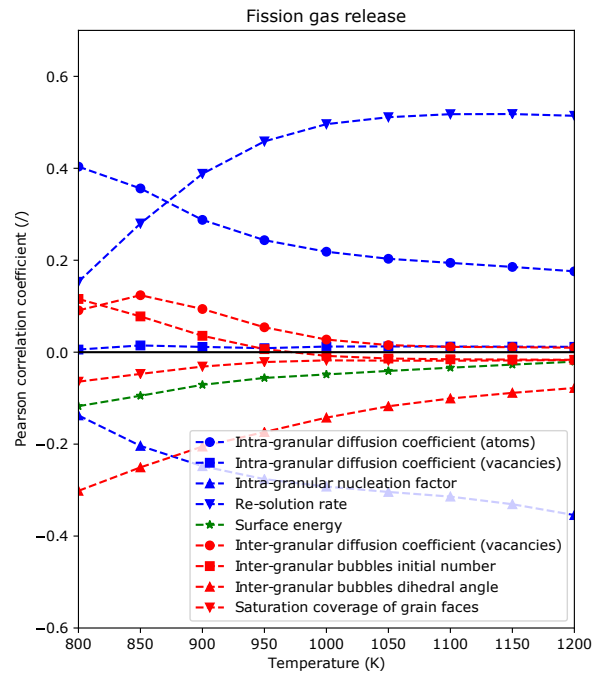
Figure 4.6: Pearson coefficient (a) and normalized sensitivity coefficient (b) of the selected parameters to fission gas release at various temperatures.
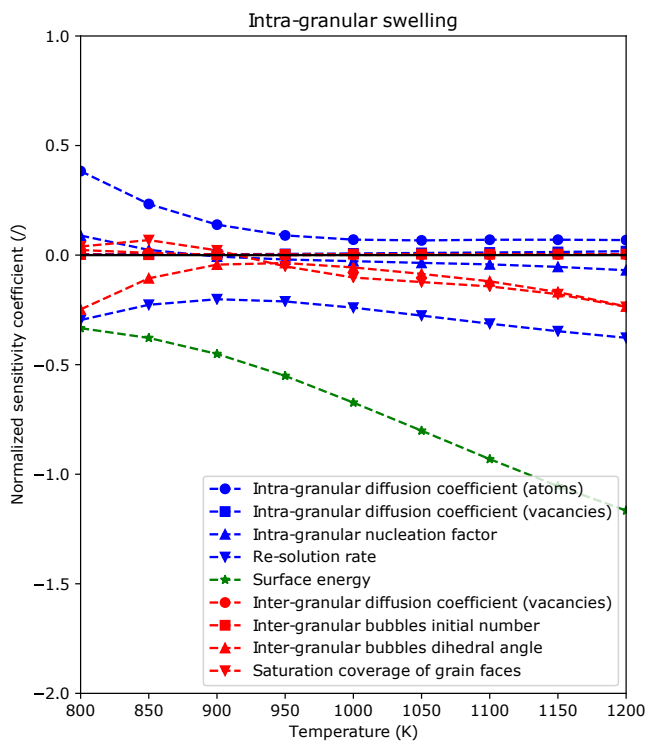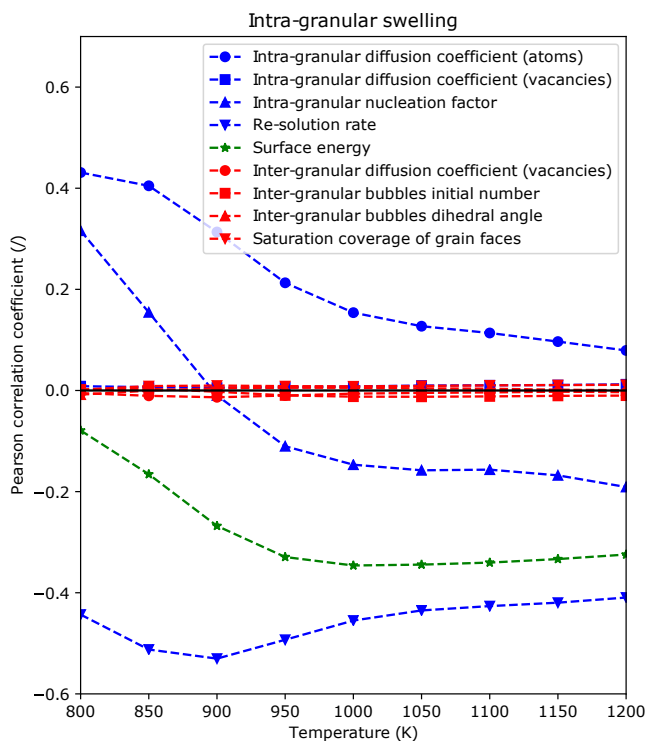
Figure 4.7: Pearson coefficient (a) and normalized sensitivity coefficient (b) of the selected parameters to intra-granular gaseous swelling at various temperatures.
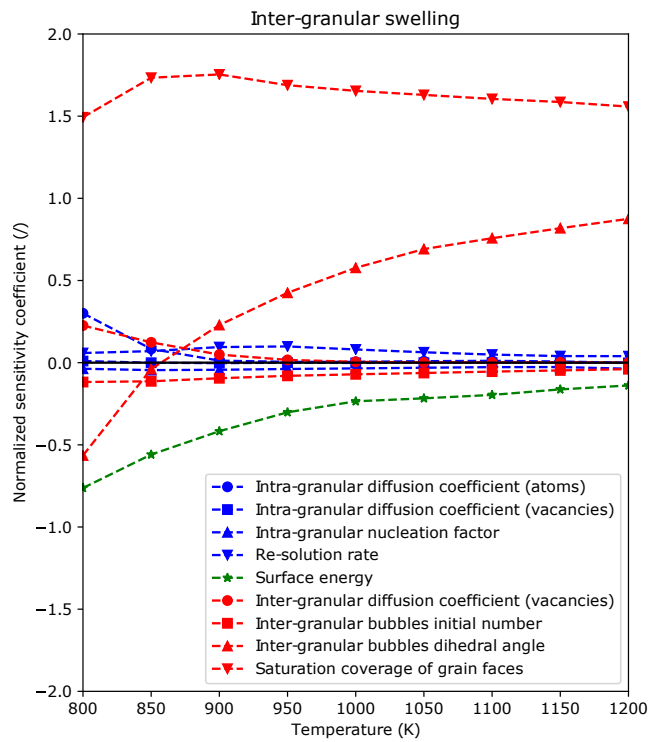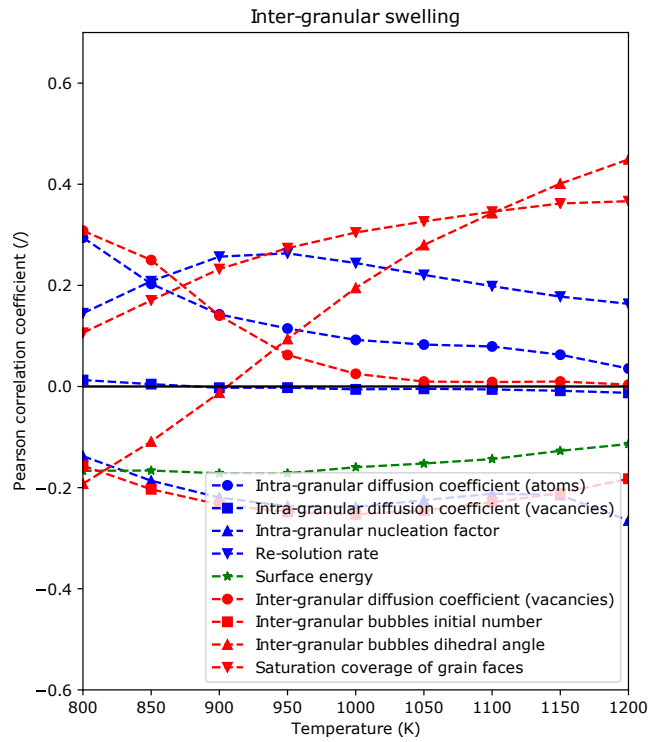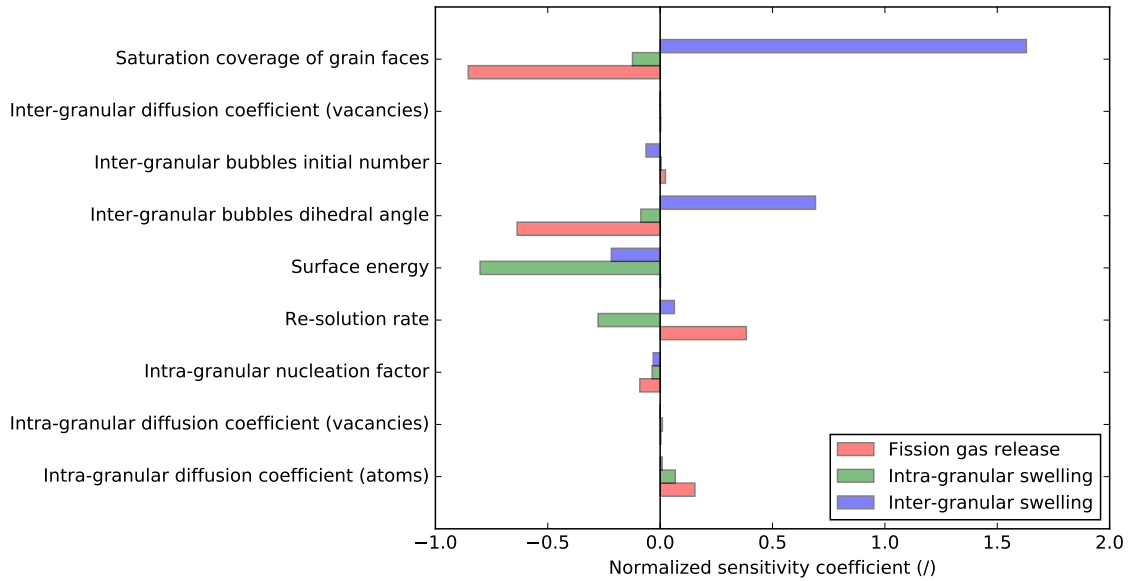
Figure 4.8: Pearson coefficient (a) and normalized sensitivity coefficient (b) of the selected parameters to inter-granular gaseous swelling at various temperatures.

Figure 4.9: Normalized sensitivity coefficients of the selected parameters to fission gas release, intra- and inter-granular swelling at the temperature of 1050 K.

4.6   Closing remarks

In this Chapter, I presented a model for fission gas behavior in U_3Si_2 under LWR conditions. The model includes components for intra-granular and grain-boundary behavior of fission gases and describes the evolution of fission gas bubbles within the grains and at grain boundaries, intra-granular gas atom diffusion, and fission gas release. The intra-granular component describes the evolution under irradiation of intra-granular fission gas bubbles and gas atom diffusion to grain boundaries. This model adopts a single-size approach for intra-granular bubbles in order to reduce complexity relative to detailed cluster dynamics approaches. However, the model is derived from the master equations of cluster dynamics and retains a physical representation of bubble nucleation, re-solution, and gas atom trapping at bubbles. Moreover, the model is suitable for application to every material in which the re-solution and nucleation of fission gas atoms show a homogeneous characteristic, hence could be extended for example to the analysis of fission gas behavior in metal fuels. In order to fill the gap in the experimental data available for U_3Si_2 under LWR conditions, I adopted a multiscale approach whereby lower-length scale modeling for the parameters is used to inform the engineering scale calculation. In particular, intra-granular single gas atom diffusion coefficient and point defect properties were derived through DFT calculations, and the re-solution parameter through BCA calculations. The model was applied to the simulation of an experiment for U_3Si_2 at power reactor temperatures available in the literature, pointing out a physically meaningful representation of fission gas swelling and release. Moreover, I carried out a sensitivity analysis to assess the importance of various model parameters in the calculated fission gas swelling and release. On the one hand, the saturation coverage

of grain faces, the re-solution parameter, and the U_3Si_2/gas specific surface energy emerged as a set of high-priority parameters to be further investigated. On the other, the sensitivity analysis indicated that some of the most uncertain parameters of the model (i.e. the intra-granular nucleation factor and the grain-boundary vacancy diffusion coefficient) are associated with weak Pearson and sensitivity coefficients over the considered temperature range.

I conclude that the work (i) demonstrated an operational multiscale modeling approach for fission gas behavior in U_3Si_2, (ii) provided a modeling framework with a promising potential for the calculation of fission gas swelling and release in U_3Si_2 under LWR conditions for engineering fuel analysis, and (iii) provided indications that can help addressing future research on the characterization of the parameters through a sensitivity analysis. The model can be progressively improved as new data become available from theoretical and experimental research.

The model of fission gas behavior in U_3Si_2 presented in this Chapter is currently available in the BISON FPC of Idaho National Laboratory.

Further developments of the presented FGB model for U_3Si_2 under LWR conditions should include a refinement of the considered physical processes involved in determining the intra-granular gas behavior, e.g. considering the impact of thermal re-solution and, in case, accounting for it. Furthermore, exploiting new atomistic and meso-scale modeling results is envisaged in order to account for irradiation-driven lattice diffusion of fission gas atoms, and to include improved estimations for the grain-boundary bubble coverage at saturation and for grain-boundary and surface energies.

CHAPTER 5. CONCLUSIONS AND PERSPECTIVES

"Dejo a los varios porvenires (no a todos) mi jardín de senderos que se bifurcan"

J. L. Borges, *El jardín de senderos que se bifurcan – Ficciones*, 1944

The goal of this thesis work is to develop physics-based models describing fission gas behavior in nuclear fuels oriented to application in fuel performance codes. The developed models deal with behavior under harsh conditions of conventional (UO_2) nuclear fuel (i.e., high temperature transients and/or high burnup conditions) and with fission gas behavior in novel materials under consideration as candidate substitutes of the conventional fuel system (U_3Si_2). I leveraged a multi-scale mechanistic modeling approach (i.e., I developed models accounting for the relevant physical phenomena governing FGB bridging different scales of modeling), allowing for a description of nuclear fuel performance in a wide spectrum of conditions, spanning from normal operating to transient and accident conditions, and addressing new materials behavior, both conditions to which empirical models cannot be applied or for which experimental data are not available.

I addressed the goal of my PhD thesis developing three FGB models: two conceived to describe the behavior of conventional nuclear fuel in extreme conditions, namely, a model describing intra-granular fission gas bubbles coarsening (i.e., abnormal growth) in high temperature conditions and a model describing the HBS formation and porosity evolution, and the third model to tackle intra- and inter-granular FGB in uranium silicide, a novel LWR fuel concept.

The common features among the developed models are:

(i) The chosen modeling approach, which demonstrates how more mechanistic modeling is the only route towards the description of FGB where no experimental data are available to draw empirical models (i.e., for extreme fuel conditions and new fuel concepts) and to describe FGB in transient conditions.

(ii) The perspective of including the models in FPCs. This latter aspect constitutes a crucial topic, since developed models must respect a compromise between the detail of physical description and a reasonable computational effort.

The developed models represent a consistent step forward with respect to the state of the art, since some of these phenomena are accounted for by empirical models (with no or very limited non-stationary capabilities) or are not accounted at all, preventing FPCs to be satisfactorily equipped to analyze conventional nuclear fuels in extreme scenarios as well as new fuel concepts.

I developed and implemented the models in the SCIANTIX code, which I also coupled to the TRANSURANUS fuel performance code, making available *de facto* the developed models also in the framework of the overall thermo-mechanical analysis of the fuel rod performed by TRANSURANUS. I validated each model in SCIANTIX by comparing its results against available separate-effect experiments, showing a satisfactory predictive capability of the developed FGB models, surpassing the state-of-the-art ones.

The inclusion of the models in the SCIANTIX code represents another strength of the thesis work. In fact, SCIANTIX being an open source code, the developed models would be made available to the general public and to a wide spectrum of fuel performance codes.

All the models developed in the thesis have been included in fuel performance codes, either directly (i.e., I implemented the intra-granular bubble coarsening and uranium silicide models directly in the BISON code) or via the coupling of SCIANTIX with TRANSURANUS.

As evolution equations account for physical phenomena, the modeling strategy allows for effectively transferring the models to other materials with minor modifications in the physical parameters but preserving the fundamental equations. In this picture, the application of the developed models for UO_2 to other oxide fuel systems (such as MOX or $(U,Pu)O_2$), or to uranium silicide, is of sure interest, together with the application of uranium silicide models to metallic fuel concepts (e.g., to U-Pu-Zr alloys considered for application in sodium fast reactors).

To summarize, the main outcomes of my PhD thesis work are:

- The development and validation of more mechanistic models aimed at filling gaps in state of the art to describe FGB in uranium dioxide in extreme conditions (i.e., high temperature transients and high burnup conditions).

- The development of mechanistic models describing FGB in a novel, accident-tolerant fuel material (i.e., uranium silicide) to boost its design and analysis phase.

- The introduction of the developed models in engineering-scale fuel performance codes. The models are made available to the codes either via a direct implementation into the code itself (which is the case of the model introduced in the BISON code), either via the coupling of SCIANTIX with the TRANSURANUS code.

The latter bullet represents the main outcome of this thesis work from an engineering perspective, i.e., providing fundamental tools for the analysis of nuclear fuel behavior to fuel performance codes.

As for future developments of the presented work, many routes arise. First, the models may be complemented with helium behavior models. In fact, due to its high solubility in the fluorite phase of uranium dioxide (and presumably in uranium silicide as well), He behavior is featured by additional mechanisms governing the intra- and inter-granular behavior. This aspect becomes of the greatest importance when uranium-plutonium mixed oxide fuels (possibly bearing minor actinides as Np or Am)

are considered, for both in-pile and storage conditions. Moreover, a comprehensive model for fission products behavior calls for the inclusion of non-inert fission products which can be found in the gas phase at certain temperatures (like cesium or iodine), and more in general the integration of FGB models to a thermochemical description of the fuel system.

Second, the HBS model could be developed in the present formulation by considering higher order pore interactions (i.e., triple impingements) and considering the polydispersed pore size distribution. Considering two-species (gas atoms and vacancies) master equations as a starting point for the Fokker-Planck expansion is an additional development path of the present model for the HBS porosity. Indeed, it should be complemented with a description of the release of fission gas stored in the HBS porosity under accident conditions (e.g., in loss of coolant accidents or reactivity-initiated accidents), given its pivotal role in determining fuel rod internal pressure and hence cladding deformations. Moreover, the methodology employed to estimate the central moments of the pore size distribution could be applied to the intra-granular bubble model, for both bulk and dislocation bubbles.

Third, as computational or experimental evidences on HBS formation in uranium silicide would arise, an application of this model to the analysis of high burnup uranium silicide fuel is of interest, as well as HBS modeling inclusion in the analysis of fast reactor $(U,Pu)O_2$ fuel.

Fourth, the continuous development and validation of SCIANTIX have to be considered and pursued, in order to enlarge its modeling capabilities, to strengthen its validation database, demonstrating its wide application range. This would contribute to reinforce the SCIANTIX code, allowing for its exploitation in the framework of industrial fuel performance codes and pursuing a mechanistic and multi-scale modeling approach which could combine the theoretical work done at various modeling scales and introduce it in the field of FPCs. Moreover, implementation of the SCANTIX code is also underway in the GERMINAL code of the Commissariat à l'énergie atomique et aux énergies alternatives (CEA) and planned in the OFFBEAT code of the École Polytechnique Fédérale de Lausanne (EPFL).

As for the assessment side, comparison of the models included in fuel performance codes against integral irradiation experiments would help to assess the impact of these models on the overall fuel rod thermo-mechanical analysis. On the other hand, the comparison of stand-alone calculations of SCIANTIX to other meso-scale codes (such as the MFPR-F code, developed at Institut de radioprotection et de sûreté nucléaire (IRSN), France), designed with similar purposes, would be an important step to assess the predictive capabilities of the codes and possible development routes.

APPENDIX. SCIANTIX: AN OPEN SOURCE CODE FOR FISSION GAS BEHAVIOR MODELING DESIGNED FOR NUCLEAR FUEL PERFORMANCE CODES

"E l'infinita luce della steppa un po' pedemontana
Mi ricorda i tempi in cui io mi pensavo un'italiana"

—————————————

D. Panizza (Pop X), *Sibillini*, 2014

Abstract

In this Appendix, I present SCIANTIX, an open source 0D stand-alone computer code designed to be included/coupled as a module in/with existing fuel performance codes. The models currently available in SCIANTIX cover intra- and inter-granular inert gas behavior in UO_2, and high burnup structure formation as well. Showcases of validation in both constant and transient conditions are presented. As for the numerical treatment of the model equations, SCIANTIX is developed with full numerical consistency and entirely verified with the method of manufactured solutions – verification of different numerical solvers is also showcased in this Appendix. The modeling features presented in this Appendix refer to the 1.0 version of the code, whereas the work presented in the bulk of this thesis will constitute the basis for a forthcoming release of the code.

Introduction

As I already discussed in the Foreword of the thesis and demonstrated throughout it, mechanistic approaches to FGB modeling offer evident advantages when compared to correlation-based ones. Different codes dealing with physics-based modeling of fission gas behavior have been developed [24, 27, 31–33, 73, 136, 269–271]. These codes are either stand-alone or conceived to be used as fission gas behavior modules within fuel performance codes (e.g., SIFGRS [72] for BISON [53, 271], FISPRO2 [34, 127] for TRANSURANUS [12, 73], CARACAS [24] for ALCYONE [185, 272], GRSW-A [32, 273] for FALCON [180, 274], and MFPR [31] for SFPR [275] and BERKUT [44]).

To carry out the development, testing, and separate-effect validation of the models presented in this thesis, I employed the SCIANTIX code [276], which I will present in this Appendix. The SCIANTIX code has been developed in the Nuclear Reactor Group at POLIMI with a twofold objective:

- It aims at effectively bridging lower-length scale and the engineering scale of fuel performance code, feeding the latter with theoretical and experimental knowledge about fission gas behavior mechanisms inferred by the former approaches. Thus, when possible, the use of physics-based models is preferred over correlation-based approaches, but always in line with the computational requirements of fuel performance codes.

- It aims at being usable as a stand-alone code for the simulation of separate effect experiments at the fuel-grain scale involving inert gas behavior, both supporting the design of the experiment itself and the interpretation of the results.

In order to target these objectives, SCIANTIX has specific software features and embodies a consistent set of physics-based models. Moreover, SCIANTIX is available as open source under MIT license [276], greatly easing its usage as fission gas behavior module in existing fuel performance codes. Because of this licensing choice, all the models implemented in the currently available version of SCIANTIX are already published and validated. For this reason, after a summary of SCIANTIX validation, a showcase of selected simulations detailing the behavior of the main models are presented. Lastly, I provide an overview of the currently ongoing developments in SCIANTIX outside this thesis work (all the modeling effort done in this thesis will eventually be released in SCIANTIX).

Flow chart and numerical features

SCIANTIX is inherently designed as a module ready to be included/coupled with existing fuel performance codes (even in its stand-alone structure). For this reason, the flow chart reported in Fig. A.1 is divided in two parts: (1) on the left, the external
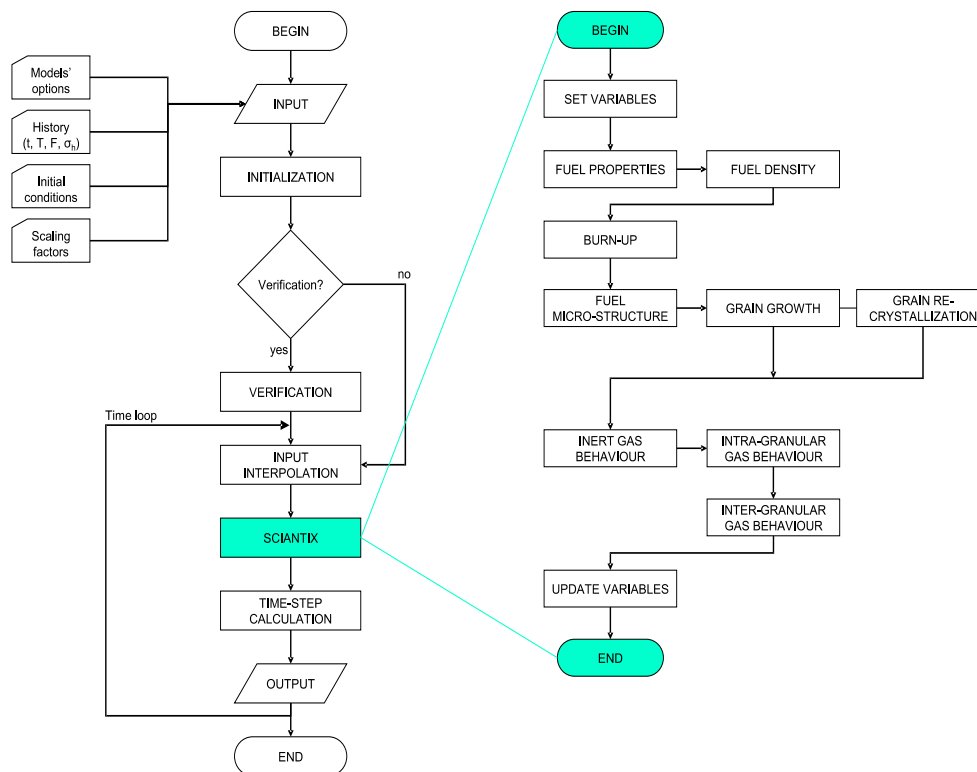
Figure A.1: Flow chart of SCIANTIX, highlighting the division between the external driver (parent code) and the meso-scale module. This flow chart is designed to ease inclusion of SCIANTIX in fuel performance codes.

driver (referred to as parent code) and on the right (2) the SCIANTIX module itself. The parent code performs several fundamental operations, e.g., inputs reading, output printing, and time stepping. As shown in Figure A.1, beside model options, initial conditions of the state variables (i.e., quantities evolving continuously in time), and possible scaling factor for sensitivity/uncertainty purposes, the parent code performs the interpolation of the simulation history quantities (i.e., temperature, fission rate density, and hydrostatic stress) in the specified time intervals. In particular, the parent code linearly interpolates the history quantities between two consecutive time points, dividing the time step in a number of sub-timesteps, chosen *a priori*. In such sub-intervals, the SCIANTIX module performs the incremental calculation of the evolution of physical state variables (e.g., grain radius, inert gas concentrations, gaseous swelling), updating the values of these variables in the parent code. This structure allows for straightforward coupling within fuel performance codes [6].

All the differential equations considered in the models implemented in SCIANTIX are solved with an implicit A-stable first order scheme, i.e., backward Euler[24].

---

[24] It is worth noting that several models available in SCIANTIX are nonlinear, with the main

Table A.1: Enumeration of the solvers available in SCIANTIX and corresponding order of convergence obtained through the MMS method.

Solver	Class of equations	Order of convergence
Integrator	$dy/dx = S$	1
Decay	$dy/dx = -\lambda y + S$	1
Binary interaction	$dy/dx = -ky^2$	1
Limited growth	$dy/dx = -M/y + S$	1
Spectral diffusion	$dy/dx = D\nabla^2 y + S$	2
FORMAS	$dy/dx = D\nabla^2 y + S$	2

Nevertheless, all the numerical solutions are consistent, i.e., have the error decreasing proportionally with the decrease in time step. The numerical solvers are all collected in an independent part of the code and can be called for in the different models. This allows for a complete verification of the code through the verification - once and for all - of the numerical solvers and allows the developers of physical models to focus on the physics itself instead of on the numerical issues. Table A.1 reports all the solvers currently available in SCIANTIX.

Verification is performed via the Method of Manufactured Solutions (MMS) [279]. Compared to other more arbitrary verification strategies (e.g., trend tests and comparisons evaluated by expert judgment) MMS provides a more rigorous verification framework. The Method of Exact Solutions (MES) is preferable to MMS if exact analytic solutions are available for the specific problem to be solved, which is not the case for the models available in SCIANTIX[25] and for many scientific codes as well. For these reason, MMS is recommended for the verification of scientific software [279, 280]. The steps required to apply MMS to verify a numerical solver are depicted in Fig. A.2. SCIANTIX can perform the verification – selection block (diamond shaped) in the flow chart reported in Fig. A.1 – of all the selected solvers prior to the simulation, producing dedicated verification outputs. The verification outcome for all the solvers is collected in Table A.1.

Limited computational time is a fundamental requirement for a multi-scale module like SCIANTIX, which has the engineering goal of being used within fuel performance codes. In fact, when coupled with a fuel performance code, SCIANTIX represents a local (or point) model to be called at each mesh point, at each convergence iteration (since gaseous swelling and fission gas release feedback the thermomechanical behavior of the fuel rod), and at each time step. Considering these considerable number of calls, SCIANTIX is designed to have a computational time in the order of milliseconds per

---

source of non-linearity arising from the time-variation of the parameters. Dedicated approaches developed to handle this type of non-linearity are currently available, and applied in fuel performance codes especially for the solution of the fission gas diffusion equation [260, 277, 278]. These approaches are not applied in SCIANTIX, in order to preserve the consistency of all the numerical solutions in the code.

[25] The analytic solution is generally well known for constant conditions, but time-varying situations occur in practically all the simulations.
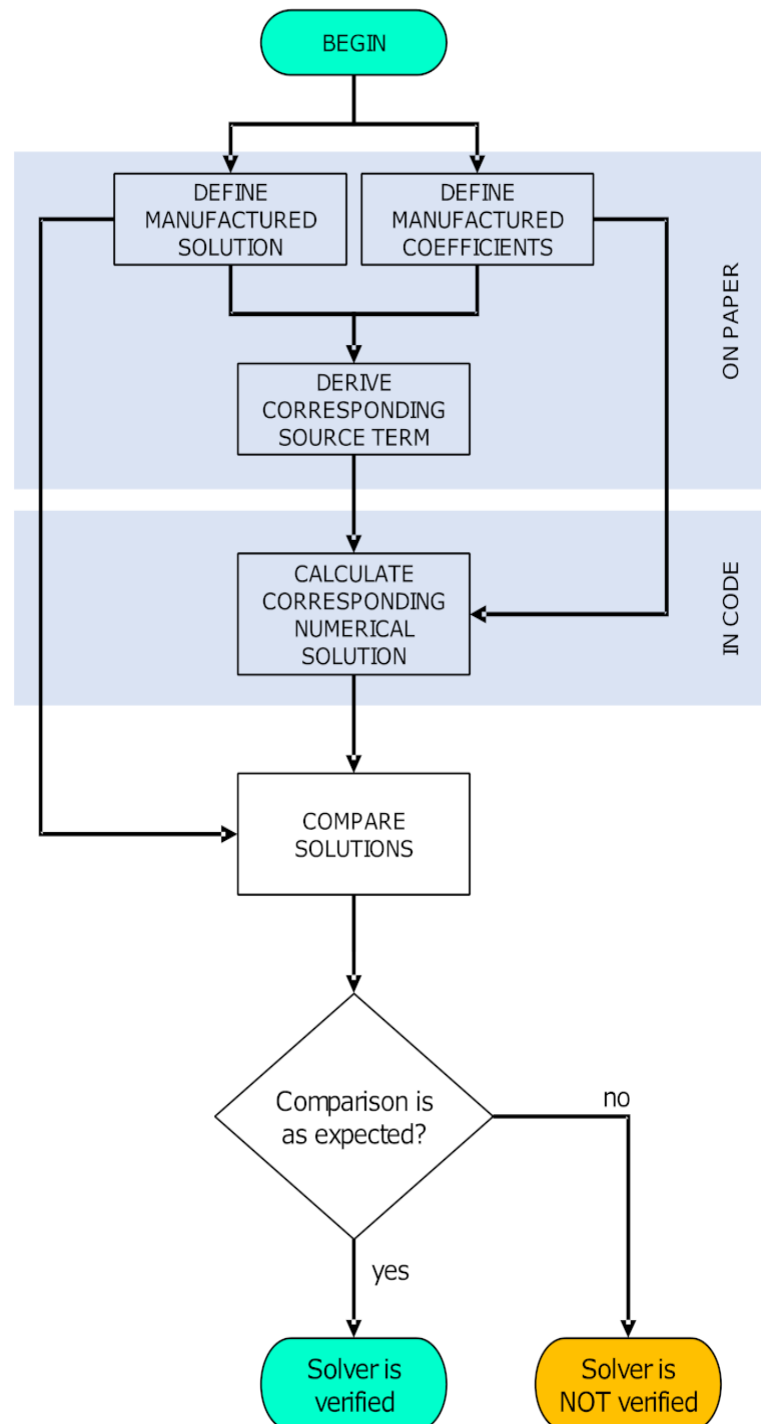
Figure A.2: Conceptual map of the method of manufactured solution verification strategy [279]. This verification strategy is applied for every solver in SCIANTIX.

call[26]. In order to ensure this limited computational time, all the models' differential equations are solved with an operator split approach[27], i.e., sequenced based on their characteristic time constants and with coefficients evaluated at the beginning of time step.

Physics-based models

In this Section, I briefly describe the inert gas behavior models for UO_2 available in the version 1.0 of SCIANTIX. More detailed information about each model can be found in dedicated publications[28] [25, 26, 34, 72, 141, 186].

Intra-granular fission gas behavior

The description of intra-granular fission gas behavior is typically the first and fundamental part of models for the prediction of fission gas release and swelling in nuclear fuel performance codes. The model currently available in SCIANTIX (described in detail in [26] and outlined both in Chapter 2 and 3) considers the fundamental processes of single gas atom diffusion, i.e., gas bubble nucleation, re-solution, and gas atom trapping at bubbles. The model is derived from a cluster dynamic formulation yet consisting of only three differential equations in its final form. It can hence be efficiently applied in engineering fuel performance codes while retaining a physical basis. The model equations are similar to state-of-the-art models currently used in fuel performance codes (see [56] for a complete review).

As for spatial problem, the intra-granular diffusion is treated with the classical Booth's approach [199], i.e., assuming a spherical grain of radius a. According to the approximation originally proposed by Speight [200], I solve for the total intra-granular gas concentration, given by the sum of the single-atom gas concentration c_1 and the

---

[26] It is worth noting that the stand-alone use of SCIANTIX requires in general a longer computational time compared to the use as a module in fuel performance codes, the difference being related to the file handling operations required to produce the output of SCIANTIX.

[27] The use of operator split approach is clearly a numerical approximation, required to ensure the computational performance of SCIANTIX. Depending on the simulation to be performed, this numerical approach may not be adequate, since it greatly simplifies the treatment of non-linearities (both in the state variables and in the coefficients). For this reason, an internal convergence loop is being developed and will be available in future versions as an alternative option.

[28] It is worth noting that all the models included in the open source version of SCIANTIX are already published. SCIANTIX is used for model development and testing on several other topics, from inert gas behavior to actinide evolution, which are not yet available open source and therefore not detailed in this work.

Table A.2: Options available for the fission gas diffusivity, D m^2 s^{-1}.

Option	Correlation	Reference
0	$D = 0.0$	–
1	$D = D(T, \dot{F}) = D_1 + D_2 + D_3$	[106]
	$D_1 = 7.6 \cdot 10^{-10} \exp(-4.86 \cdot 10^{-19}/k_B T)$	
	$D_2 = 5.64 \cdot 10^{-25}\sqrt{\dot{F}}\exp(-1.91 \cdot 10^{-19}/k_B T)$	
	$D_3 = 2 \cdot 10^{-40} \cdot \dot{F}$	
2	$D = D(T) = 5 \cdot 10^{-8} \exp(-40,262/T)$	[54, 277]

gas concentration trapped in intra-granular bubbles m [29]

$$\begin{cases} \dfrac{\partial(c_1 + m)}{\partial t} = \dfrac{\alpha}{\alpha + \beta}D\nabla^2(c_1 + m) + y\dot{F} \\ \dfrac{\mathrm{d}N_ig}{\mathrm{d}t} = \nu - \alpha N \end{cases} \tag{A.1}$$

where D is the single-atom diffusion coefficient (Table A.2), α is the re-solution rate (Table A.4), β is the trapping rate (Table A.5), y is the fission yield of fission gas, $\dot{F}$ is the fission rate, and t is time. The term $\alpha/\alpha + \beta\ D$ is referred to as the effective diffusion coefficient, accounting for the fraction of time single atoms are available for diffusion towards grain boundaries (i.e., not trapped in intra-granular bubbles).

As for the evolution of intra-granular bubble concentration N, the current model assumes that bubbles are formed at a nucleation rate ν (Table A.3) and destroyed by irradiation induced re-solution[30]. The intra-granular bubble radius is then calculated assuming m/N atoms in each bubble, i.e.,

$$R = \left(B_{ig}\frac{m}{N}\right)^{1/3} \tag{A.2}$$

---

[29] The approximation proposed by Speight assumes that the trapping and re-solution of gas to and from intra-granular bubbles is faster than the diffusion towards the grain boundaries, therefore considering the evolution of the gas concentration in intra-granular bubbles as quasi-static. The limitations of this approach have been demonstrated theoretically by Veshchunov and Tarasov [23] through an alternative derivation of Eq. A.1, and also shown non-adequate for particular fast transient conditions (timescales in the order of milliseconds, through numerical experiments [201]). Nevertheless, the approximation by Speight is practically effective in operational and relatively slow transient conditions (timescale in the order of seconds), and therefore still applied in fuel performance codes. For this reason, it is currently considered the default approach in SCIANTIX. Overcoming this quasi-static approximation is one of the envisaged developments of SCIANTIX.

[30] The intra-granular model currently does not consider the mobility of intra-granular bubbles in isothermal conditions. This mechanism has been observed experimentally at high temperatures (above 1800°C) [76] and confirmed by recent analysis [100] but the mechanism is still under investigation [281]. Straightforward extension of the model including this mechanism can be found in [127].

Table A.3: Options available for the intra-granular bubble nucleation rate ν (bub m^{-3} s^{-1}).

Option	Correlation	Reference
0	$\nu = 4.0 \cdot 10^{20}$	–
1	$\nu = 2 \cdot 25 \cdot \dot{F}$	[30, 56, 65]

Table A.4: Options available for the intra-granular re-solution rate, α (s^{-1}).

Option	Correlation	Reference
0	$\alpha = 1.0 \cdot 10^{-4}$	–
1	$\alpha = 2\pi\mu_{ff}\left(R + R_{ff}\right)^2 \cdot \dot{F}$	[102]
2	$\alpha = 3 \cdot 10^{-23} \cdot \dot{F}$	[29]

Table A.5: Options available for the intra-granular trapping rate β (s^{-1}).

Option	Correlation	Reference
0	$\beta = 1.0 \cdot 10^{-4}$	–
1	$\beta = 4\pi D(R + R_{sg})N$	[105]

where $B_{ig} = 4.09 \cdot 10^{-29}$ m^3 is the gas atomic volume in the lattice[31]. The intra-granular component of the gaseous swelling is derived as

$$\left(\frac{\Delta V}{V}\right)_{ig} = \frac{4}{3}\pi N R^3 \tag{A.3}$$

Inter-granular inert gas behavior

The inter-granular bubble evolution model adopted in SCIANTIX is the one proposed by Pastore et al. [34, 72], with the extension accounting for micro-cracking of grain boundaries in transient conditions [25]. This model is the default option in the BISON fuel performance code and available in TRANSURANUS as well. Remarkably, the model has been validated both as stand-alone against a set of

---

[31] This value, which is the volume of a Schottky trio (a neutral defect complex made by one uranium vacancy plus two oxygen vacancies) in the uranium dioxide lattice, is consistent with the measured (atomic) densities of intra-granular fission gas bubbles reported in [1, 80, 217]. It must be underlined that some atomic volumes occupied by Xe and Kr in intra-granular bubbles reported in the open literature (e.g., [101] based on Ronchi equation of state [219]) are derived considering equilibrium bubbles, yielding atomic volumes slightly higher than the ones reported in [1, 80, 217].

separate effects experiments [50] in terms of inter-granular bubble swellings, and within TRANSURANUS against integral irradiation experiments in terms of integral fission gas release [25, 34]. In the light of its mechanistic nature, the model formulation is the same as the one accounting for the development of grain boundary bubbles in U_3Si_2, presented in Chapter 4. I chose to briefly report the main features also here below for the sake of completeness.

The variation rate of gas atom concentration into inter-granular bubbles q is given by

$$\frac{\partial q}{\partial t} = - \left[\frac{3}{r_{gr}} \frac{\alpha}{\alpha + \beta} D \frac{\partial(c_1 + m)}{\partial r} \right]_{r=a} - R \tag{A.4}$$

where r_{gr} (m) is the grain size, r is the radial coordinate of the spherical laplacian (Eq. A.1). The source term for q is the flux of single atoms diffusing from inside the fuel grain, whereas the release term R is modeled accounting for different phenomena:

1. Gas atoms arriving at the grain boundaries are collected in inter-granular bubbles, which are assumed to be one-off nucleated (e.g., [30]) on grain faces. No single atoms are assumed to exist at grain boundaries, since it is assumed that the trapping of single gas atoms is faster than the other processes[32] and re-solution of gas from inter-granular bubbles is neglected. Moreover, grain-edges bubbles are not modeled.

2. Inter-granular bubbles, assumed of lenticular shape with circular projection on grain faces, are pressurized by gas atoms and grow by diffusion-controlled – with vacancy diffusivity at the grain boundaries D_v – vacancy absorption towards an equilibrium pressure [114] (Table A.6).

3. The bubbles interconnect because of their growth. The inter-granular bubble concentration N_{gb} (bub m^{-2}) on grain faces decreases as their projected area on the grain face A_{gf} (m^2 bub^{-1}) grows following $dN_{gf}/dA_{gf} = -2N_{gf}^2$.

4. The net result of inter-granular bubble growth and interconnection is the increase of the grain-face fractional coverage $F_{gf} = N_{gf}A_{gf}$ (/). When the fractional coverage reaches a saturation value $F_{gf} = F_{gf,sat} = 0.5$, it is assumed that a percolated path along the grain faces is formed, allowing for the release of gas from the grain boundaries.

---

[32] These modeling assumption (one-off nucleation and instantaneous trapping) do not allow for the description of phenomena such as circulation, in which single gas atoms undergo to a re-solution from inter-granular bubbles back into the matrix, hence constituting an additional source term for the flux of gas atoms possibly transported to the grain edges. This phenomenon, which is considered e.g. in the MFPR code [31], requires the description of irradiation-induced re-solution of gas atom from inter-granular bubbles (e.g., [188]), plus the modeling of grain-edges gas bubbles. In the model employed in SCIANTIX, based on Pastore et al. [34], these two features are not included, thus gas circulation at grain boundaries cannot be modeled.

Table A.6: Options available for the inter-granular vacancy diffusion coefficient D_v (m^2 s^{-1}).

Option	Correlation	Reference
0	$D_v = 1.0 \cdot 10^{-30}$	–
1	$D_v = 6.9 \cdot 10^{-4} \exp(-3.88 \cdot 10^4/T)$	[287]
2	$D_v = \left(\dfrac{3}{5}\right) 8.86 \cdot 10^{-6} \exp(-4.17 \cdot 10^4/T)$	[72]

5. The swelling rate decreases as the percolation of grain boundaries occurs, since the gas atoms diffusing from the interior of the grains are not entirely stored in the grain-boundary bubbles once percolation occurred.

The inter-granular swelling is mechanistically described according to

$$\left(\frac{\Delta V}{V}\right)_{gf} = \frac{3}{r_{gr}} \frac{4\pi}{3} N_{gf} R_{gf}^3 \tag{A.5}$$

where R_{gf} (m bub^{-1}) is the radius of inter-granular bubbles and $3/r_{gr}$ is the surface-to-volume ratio of fuel grains.

On top of this model describing the evolution of grain-face bubbles fed by intra-granular diffusion and allowing for fission gas release, we consider a semi-empirical description of a mechanism of grain-boundary micro-cracking [7, 282–285], based on [25]. By introducing the fraction of non-cracked grain-faces f_{gf}, one can write its influence on the fractional coverage F_{gf} and the saturation fractional coverage of grain boundaries $F_{gf,sat}$ as

$$\begin{cases} \dfrac{\mathrm{d}F_{gf}}{\mathrm{d}t} = \dfrac{\partial F_{gf}}{\partial q} \dfrac{\mathrm{d}q}{\mathrm{d}t} + F_{gf}\left(\dfrac{\mathrm{d}f_{gf}}{\mathrm{d}t}\right) \\[4mm] \dfrac{\mathrm{d}F_{gf,sat}}{\mathrm{d}t} = F_{gf,sat}\left(\dfrac{\mathrm{d}f_{gf}}{\mathrm{d}t}\right) \end{cases} \tag{A.6}$$

where the evolution of the fractional coverage is described as the super-position of the inflow of gas atoms (and the consequent grain-boundary bubble evolution) and the micro-cracking of grain boundaries. The evolution of f_{gf} is described by an empirical micro-cracking parameter, which is a function of temperature and burnup, accounting for micro-cracking during heating and cooling transients [282–285] and healing of micro-cracks with burnup [286].

Micro-structure evolution

The grain growth process is strictly related to fission gas behavior [1, 2] and therefore its treatment is required in SCIANTIX. Grain growth has two major

consequences: (1) it affects the diffusion rate towards the grain boundaries, D/r_{gr}^2, and (2) while moving during the grain growth process, grain boundaries effectively sweep the fuel, collecting gas and gas bubble as a net [135, 288, 289]. The model currently available in SCIANTIX is based on the work of [290, 291], drawn on the formulation of Hillert [292] and accounting for the so-called Zener pinning effect [293], reading

$$\frac{\mathrm{d}r_{gr}}{\mathrm{d}t} = 4M \left(\frac{1}{r_{gr}} - \frac{g\,(bu)}{r_{gr,m}} \right) \tag{A.7}$$

where $M = 1.46 \cdot 10^{-10} \exp(-32,114.5/T)$ [33] is the grain-boundary mobility, $g(bu) = 1 + 0.002bu$ is an empirical function of burnup bu, and $r_{gr,m} = 2.23 \cdot 10^{-3} \exp(-7,620/T)$ is the limiting grain size for a given temperature T.

Besides the normal grain growth process, relevant for low burnups (e.g., [293, 298, 301]), also the formation of high burnup structure involves a recrystallization of grains, *de facto* changing the grain size [51]. The description of the formation and evolution of high burnup structure is herein described as just affecting the (average) grain size. The model describing HBS formation and depletion currently available in SCIANTIX is based on the concept of effective burnup, i.e., the burnup integrated below a certain temperature threshold (e.g., [32] or see Chapter 3), as representative of the accumulation of radiation damage triggering recrystallization. Namely, the evolution of the "average" grain size[34] is described by

$$\frac{\mathrm{d}r_{gr}}{\mathrm{d}bu_{eff}} = -\frac{1}{\tau} \left(r_{gr} - r_{gr,\infty} \right) \tag{A.8}$$

where, bu_{eff} is the effective burnup, $\tau = 5$ GWd t_{UO2}^{-1} is the characteristic burnup governing the high burnup structure formation rate, and $a_\infty = 150$ nm is the grain radius of recrystallized grains in the high burnup structure of UO_2 (e.g., [140, 159]).

Showcase of results

Stand-alone validation of the physics-based models available in SCIANTIX has been performed for each of the described models and is extensively reported in

---

[33] The mobility of grain boundaries herein reported is based on the experimental data of [293]. It is possible to apply the model for grain growth available in SCIANTIX with other correlations for grain-boundary mobility derived from lower-length scale analysis [294–297] or from another experimental dataset (e.g., [298, 299]). The grain-boundary mobility may be defined accordingly to the exponent of a on the right-hand side of Eq. A.7, (1 in the current formulation), but different exponents may be found in the literature (e.g., [292, 300]).

[34] The formation of high burnup structure may be depicted as a phase transition, with one phase being the unrestructured fuel, and the other phase being the recrystallized fuel (e.g., see the modeling approach in [32, 192]). The herein proposed description averages out these two phases by defining an average phase featured by a representative grain size, evolving from the unrestructured value to the recrystallized value. The model presented in Chapter 3 overcomes this simplification and introduces the description of HBS porosity. It will be included in the next version of the code.

previous publications [26, 34, 186]. Together with the comparison with experimental data, the referenced publications include also comparison between the results of the models currently available in SCIANTIX and those of several state-of-the-art models available in the open literature. Moreover, the validation strategy applied for SCIANTIX involves the comparison between integral irradiation experiments results and the simulation results of fuel performance codes including SCIANTIX as fission gas behavior module. Also, these comparisons have been published in dedicated publications (e.g., [25]). For the sake of completeness, I report a summary of the validation database of SCIANTIX, comparing the calculations to experimental results in terms of gaseous swelling. These results are complemented by a detailed showcase of selected SCIANTIX simulations (still compared with experimental results) in relevant cases (both constant and transient conditions). Finally, I apply the SCIANTIX code to the simulation of an irradiation history typical of a RIA scenario, to showcase the capabilities of the code in accident conditions.

Gaseous swelling results from the overall SCIANTIX validation database

Stand-alone validation of SCIANTIX against experimental data in terms of gaseous swelling is presented in Figure A.3. In this Figure, we compare the predictions on both intra-granular swelling (i.e., swelling due to intra-granular bubbles as defined by Eq. A.3) and inter-granular swelling (i.e., swelling due to grain boundary bubbles, as defined by Eq. A.5).

The experimental database by Baker [65] includes irradiation at constant temperatures (from 1273 K to 2073 K) and low burn-up (6.5 GWd/t$_{UO2}$) of standard uranium dioxide fuels in the UKAEA's Winfirth SGHWR. The results are in line with those ones shown in a previous publication of the intra-granular model employed in SCIANTIX [26], and demonstrate an acceptable deviation from the experimental data in terms of gaseous swelling. For a more thorough analysis of this experimental database, I refer the reader to aforementioned publication.

Comparison of the predicted gaseous swelling due to inter-granular bubbles to experimental data is also included in Figure A.3. The experimental cases are taken from the database by White and co-workers [50], which were considered already in this thesis work in Chapter 2. The database consists in measurements performed on uranium dioxide Advanced Gas Reactor samples of fuel rods irradiated up to burnup between 9 and 21 GWd/t$_{UO2}$ in the Halden reactor. After the base irradiation, rods were subjected to power ramp or power cycle histories. The comparison shows a satisfactory agreement between calculated and measured data yet demonstrating an overestimation of the low swelling data. Indeed, the results obtained through SCIANTIX are in-line with a previous publication entailing the same model for inter-granular bubble evolution and experimental database [34].

Constant conditions

To showcase detailed SCIANTIX results in constant conditions, I selected the simulation of one of the experimental fuel samples by Baker [65], and summarized in Section 5. The sample has been analyzed using transmission electron microscopy to measure intra-granular bubble concentration and intra-granular bubble radius.

The simulation in SCIANTIX is set up with an irradiation history of 5,500 hours with a constant fission rate of $1 \cdot 10^{19}$ fiss m^{-3} s^{-1} (resulting in $\approx 2 \cdot 10^{16}$ fiss m^{-3} $\approx$ 6.5 GWd/t$_{UO2}$), at a constant temperature of 1300 K and with no hydrostatic stress. The default model parameters required in Eqs. A.1–A.3 are used (i.e., option 1 in Tables A.2–A.6), namely Turnbull's diffusivity, heterogeneous nucleation, Turnbull's heterogeneous re-solution rate, and diffusional trapping.

Figure A.4 reports the evolution of intra-granular bubble concentration and of intra-granular bubble radius as a function of burnup as simulated by SCIANTIX, compared with the experimental results available at end of irradiation. First, the agreement between simulated and experimental results is satisfactory. The agreement
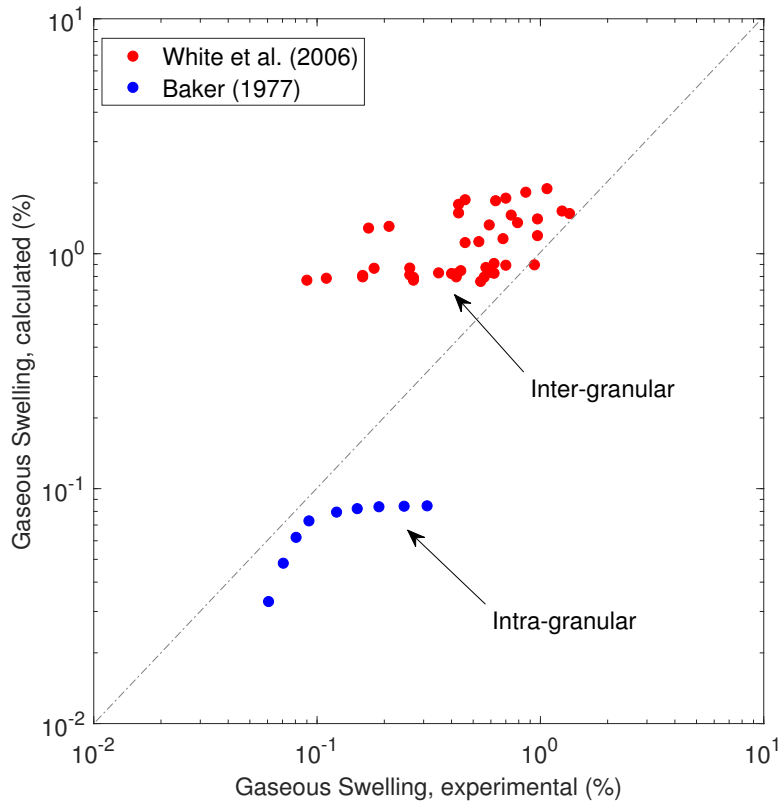
Figure A.3: Comparison of calculated intra- and inter-granular gaseous swelling by SCIANTIX to experimental data by Baker [65] (swelling due to intra-granular bubbles, blue markers) and by White and co-workers [50] (swelling due to inter-granular bubbles, red markers).
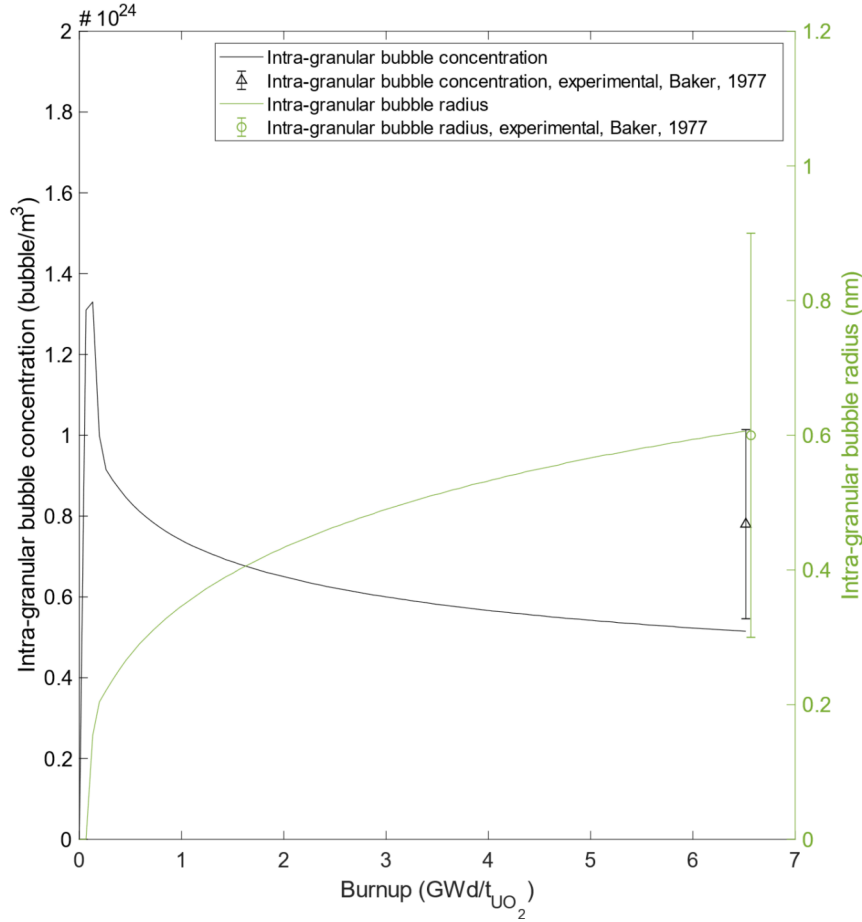
Figure A.4: Evolution of intra-granular bubble concentration and intra-granular bubble radius as a function of burnup in constant conditions as predicted by SCIANTIX, compared with the experimental results by Baker [65].

with experiments is particularly good for the intra-granular bubble radius, which is dominant compared to the intra-granular bubble concentration in determining the intra-granular swelling (third power in Eq. A.3). Besides the values at the end of irradiation, it is interesting to discuss the evolution of the variables along burnup. The intra-granular bubble concentration evolves according to Eq. A.1. Due to the selection of a heterogeneous nucleation rate and a heterogeneous re-solution rate as model parameters, after an initial increase due to nucleation, the evolution of the intra-granular bubble concentration is asymptotically determined by the ratio of these two parameters, i.e., when $dN/dt \to 0$, then $N \to \nu/\alpha = \eta/\left[2\pi\mu_{ff}\left(R+R_{ff}\right)^2\right]$. The only variable in the right-hand side is the intra-granular bubble radius R, therefore as the intra-granular bubble radius increases steadily as a result of trapping, the bubble concentration decreases with burnup.

As for the growth of the radius of intra-granular bubbles, it is governed by Eq. A.2, in particular by the ratio between the intra-granular gas concentration trapped in bubbles and the bubble concentration, i.e., m/N. The intra-granular gas concentration in bubbles is depicted in Fig. A.5, together with the evolution
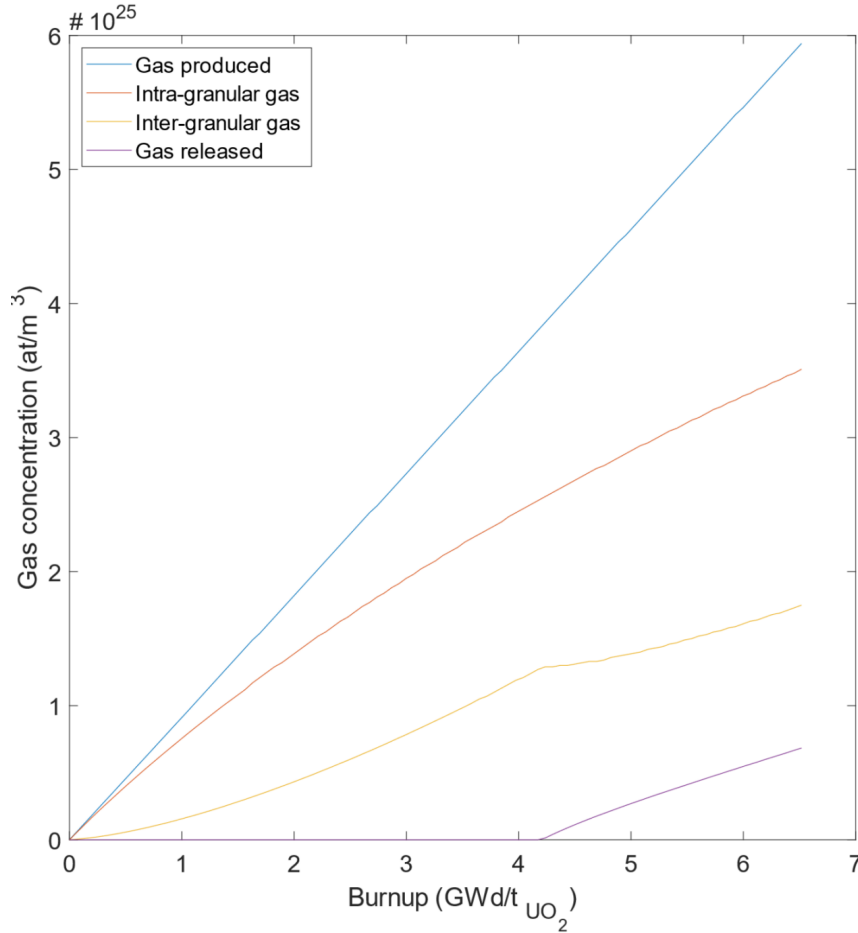
Figure A.5: Evolution of gas concentrations a function of burnup in an irradiation history [65] with constant conditions as predicted by SCIANTIX.

of the other gas concentrations. The gas evolution is governed by Eqs. A.1, A.4. The gas produced increases linearly as $y\dot{F}$. A fraction of it, the intra-granular gas concentration, $c_1 + m$, remains inside the grain after the diffusion process occurs. The gas that reaches the grain boundary, q, is eventually released when the saturation of grain boundaries is reached (see the change of slope in the curve in Fig. A.5). The release process occurring in this irradiation history is purely diffusion-based, since no temperature variations. According to the model described in Section 5, the gas release occurs only after the saturation of grain boundary is reached (in line with the change of slope in the inter-granular gas concentration).

The behavior of gas at the grain boundaries is clear from Fig. A.6. The inter-granular bubble concentration N_{gf} decreases from the initial value $4 \cdot 10^{13}$ bub m^{-3} (model parameter representing a one-off nucleation [30, 34]) as the bubble size A_{gf} increases due to the inflow of gas from inside the grains and the absorption of vacancies due to bubble over pressurization. As bubble growth and interconnection proceeds, the fractional coverage $F_{gf} = N_{gf}A_{gf}$ increases steadily, up to the saturation value $F_{gf} = F_{gf,sat} = 0.5$. The instant at which the saturation is reached corresponds to onset of fission gas release in Fig. A.5.
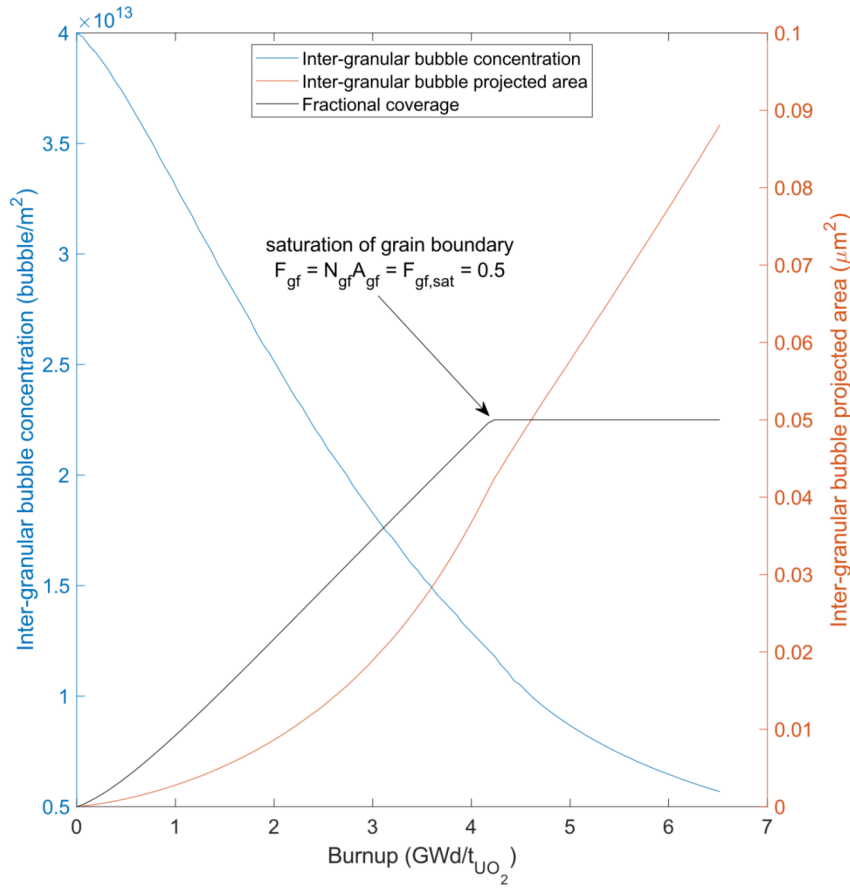
Figure A.6: Evolution of inter-granular bubble concentration, projected area, and fractional coverage as a function of burnup in an irradiation history [65] with constant conditions as predicted by SCIANTIX.

Transient conditions

To showcase the application of SCIANTIX in transient conditions, I selected an irradiation case among those analyzed by White and co-workers [50] and presented in Section 5. This case study allows discussing in more detail the behavior of the grain-boundary model. The considered fuel sample (referred to as 4000C–A), after a base irradiation at low temperature (lower than 900°C) up to a local burnup of 17.5 GWd/t_{UO2} (corresponding to an irradiation of 35,600 hours at a constant fission rate of $4.15 \cdot 10^{18}$ fiss m^{-3} s^{-1} and a constant hydrostatic stress of -0.21 MPa, based on ENIGMA [136] calculations [50]), has been subject to a ramp test characterized by (1) a conditioning step of 288 hours at 884°C, $4.15 \cdot 10^{18}$ fiss m^{-3} s^{-1}, and -0.21 MPa, followed by (2) a ramp up of 1.52 minutes up to (3) a holding of 30 minutes at 1775°C, $1.08 \cdot 10^{19}$ fiss m^{-3} s^{-1}, and -14.8 MPa, followed by (4) a ramp down of 100 seconds down to (5) a final holding of 99 minutes at 884°C, $4.15 \cdot 10^{18}$ fiss m^{-3} s^{-1}, and -0.21 MPa, and (6) a fast SCRAM (Fig. A.7).

Figure A.8 reports the evolution of gas concentration as a function of temperature, as predicted by SCIANTIX. In this representation, the base irradiation and the
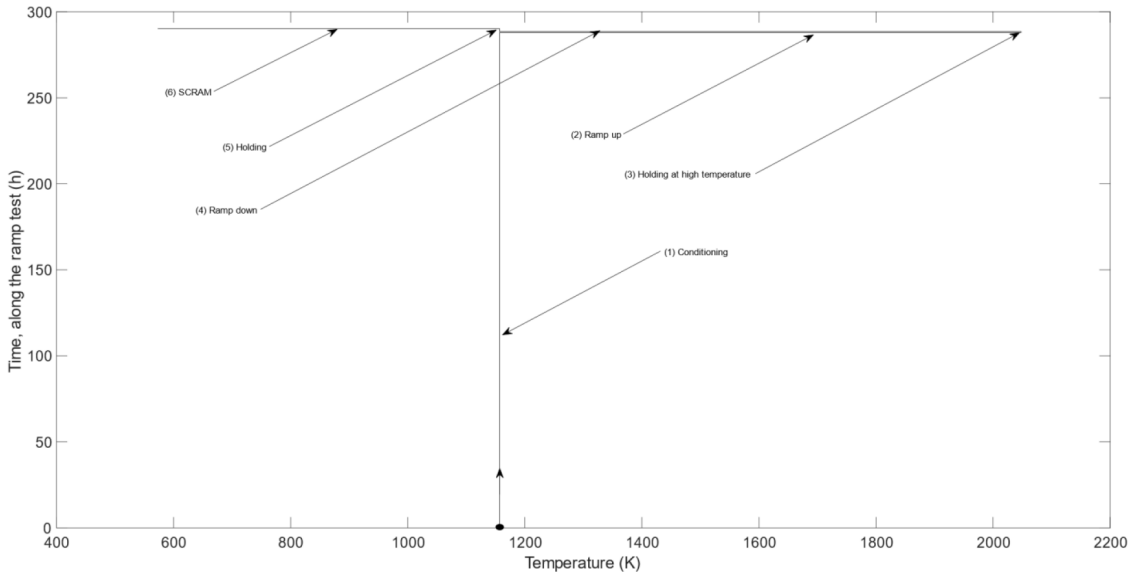
Figure A.7: Temperature history for the sample 4000C–A from White et al. [50]. The (unusual) choice of plotting time as a function of temperature has the purpose of easing the reading of Figs. A.8 and A.9. Temperature is a more natural variable for this transient, and it allows a clearer description of the model behavior compared to time (due to the brevity of the ramp compared to the conditioning period).

conditioning step are vertical lines at 1157 K, while the holding on the of the ramp is the vertical line at 2048 K. Each line can be followed by the Beginning of the Ramp Test (BRT) towards the End of the Ramp Test (ERT). Moving right along a line corresponds to a temperature increase, moving vertically to a step at constant temperature, and moving left to a temperature decrease.

The first observation from Fig. A.8 is that the produced gas is practically constant. Second, during this ramp test the intra-granular gas concentration (almost) never grows, besides the temperature and consequently the diffusivity increases. This is caused by the competition of intra-granular bubble trapping and diffusion towards the grain boundaries. It can be seen from Fig. 8 that the gas is transferred from intra-granular solution to intra-granular bubbles during the heating and the holding, and back from intra-granular bubbles to the solution during the cooling period, with a net trapping effect visible at ERT.

As for the gas at the grain boundaries, it is clear from Fig. A.8 that it is released during the heating, the holding at high temperature, and the cool down as well. During the heat up, the release is mainly caused by the micro-cracking of grain boundaries and partially by the diffusional release following grain-boundary bubble coalescence (as discussed, no additional gas arrives at the grain boundary during the ramp test, but the increase in temperature causes an increase in bubble pressure, triggering bubble growth by vacancy absorption).

The contributions to fission gas release arising from either micro-cracking of grain boundaries or diffusional release can be isolated by looking at the evolution of the grain-boundary coverage as a function of temperature (Fig. A.9a). From the base
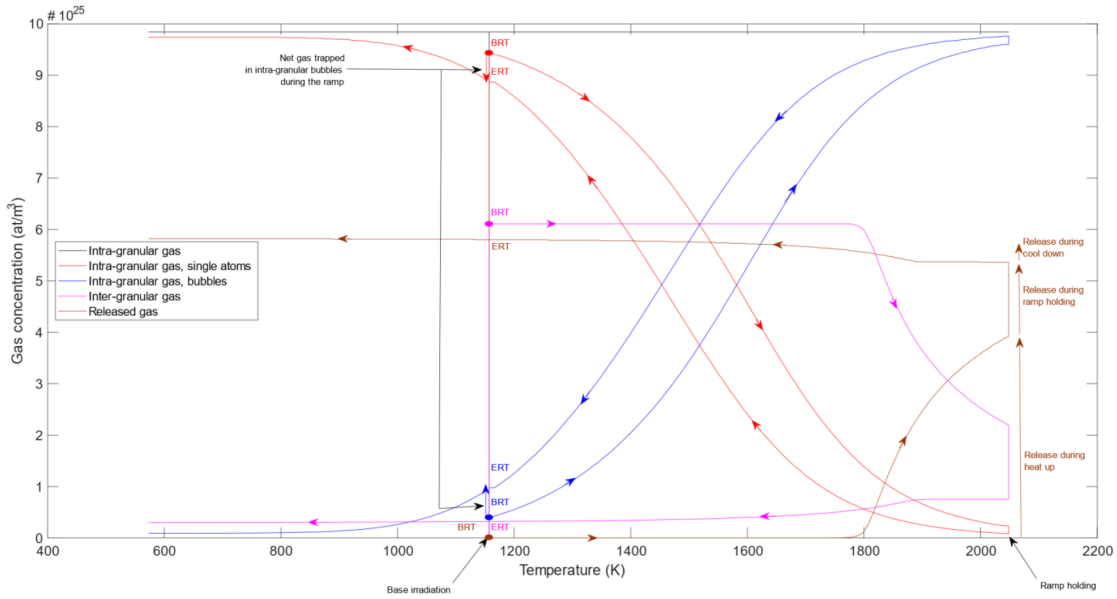
Figure A.8: Evolution of the gas concentrations as a function of temperature, simulated by SCIANTIX for the sample 4000C–A from White et al. [50]. From the beginning of the ramp test (BRT), moving right corresponds to a heating transient, vertical lines correspond to temperature holdings, and moving left correspond to a cooling transient. The end of the ramp is marked by ERT.
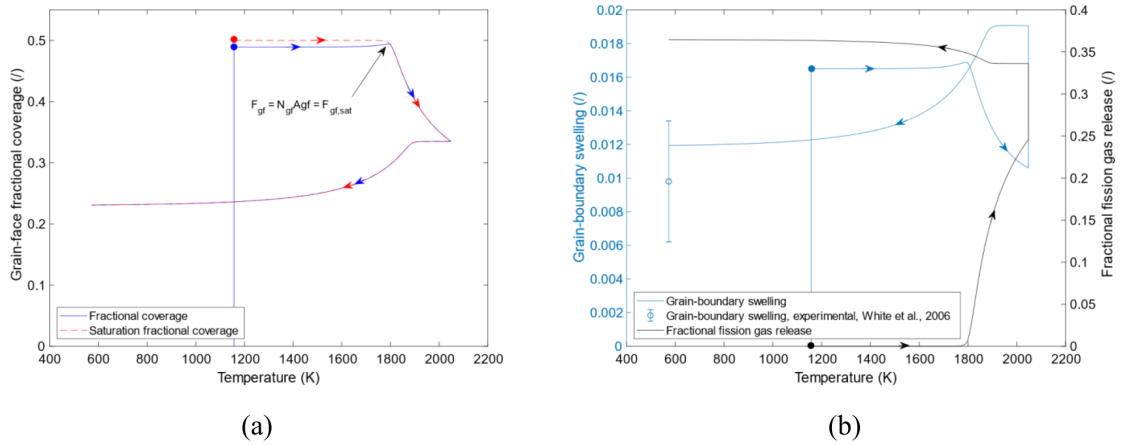
Figure A.9: Evolution of (a) the grain-face fractional coverage, saturation fractional coverage (dashed line), and (b) grain-boundary swelling and fractional fission gas release as a function of temperature, simulated by SCIANTIX for the sample 4000C–A by White et al. [50]. Base irradiation corresponds to the vertical line at 1157 K, moving right corresponds to a heating transient, the holding on top of the power/temperature ramp corresponds to the vertical line at 2048 K, and moving left corresponds to the cooling transient, down to 573 K. The experimental measurement of grain-swelling is reported for comparison sake.

irradiation of 1157 K, the grain-face fractional coverage slightly increases during the first moments of the heat up step (up to $\approx$ 1800 K), reaching the saturation value and therefore triggering diffusional release. Above 1800 K it then steadily decreases due to the micro-cracking of grain faces during temperature transients and remains constant (at the saturation value) during the holding at 2048 K. Figure A.9b depicts the evolution of grain-boundary swelling and of fractional fission gas release as a function of temperature, which are directly related to the evolution of fractional coverage, the main difference being the increase of grain-boundary swelling during the high temperature holding because of vacancy absorption. It is evident that the onset of fission gas release as the fractional coverage reaches the saturation value. Lastly, Fig. A.9b reports the satisfactory agreement of the grain-boundary swelling predicted by SCIANTIX with the experimentally measured value.

Accident conditions

As a last showcasing of SCIANTIX capabilities, we present the simulation of a representative RIA transient scenario. It is clear that the purpose of this Section is not to demonstrate the capability of SCIANTIX of performing a safety analysis, which would be impossible with a 0D stand-alone code, but only to provide an example of SCIANTIX performance during a very fast (accidental) transient.

As an explicative RIA case we select the CABRI REP-Na5 power pulse experiment [171]. This experiment involved a Gaussian-type power pulse of 8.8 milliseconds full width at half maximum injecting 451 $\mathrm{J\,g^{-1}}$ in a UO_2–Zr-4 rodlet previously irradiated to 64 GWd/t$_{\mathrm{HM}}$. The analysis herein reported considers a point within the fuel pellet close to the pellet periphery. The evolution of the radial temperature profile during the transient test was derived in [171] by SCANAIR-3.2 calculations. The input conditions for the SCIANTIX simulation[35], i.e., temperature and fission rate evolution as a function of time – reported in Figure A.10, are directly extracted from the results presented in [171].

Figure A.11 reports the fission gas release evolution as a function of temperature as calculated by SCIANTIX. The release during the base irradiation is negligible compared to that obtained during the transient ($\approx$ 2%). The release of fission gas during this transient is ascribed by the model to the micro-cracking of grain boundaries, and thus is predicted to occur during both the heat up and the cool down. The measured integral fission gas release for the CABRI REP-Na5 test transient was of 15.1% [171]. Besides this experimental result not being directly comparable with the 0D local result obtained with SCIANTIX, it is in line with integral fuel performance calculations performed on the same RIA transient test applying a similar grain-boundary micro-cracking model [302].

As declared, the purpose of this Section is purely to demonstrate the suitability of SCIANTIX in simulating transients in the scale of milliseconds: several model

---

[35] A base irradiation in constant conditions (900 K, $1 \cdot 10^{19}$ fiss $\mathrm{m^{-3}\,s^{-1}}$) up to the burnup prior to the transient test has been postulated.
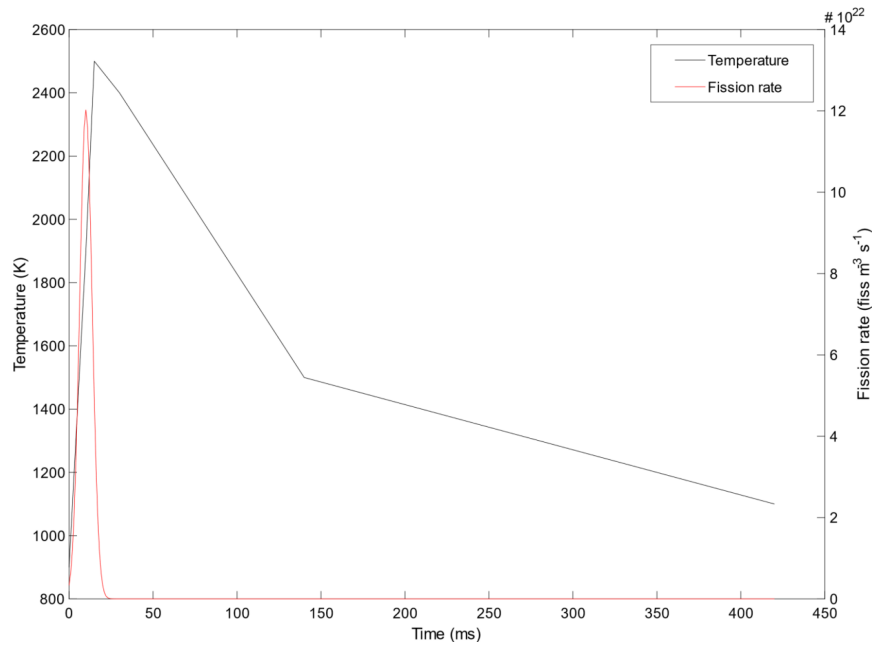
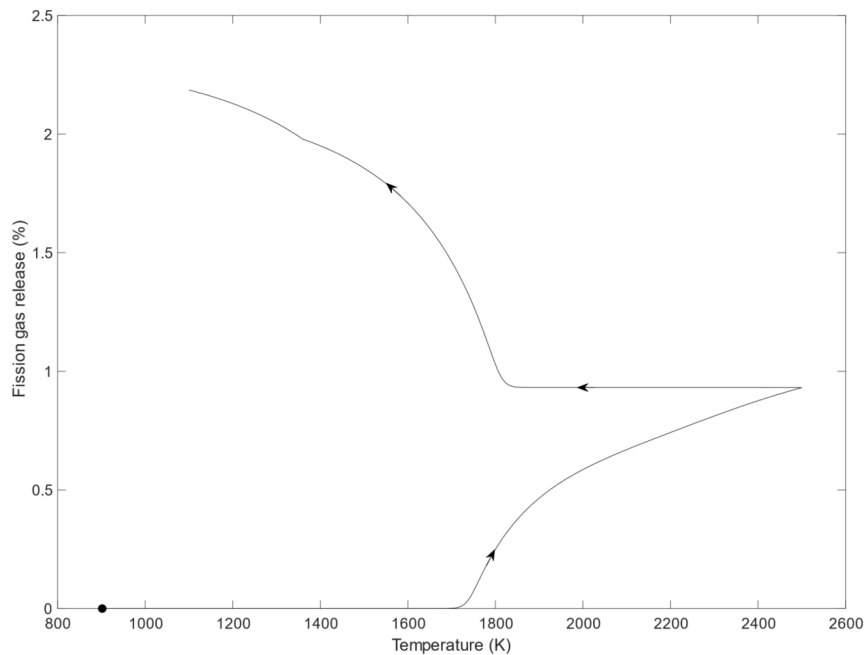Figure A.10: Temperature and power histories of the CABRI REP Na-5 power pulse test [171].

Figure A.11: Evolution of fission gas release as a function of temperature during the CABRI REP-Na5 transient test, as simulated by SCIANTIX.

developments are required for a proper description of fission gas behavior during RIA transient scenarios. Among the others, the treatment of non-equilibrium trapping and re-solution has been proved to play a role in this timescales [201].

Summary and future developments

In this Appendix I presented the models currently available in the open source version 1.0 of SCIANTIX (available at [276]), together with a summary of the validation and selected showcases of results compared with experimental data. Summarizing, the current version of SCIANTIX:

- Is designed to be used effectively as a fission gas behavior module included/coupled in/with fuel performance codes, and as stand-alone code as well.

- Includes a set of numerical solvers, each verified through the method of manufactured solutions, and has computational requirements in line with the needs of fuel performance codes.

- Includes a consistent set of models (independently published and validated) describing fission gas behavior in UO_2, providing an overall physic-based description of the phenomena, with semi-empirical approaches used essentially for model parameters.

In view of these characteristics, SCIANTIX is a candidate to effectively realize a multi-scale bridging in the description of fission gas behavior in oxide fuel, allowing for the transfer of knowledge from the lower-length scale up to the engineering-scale of fuel performance codes[36].

As conclusion, I summarize the ongoing model developments of SCIANTIX, which partly overlap with the activities carried out in the framework of this thesis and with the future perspectives elucidated in Chapter 5:

- A description of helium behavior, based on the current treatment of fission gas behavior but including additional terms, such as the solubility [99, 303–305]. This model is of relevance for the simulation of uranium-plutonium mixed oxide fuels and of storage conditions, where helium concentration becomes relevant.

- A description of actinide evolution with burnup, based on a reduced order model employing Bateman's equation with energy-averaged cross sections considered as functions of burnup and initial fuel composition [195, 306, 307]. This depletion capability implies the prediction of the helium production rate.

- A model describing intra-granular bubble coarsening, which is the object of the investigations shown in Chapter 2. This model will allow a more accurate description of intra-granular bubble swelling during transients.

---

[36]As an example, model parameters (like diffusivity of atoms and vacancies, re-solution and nucleation rate formulation) may be calculated by atomistic approaches, molecular dynamics, or other lower-length scale methods, as was shown in the Chapter 4 of this thesis. Then, one may plug the derived expression in the current models, as an additional option beside available correlations, without affecting the evolution equations constituting the models.

- A comprehensive model describing the HBS formation, intra-granular gas depletion, and porosity evolution, which was developed and presented in this thesis work in Chapter 3. This will remarkably overcome some semi-empirical approaches present in the current model.

- A reduced order model describing the diffusion of intra-granular gas in columnar grains, relevant for the simulation of MOX fuel in fast reactor conditions.

More long-term developments include the description of fission products formation and evolution, and the description of point defects evolution and interaction with fission gas. For all these model developments, the validation strategy based on comparison with separate effect experiments is going to be applied when possible.

As for the inclusion of SCIANTIX within fuel performance codes as a fission gas behavior module, the current status is that coupling has been demonstrated in TRANSURANUS [308] and will be subject of future publications, and is being pursued for GERMINAL code [309] in the frame of the INSPYRE Project [10].

REFERENCES

[1] D. R. Olander, Fundamental Aspects of Nuclear Reactor Fuel Elements, Technical Information Center, Office of Public Affairs Energy Research and Development Administration, 1976.

[2] J. Rest, M. Cooper, J. Spino, J. Turnbull, P. Van Uffelen, C. Walker, Fission gas release from UO_2 nuclear fuel: A review, Journal of Nuclear Materials 513 (2019) 310–345. doi:10.1016/J.JNUCMAT.2018.08.019.

[3] M. R. Tonks, D. Andersson, S. R. Phillpot, Y. Zhang, R. Williamson, C. R. Stanek, B. P. Uberuaga, S. L. Hayes, Mechanistic materials modeling for nuclear fuel performance, Annals of Nuclear Energy 105 (2017) 11–24. doi:10.1016/J.ANUCENE.2017.03.005.

[4] P. Van Uffelen, R. J. M. Konings, C. Vitanza, J. Tulenko, Analysis of reactor fuel rod behavior, in: D. G. Cacuci (Ed.), Handbook of Nuclear Engineering, Springer Science + Business Media, LLC, New York, 2010, Ch. 13, pp. 1519–1627.

[5] P. Van Uffelen, J. Hales, W. Li, G. Rossiter, R. Williamson, A review of fuel performance modelling, Journal of Nuclear Materials 516 (2019) 373–412. doi:10.1016/j.jnucmat.2018.12.037.

[6] K. Lassmann, The structure of fuel element codes, Nuclear Engineering and Design 57 (1) (1980) 17–39. doi:10.1016/0029-5493(80)90221-6.

[7] M. Tonks, D. Andersson, R. Devanathan, R. Dubourg, A. El-Azab, M. Freyss, F. Iglesias, K. Kulacsy, G. Pastore, S. R. Phillpot, M. Welland, Unit mechanisms of fission gas release: Current understanding and future needs, Journal of Nuclear Materials 504 (2018) 300–317.

[8] M. Bertolus, M. Freyss, B. Dorado, G. Martin, K. Hoang, S. Maillard, R. Skorek, P. Garcia, C. Valot, A. Chartier, L. Van Brutzel, P. Fossati, R. W. Grimes, D. C. Parfitt, C. L. Bishop, S. T. Murphy, M. J. D. Rushton, D. Staicu, E. Yakub, S. Nichenko, M. Krack, F. Devynck, R. Ngayam-Happy, K. Govers, C. S. Deo, R. K. Behera, Linking atomic and mesoscopic scales for the modelling of the transport properties of uranium dioxide under irradiation, Journal of Nuclear Materials 462 (2015) 475–495. doi:10.1016/j.jnucmat.2015.02.026.

[9] OECD - NEA, State-of-the-Art Report on Multi-scale Modelling of Nuclear Fuels, Tech. Rep. October (2015).

[10] M. Bertolus, INSPYRE: Investigations Supporting MOX Fuel Licensing in ESNII Prototype Reactors (2017).
URL http://www.eera-jpnm.eu/inspyre/

[11] B. D. Wirth, Fission Gas SciDAC 4: Simulation of Fission Gas in Uranium Oxide Nuclear Fuel (Oct 2018).
URL https://collab.cels.anl.gov/display/FissionGasSciDAC2

[12] K. Lassmann, TRANSURANUS: a fuel rod analysis code ready for use, Journal of Nuclear Materials 188 (1992) 295–302.

[13] A. Denis, R. Piotrkowski, Simulation of isothermal fission gas release, Journal of Nuclear Materials 229 (1996) 149–154. doi:10.1016/0022-3115(95)00203-0.

[14] G. Berna, C. Beyer, K. Davis, D. Lanning, A computer code for the calculation of steady-state, thermal-mechanical behavior of oxide fuel rods for high burnup, Tech. Rep. NUREG/CR-6534 (1997).

[15] J. P. Foster, S. Sidener, Westinghouse Improved Performance Analysis and Design Model (PAD 4.0) (2000).

[16] L. Bernard, J. Jacoud, P. Vesco, An efficient model for the analysis of fission gas release, Journal of Nuclear Materials 302 (2-3) (2002) 125–134. doi:10.1016/S0022-3115(02)00793-6.

[17] Á. Griger, J. Gadó, Models of the FUROM-1.3 Code, Tech. rep., AEKI-FRL-2007-719-1.3-01 (in Hungarian) (2007).

[18] A. R. Massih, K. Forsberg, Calculation of grain boundary gaseous swelling in UO_2, Journal of Nuclear Materials 377 (2) (2008) 406–408. doi:10.1016/j.jnucmat.2008.03.011.

[19] J. A. Turnbull, C. E. Beyer, Background and Derivation of ANS-5.4 Standard Fission Product Release Model, Tech. rep., United States Nuclear Regulatory Commission (2010).

[20] K. Mikityuk, A. Shestopalov, FRED fuel behaviour code: Main models and analysis of Halden IFA-503.2 tests, Nuclear Engineering and Design 241 (7) (2011) 2455–2461. doi:10.1016/J.NUCENGDES.2011.04.033.

[21] R. J. White, M. O. Tucker, A new fission gas release model, Journal of Nuclear Materials 118 (1) (1983) 1–38.

[22] J. Rest, An improved model for fission product behavior in nuclear fuel under normal and accident conditions, Journal of Nuclear Materials 120 (2-3) (1984) 195–212. doi:10.1016/0022-3115(84)90057-6.

[23] M. S. Veshchunov, V. I. Tarasov, Modelling of irradiated UO_2 fuel behaviour under transient conditions, Journal of Nuclear Materials 437 (1-3) (2013) 250–260. doi:10.1016/j.jnucmat.2013.02.011.

[24] G. Jomard, C. Struzik, A. Boulore, P. Mailhé, V. Auret, R. Largenton, CARACAS : An Industrial Model for the Description of Fission Gas Behavior in LWR-UO_2 Fuel, in: World Reactor Fuel Performance Meeting, no. 100154, Sendai, Japan, 2014, pp. 14–17.

[25] T. Barani, E. Bruschi, D. Pizzocri, G. Pastore, P. Van Uffelen, R. Williamson, L. Luzzi, Analysis of transient fission gas behaviour in oxide fuel using BISON and TRANSURANUS, Journal of Nuclear Materials 486. doi:10.1016/j.jnucmat.2016.10.051.

[26] D. Pizzocri, G. Pastore, T. Barani, A. Magni, L. Luzzi, P. Van Uffelen, S. A. Pitts, A. Alfonsi, J. D. Hales, A model describing intra-granular fission gas behaviour in oxide fuel for advanced engineering tools, Journal of Nuclear Materials 502 (2018) 323–330.

[27] J. Rest, A. Zawadski, FASTGRASS: A Mechanistic Model for the Prediction of Xe, I, Cs, Te, Ba, and Sr Release from Nuclear Fuel under Normal and Severe-Accident Conditions, Report NUREG/CR-5840, 1993.

[28] P. Van Uffelen, Contribution to the modelling of fission gas release in Light Water Reactor fuel, Ph.D. thesis, Université de Liège (2002).

[29] P. Lösönen, Modelling intragranular fission gas release in irradiation of sintered LWR UO$_2$ fuel, Journal of Nuclear Materials 304 (1) (2002) 29–49.

[30] R. J. White, The development of grain-face porosity in irradiated oxide fuel, Journal of Nuclear Materials 325 (1) (2004) 61–77. doi:10.1016/j.jnucmat.2003.10.008.

[31] M. S. Veshchunov, V. D. Ozrin, V. E. Shestak, V. I. Tarasov, R. Dubourg, G. Nicaise, Development of the mechanistic code MFPR for modelling fission-product release from irradiated UO$_2$ fuel, Nuclear Engineering and Design 236 (2) (2006) 179–200. doi:10.1016/j.nucengdes.2005.08.006.

[32] G. Khvostov, K. Mikityuk, M. A. Zimmermann, A model for fission gas release and gaseous swelling of the uranium dioxide fuel coupled with the FALCON code, Nuclear Engineering and Design 241 (8) (2011) 2983–3007.

[33] L. Noirot, MARGARET: A comprehensive code for the description of fission gas behavior, Nuclear Engineering and Design 241 (6) (2011) 2099–2118. doi:10.1016/j.nucengdes.2011.03.044.

[34] G. Pastore, L. Luzzi, V. Di Marcello, P. Van Uffelen, Physics-based modelling of fission gas swelling and release in UO$_2$ applied to integral fuel rod analysis, Nuclear Engineering and Design 256 (2013) 75–86. doi:10.1016/j.nucengdes.2012.12.002.

[35] J. Evans, Bubble diffusion to grain boundaries in UO$_2$ and metals during annealing: a new approach, Journal of Nuclear Materials 210 (1994) 21–29.

[36] M. S. Veshchunov, V. E. Shestak, Modelling of fission gas release from irradiated UO$_2$ fuel under high-temperature annealing conditions, Journal of Nuclear Materials 430 (1-3) (2012) 82–89. doi:10.1016/j.jnucmat.2012.06.048.

[37] V. I. Tarasov, P. V. Polovnikov, V. E. Shestak, M. S. Veshchunov, Development of the MFPR/R code for characterization of the rim zone and high burnup structure evolution in UO$_2$ fuel pellets, Journal of Nuclear Materials 517 (2019) 214–224. `doi:10.1016/j.jnucmat.2019.01.055`.

[38] M. Stan, Discovery and design of nuclear fuels, Materials Today 12 (11) (2009) 20–28. `doi:10.1016/S1369-7021(09)70295-0`.

[39] E. Kotomin, Y. Mastrikov, S. Rashkeev, P. Van Uffelen, Implementing first principles calculations of defect migration in a fuel performance code for UN simulations, Journal of Nuclear Materials 393 (2) (2009) 292–299.

[40] D. A. Andersson, P. Garcia, X. Y. Liu, G. Pastore, M. Tonks, P. Millett, B. Dorado, D. R. Gaston, D. Andrs, R. L. Williamson, R. C. Martineau, B. P. Uberuaga, C. R. Stanek, Atomistic modeling of intrinsic and radiation-enhanced fission gas (Xe) diffusion in UO$_{2\pm x}$: Implications for nuclear fuel performance modeling, Journal of Nuclear Materials 451 (1-3) (2014) 225–242. `doi:10.1016/j.jnucmat.2014.03.041`.

[41] M. R. Tonks, X. Y. Liu, D. Andersson, D. Perez, A. Chernatynskiy, G. Pastore, C. R. Stanek, R. Williamson, Development of a multiscale thermal conductivity model for fission gas in UO$_2$, Journal of Nuclear Materials 469 (2016) 89–98. `doi:10.1016/j.jnucmat.2015.11.042`.

[42] Y. Miao, K. A. Gamble, D. Andersson, B. Ye, Z. G. Mei, G. Hofman, A. M. Yacout, Gaseous swelling of U$_3$Si$_2$ during steady-state LWR operation: A rate theory investigation, Nuclear Engineering and Design 322 (2017) 336–344.

[43] T. Barani, G. Pastore, D. Pizzocri, D. A. Andersson, C. Matthews, A. Alfonsi, K. A. Gamble, P. Van Uffelen, L. Luzzi, J. D. Hales, Multiscale modeling of fission gas behavior in U$_3$Si$_2$ under LWR conditions, Journal of Nuclear Materials 522 (2019) 97–110. `doi:10.1016/j.jnucmat.2019.04.037`.

[44] M. Veshchunov, A. Boldyrev, A. Kuznetsov, V. Ozrin, M. Seryi, V. Shestak, V. Tarasov, G. Norman, A. Kuksin, V. Pisarev, D. Smirnova, S. Starikov, V. Stegailov, A. Yanilkin, Development of the advanced mechanistic fuel performance and safety code using the multi-scale approach, Nuclear Engineering and Design 295 (2015) 116 – 126. `doi:https://doi.org/10.1016/j.nucengdes.2015.09.035`.

[45] D. Yun, J. Rest, G. L. Hofman, A. M. Yacout, An initial assessment of a mechanistic model, GRASS-SST, in U-Pu-Zr metallic alloy fuel fission-gas behavior simulations, Journal of Nuclear Materials 435 (1-3) (2013) 153–163. `doi:10.1016/j.jnucmat.2012.12.024`.

[46] J. Rest, A generalized model for radiation-induced amorphization and crystallization of U$_3$Si and U$_3$Si$_2$ and recrystallization of UO$_2$ 248 (1997) 205–214.

[47] J. Rest, A model for fission-gas-bubble behavior in amorphous uranium silicide compounds, Journal of Nuclear Materials 325 (2-3) (2004) 107–117. `doi:10.1016/J.JNUCMAT.2003.11.008`.

[48] OECD-NEA, State-of-the-Art Report on Light Water Reactor Accident-Tolerant Fuels (2018) No.7317.

[49] P. Losonen, On the behaviour of intragranular fission gas in UO_2 fuel, Journal of Nuclear Materials 280 (1) (2000) 56–72. `doi:10.1016/S0022-3115(00)00028-3`.

[50] R. J. White, R. C. Corcoran, P. J. Barnes, A Summary of Swelling Data Obtained from the AGR/Halden Ramp Test Programme, Tech. Rep. R&T/NG/EXT/REP/0206/02 (2006).

[51] V. V. Rondinella, T. Wiss, The high burn-up structure in nuclear fuel, Materials Today 13 (12) (2010) 24–32. `doi:10.1016/S1369-7021(10)70221-2`.

[52] D. Pizzocri, T. Barani, L. Luzzi, SCIANTIX: A new open source multi-scale code for fission gas behaviour modelling designed for nuclear fuel performance codes, Journal of Nuclear Materials 532 (2020) 152042. `doi:https://doi.org/10.1016/j.jnucmat.2020.152042`.

[53] R. L. Williamson, J. D. Hales, S. R. Novascone, M. R. Tonks, D. R. Gaston, C. J. Permann, D. Andrs, R. C. Martineau, Multidimensional multiphysics simulation of nuclear fuel behavior, Journal of Nuclear Materials 423 (1-3) (2012) 149–163.

[54] H. Matzke, Gas release mechanisms in UO_2 - A critical review, Radiation effects 53 (1980) 219–242.

[55] C. Ronchi, Physical processes and mechanisms related to fission gas swelling in MX-type nuclear fuels, Journal of Nuclear Materials 84 (1-2) (1979) 55–84. `doi:10.1016/0022-3115(79)90150-8`.

[56] D. R. Olander, D. Wongsawaeng, Re-solution of fission gas - A review: Part I. Intragranular bubbles, Journal of Nuclear Materials 354 (1-3) (2006) 94–109. `doi:10.1016/j.jnucmat.2006.03.010`.

[57] J. Killeen, C. Baker, Fission gas release during post irradiation annealing of UO_2 up to 1750°C, in: Proceedings of the ANS Topical Meeting on LWR Fuel Performance, ANS, Orlando, Florida, 1985.

[58] G. J. Small, Bubble development and fission gas release during rapid heating of 18 GWd/teU UO_2, in: Specialists Meeting of Fission Product Release and Transport in Gas-Cooled Reactors, Berkeley, UK, 1985, pp. 114–137.

[59] S. Kashibe, K. Une, K. Nogita, Formation and growth of intragranular fission gas bubbles in UO_2 fuels with burnup of 6-83 GWd/t, Journal of Nuclear Materials 206 (1993) 22–34.

124

[60] I. Zacharie, S. Lansiart, P. Combette, M. Trotabas, M. Coster, M. Groos, Thermal treatment of uranium oxide irradiated in pressurized water reactor: Swelling and release of fission gases, Journal of Nuclear Materials 255 (2-3) (1998) 85–91.

[61] R. J. White, The growth of intra-granular bubbles in post-irradiation annealed UO_2 fuel, in: Technical committee meeting on nuclear fuel behaviour modelling at high burnup and its experimental support, IAEA, Windermere, UK, 2000, pp. 91–104.

[62] M. Mogensen, C. Walker, I. Ray, M. Coquerelle, Local fission gas release and swelling in water reactor fuel during slow power transients, Journal of Nuclear Materials 131 (1985) 162–171. doi:10.1016/S0065-2881(08)60234-5.

[63] P. Garcia, G. Martin, C. Sabathier, G. Carlot, A. Michel, P. Martin, B. Dorado, M. Freyss, M. Bertolus, R. Skorek, J. Noirot, L. Noirot, O. Kaitasov, S. Maillard, Nucleation and growth of intragranular defect and insoluble atom clusters in nuclear oxide fuels, Nuclear Instruments and Methods in Physics Research, Section B: Beam Interactions with Materials and Atoms 277 (2012) 98–108. doi:10.1016/j.nimb.2011.12.031.

[64] P. Losonen, On the effect of irradiation-induced resolution in modelling fission gas release in UO_2 LWR fuel, Journal of Nuclear Materials 496 (2017) 140–156. doi:10.1016/j.jnucmat.2017.09.015.

[65] C. Baker, The fission gas bubble distribution in uranium dioxide from high temperature irradiated SGHWR fuel pins, Journal of Nuclear Materials 66 (1977) 283–291.

[66] P. Van Uffelen, M. Sheindlin, V. Rondinella, C. Ronchi, On the relations between the fission gas behaviour and the pellet-cladding mechanical interaction in LWR fuel rods, in: Pellet-cladding interaction in water reactor fuels, 2004, pp. 213–228.

[67] M. H. A. Piro, D. Sunderland, S. Livingstone, J. Sercombe, W. Revie, A. Quastel, K. A. Terrani, C. Judge, A Review of Pellet–Clad Interaction Behavior in Zirconium Alloy Fuel Cladding, in: Reference Module in Materials Science and Materials Engineering, Elsevier, 2017.

[68] T. Jourdan, G. Bencteux, G. Adjanor, Efficient simulation of kinetics of radiation induced defects : A cluster dynamics approach, Journal of Nuclear Materials 444 (1-3) (2014) 298–313.

[69] ORNL–Fusion, Xolotl website (March 2019).
URL https://github.com/ORNL-Fusion/xolotl/

[70] S. Blondel, D. E. Bernholdt, K. D. Hammond, L. Hu, D. Maroudas, B. D. Wirth, Benchmarks and Tests of a Multidimensional Cluster Dynamics Model of Helium Implantation in Tungsten, Fusion Science and Technology 71 (1) (2017) 84–92.

[71] A. A. Kohnert, B. D. Wirth, L. Capolungo, Modeling microstructural evolution in irradiated materials with cluster dynamics methods: A review, Computational Materials Science 149 (2018) 442–459.

[72] G. Pastore, L. P. Swiler, J. D. Hales, S. R. Novascone, D. M. Perez, B. W. Spencer, L. Luzzi, P. Van Uffelen, R. L. Williamson, Uncertainty and sensitivity analysis of fission gas behavior in engineering-scale fuel modeling, Journal of Nuclear Materials 456 (2015) 398–408. `doi:10.1016/j.jnucmat.2014.09.077`.

[73] K. Lassmann, A. Schubert, P. Van Uffelen, C. Gyori, J. van de Laar, TRANSURANUS Handbook, Copyright © 1975-2018, Institute for Transuranium Elements, Karlsruhe, 2018.

[74] J. D. Hales, R. L. Williamson, S. R. Novascone, G. Pastore, B. W. Spencer, D. S. Stafford, K. A. Gamble, D. M. Perez, W. Liu, BISON Theory Manual: The Equations behind Nuclear Fuel Analysis, 2016. `doi:10.2172/1374503`.

[75] M. S. Veshchunov, On the theory of fission gas bubble evolution in irradiated UO_2 fuel, Journal of Nuclear Materials 277 (2000) 67 – 81.

[76] C. Baker, The migration of intragranular fission gas bubbles in irradiated uranium dioxide, Journal of Nuclear Materials 71 (1) (1977) 117–123. `doi:10.1016/0022-3115(77)90195-7`.

[77] L. He, X. Bai, J. Pakarinen, B. Jaques, J. Gan, A. Nelson, A. El-Azab, T. Allen, Bubble evolution in Kr-irradiated UO_2 during annealing, Journal of Nuclear Materials 496 (2017) 242–250. `doi:https://doi.org/10.1016/j.jnucmat.2017.09.036`.

[78] R. M. Cornell, An electron microscope examination of matrix fission-gas bubbles in irradiated uranium dioxide, Journal of Nuclear Materials 38 (3) (1971) 319–328. `doi:10.1016/0022-3115(71)90061-4`.

[79] K. Nogita, K. Une, High resolution TEM of high burnup UO_2 fuel, Journal of Nuclear Materials 250 (2-3) (1997) 244–249. `doi:10.1016/S0022-3115(97)00282-1`.

[80] K. Nogita, K. Une, High resolution TEM observation and density estimation of Xe bubbles in high burnup UO_2 fuels, Nuclear Instruments and Methods in Physics Research Section B: Beam Interactions with Materials and Atoms 141 (1998) 481–486.

[81] P. Martin, P. Garcia, G. Carlot, C. Sabathier, C. Valot, V. Nassif, O. Proux, J.-L. Hazemann, XAS characterisation of xenon bubbles in uranium dioxide, Nuclear Instruments and Methods in Physics Research Section B: Beam Interactions with Materials and Atoms 266 (12) (2008) 2887–2891, radiation Effects in Insulators. `doi:https://doi.org/10.1016/j.nimb.2008.03.180`.

[82] P. Martin, E. Vathonne, G. Carlot, R. Delorme, C. Sabathier, M. Freyss, P. Garcia, M. Bertolus, P. Glatzel, O. Proux, Behavior of fission gases in nuclear fuel: XAS characterization of Kr in UO_2, Journal of Nuclear Materials 466 (2015) 379–392. doi:https://doi.org/10.1016/j.jnucmat.2015.08.019.

[83] L. Thomas, Condensed-phase xenon and krypton in UO_2 spent fuel, in: S. Donnelly, J. Evans (Eds.), Fundamental Aspects of Inert Gases in Solids, Plenum Press, New York, 1991, pp. 431–441.

[84] L. Verma, L. Noirot, P. Maugis, Modelling intra-granular bubble movement and fission gas release during post-irradiation annealing of UO_2 using a mesoscale and spatialized approach, Journal of Nuclear Materials 528 (2020) 151874. doi:https://doi.org/10.1016/j.jnucmat.2019.151874.

[85] L. E. Thomas, R. J. Guenther, Characterization of Low-Gas-Release LHR Fuels by Transmission Electron Microscopy, MRS Proceedings 127 (1988) 293. doi:10.1557/PROC-127-293.

[86] R. J. White, A New Mechanistic Model for the Calculation of Fission Gas Release, in: Proceedings of the International topical meeting on Light Water Reactor Fuel Performance, ANS, Palm Beach, Florida, 1994, pp. 196–202.

[87] I. Lifshitz, V. Slyozov, The kinetics of precipitation from supersaturated solid solutions, Journal of Physics and Chemistry of Solids 19 (1-2) (1961) 35–50.

[88] C. Wagner, Theorie der Alterung von Niederschlagen durch Umlosen (Ostwald-Reifung), Zeitschrift fur Elektrochemie, Berichte der Bunsengesellschaft fur physikalische Chemie 65 (7-8) (1961) 581–591.

[89] A. Baldan, Progress in Ostwald ripening theories and their applications to nickel-base superalloys, Journal of Materials Science 37 (2002) 2171–2202.

[90] H. Trinkaus, The effect of internal pressure on the coarsening of inert gas bubbles in metals, Scripta metallurgica 23 (10) (1989) 1773–1778.

[91] H. Schroeder, P. F. Fichtner, On the coarsening mechanisms of helium bubbles - Ostwald ripening versus migration and coalescence, Journal of Nuclear Materials 179-181 (PART 2) (1991) 1007–1010.

[92] P. F. Fichtner, H. Schroeder, H. Trinkaus, A simulation study of Ostwald ripening of gas bubbles in metals accounting for real gas behaviour, Acta Metallurgica Et Materialia 39 (8) (1991) 1845–1852.

[93] J. Spino, A. D. Stalios, H. Santa Cruz, D. Baron, Stereological evolution of the rim structure in PWR-fuels at prolonged irradiation: Dependencies with burn-up and temperature, Journal of Nuclear Materials 354 (1-3) (2006) 66–84.

[94] H. Schroeder, P. Fichtner, H. Trinkaus, Inert gas bubble coarsening mechanisms, in: S. Donnelly, J. Evans (Eds.), Fundamental Aspects of Inert Gases in Solids, Plenum Press, New York, 1991, pp. 289–297.

[95] S. T. Murphy, A. Chartier, L. Van Brutzel, J.-P. Crocombette, Free energy of Xe incorporation at point defects and in nanovoids and bubbles in UO$_2$, Phys. Rev. B 85 (2012) 144102. `doi:10.1103/PhysRevB.85.144102`.

[96] W. Nixon, D. MacInnes, A model for bubble diffusion in uranium dioxide, Journal of Nuclear Materials 101 (1) (1981) 192–199.

[97] M. Veshchunov, V. Shestak, An advanced model for intragranular bubble diffusivity in irradiated UO$_2$ fuel, Journal of Nuclear Materials 376 (2) (2008) 174–180. `doi:https://doi.org/10.1016/j.jnucmat.2008.01.026`.

[98] R. W. Grimes, C. R. A. Catlow, The stability of fission products in uranium dioxide, Philosophical Transactions of the Royal Society of London. Series A: Physical and Engineering Sciences 335 (1639) (1991) 609–634.

[99] L. Noirot, A method to calculate equilibrium concentrations of gas and defects in the vicinity of an over-pressured bubble in UO$_2$, Journal of Nuclear Materials 447 (1-3) (2014) 166–178. `doi:10.1016/j.jnucmat.2014.01.011`.

[100] L. Verma, L. Noirot, P. Maugis, A new spatially resolved model for defects and fission gas bubbles interaction at the mesoscale, Nuclear Instruments and Methods in Physics Research, Section B: Beam Interactions with Materials and Atoms (October) (2018) 1–8. `doi:10.1016/j.nimb.2018.10.028`.

[101] J. Spino, J. Rest, W. Goll, C. T. Walker, Matrix swelling rate and cavity volume balance of UO$_2$ fuels at high burn-up, Journal of Nuclear Materials 346 (2-3) (2005) 131–144. `doi:10.1016/j.jnucmat.2005.06.015`.

[102] J. A. Turnbull, The distribution of intragranular fission gas bubbles in UO$_2$ during irradiation, Journal of Nuclear Materials 38 (1971) 203–212.

[103] G. Martin, P. Garcia, C. Sabathier, L. Van Brutzel, B. Dorado, F. Garrido, S. Maillard, Irradiation-induced heterogeneous nucleation in uranium dioxide, Physics Letters, Section A: General, Atomic and Solid State Physics 374 (30) (2010) 3038–3041. `doi:10.1016/j.physleta.2010.05.033`.

[104] G. Greenwood, A. Foreman, D. Rimmer, The role of vacancies and dislocations in the nucleation and growth of gas bubbles in irradiated fissile material, Journal of Nuclear Materials 1 (4) (1959) 305 – 324.

[105] F. Ham, Theory of diffusion-limited precipitation, J. Phys. Chem. Solids 6 (1958) 335–351.

[106] J. A. Turnbull, R. J. White, C. Wise, The diffusion coefficient for fission gas atoms in uranium dioxide, in: International Working Group on Water Reactor Fuel Performance and Technology, Technical committee on water reactor fuel element computer modelling in steady state, transient and accident conditions, Preston, U.K., 1989.

128

[107] S. T. Murphy, P. Fossati, R. W. Grimes, Xe diffusion and bubble nucleation around edge dislocations in UO_2, Journal of Nuclear Materials 466 (2015) 634–637. `doi:10.1016/j.jnucmat.2015.09.007`.

[108] H. Blank, H. J. Matzke, The effect of fission spikes on fission gas re-solution, Radiation Effects 17 (1-2) (1973) 57–64.

[109] R. Nelson, The stability of gas bubbles in an irradiation environment, Journal of Nuclear Materials 31 (2) (1969) 153–161.

[110] D. Schwen, M. Huang, P. Bellon, R. S. Averback, Molecular dynamics simulation of intragranular Xe bubble re-solution in UO_2, Journal of Nuclear Materials 392 (1) (2009) 35–39. `doi:10.1016/j.jnucmat.2009.03.037`.

[111] D. Schwen, R. S. Averback, Intragranular Xe bubble population evolution in UO_2: A first passage Monte Carlo simulation approach, Journal of Nuclear Materials 402 (2-3) (2010) 116–123. `doi:10.1016/j.jnucmat.2010.05.006`.

[112] K. Govers, C. L. Bishop, D. C. Parfitt, S. E. Lemehov, M. Verwerft, R. W. Grimes, Molecular dynamics study of Xe bubble re-solution in UO_2, Journal of Nuclear Materials 420 (1-3) (2012) 282–290. `doi:10.1016/j.jnucmat.2011.10.010`.

[113] W. Setyawan, M. W. Cooper, K. J. Roche, R. J. Kurtz, B. P. Uberuaga, D. A. Andersson, B. D. Wirth, Atomistic model of xenon gas bubble re-solution rate due to thermal spike in uranium oxide, Journal of Applied Physics 124 (7). `doi:10.1063/1.5042770`.

[114] M. Speight, W. Beere, Vacancy potential and void growth on grain boundaries, Met. Sci. 9 (1975) 190–191.

[115] D. R. Olander, Interaction of stresses with inclusions in solids - a review, Journal of Nuclear Materials 92 (1980) 163–183.

[116] N. F. Carnahan, K. E. Starling, Equation of state for nonattracting rigid spheres, The Journal of Chemical Physics 51 (2) (1969) 635–636. `doi:10.1063/1.1672048`.

[117] I. R. Brearley, D. A. MacInnes, An improved equation of state for inert gases at high pressures, Journal of Nuclear Materials 95 (3) (1980) 239–252. `doi:10.1016/0022-3115(80)90365-7`.

[118] L. Van Brutzel, A. Chartier, A new equation of state for helium nanobubbles embedded in UO_2 matrix calculated via molecular dynamics simulations, Journal of Nuclear Materials 518 (2019) 431 – 439. `doi:https://doi.org/10.1016/j.jnucmat.2019.02.015`.

[119] A. Jelea, An equation of state for xenon/krypton mixtures confined in the nuclear fuels, Journal of Nuclear Materials 530 (2020) 151952. `doi:https://doi.org/10.1016/j.jnucmat.2019.151952`.

[120] D. A. Andersson, M. R. Tonks, L. Casillas, S. Vyas, P. Nerikar, B. P. Uberuaga, C. R. Stanek, Multiscale simulation of xenon diffusion and grain boundary segregation in UO$_2$, Journal of Nuclear Materials 462 (2015) 15–25. doi: 10.1016/j.jnucmat.2015.03.019.

[121] S. T. Murphy, E. E. Jay, R. W. Grimes, Pipe diffusion at dislocations in UO$_2$, Journal of Nuclear Materials 447 (1-3) (2014) 143–149. doi:10.1016/j.jnucmat.2013.12.029.

[122] L. K. Mansur, Void swelling in metals and alloys under irradiation: An assessment of the theory, Nuclear Technology 40 (1) (1978) 5–34. doi: 10.13182/NT78-2.

[123] S. Torquato, Random Heterogeneous Materials: Microstructure and Macroscopic Properties, Vol. 82, 2013. arXiv:1406.6401, doi:10.1016/j.camwa.2013.03.019.

[124] F. Cappia, Investigation of very high burnup UO$_2$ fuels in Light Water Reactors, Ph.D. thesis, Technischen Universität München (2017).

[125] S. Torquato, Nearest-neighbor statistics fo packings hard-spheres and disks, Physical Review E 51 (4) (1995) 3170–3182.

[126] S. Torquato, B. Lu, J. Rubinstein, Nearest-neighbor distribution functions in many-body systems, Phys. Rev. A 41 (1990) 2059–2075.

[127] P. Van Uffelen, G. Pastore, V. Di Marcello, L. Luzzi, Multiscale modelling for the fission gas behaviour in the TRANSURANUS Code, Nuclear Engineering and Technology 43 (6) (2011) 477–488. doi:10.5516/NET.2011.43.6.477.

[128] R. Bès, P. Martin, E. Vathonne, R. Delorme, C. Sabathier, M. Freyss, M. Bertolus, P. Glatzel, Experimental evidence of Xe incorporation in Schottky defects in UO$_2$, Applied Physics Letters 106 (11) (2015) 114102. doi:10.1063/1.4914300.

[129] K. Nogita, K. Une, Radiation-induced microstructural change in high burnup UO$_2$ fuel pellets, Nuclear Instruments and Methods in Physics Research Section B: Beam Interactions with Materials and Atoms 91 (1994) 301–306.

[130] H. Trinkaus, B. Singh, A. Foreman, Mechanisms for decoration of dislocations by small dislocation loops under cascade damage conditions, Journal of Nuclear Materials 249 (2–3) (1997) 91–102.

[131] M. S. Veshchunov, V. E. Shestak, Model for evolution of crystal defects in UO$_2$ under irradiation up to high burn-ups, Journal of Nuclear Materials 384 (2009) 12–18. doi:10.1016/j.jnucmat.2008.09.024.

[132] P. V. Nerikar, D. C. Parfitt, L. A. Casillas Trujillo, D. A. Andersson, C. Unal, S. B. Sinnott, R. W. Grimes, B. P. Uberuaga, C. R. Stanek, Segregation of xenon to dislocations and grain boundaries in uranium dioxide, Physical

Review B - Condensed Matter and Materials Physics 84 (17) (2011) 1–11. doi:10.1103/PhysRevB.84.174105.

[133] T. Jourdan, Influence of dislocation and dislocation loop biases on microstructures simulated by rate equation cluster dynamics, Journal of Nuclear Materials 467 (2015) 286–301. doi:10.1016/j.jnucmat.2015.09.046.

[134] J. A. Turnbull, C. A. Friskney, J. R. Findlay, F. A. Johnson, A. J. Walter, The diffusion coefficients of gaseous and volatile species during the irradiation of uranium dioxide, Journal of Nuclear Materials 107 (2-3) (1982) 168–184.

[135] T. Kogai, Modelling of fission gas release and gaseous swelling of light water reactor fuels, Journal of Nuclear Materials 244 (1997) 131–140. doi:10.1016/S0022-3115(96)00731-3.

[136] G. Rossiter, Development of the ENIGMA fuel performance code for whole core analysis ad dry storage assessments, Nuclear Engineering and Technology 43 (6) (2011) 489–498. doi:10.5516/NET.2011.43.6.489.

[137] G. Pastore, P. Van Uffelen, L. Luzzi, Modeling of Fission Gas Behavior in Uranium Oxide Nuclear Fuel Applied to Engineering Fuel Performance Codes, in: 2019 Annual I-NERI Review Meeting, Lawrence Livermore National Laboratory, USA, 2019.

[138] W. Barney, B. Wemble, Metallography of UO_2-Containing Fuel Elements, KAPL-1836, January, 1958.

[139] J. Belle, Uranium dioxide: properties and nuclear applications, Vol. 4, Naval Reactors, Division of Reactor Development, US Atomic Energy Commission, 1961.

[140] J. Noirot, L. Desgranges, J. Lamontagne, Detailed characterisations of high burn-up structures in oxide fuels, Journal of Nuclear Materials 372 (2-3) (2008) 318–339.

[141] T. Wiss, V. V. Rondinella, R. J. M. Konings, D. Staicu, D. Papaioannou, S. Bremier, P. Pöml, O. Benes, J.-Y. Colle, P. Van Uffelen, A. Schubert, F. Cappia, M. Marchetti, D. Pizzocri, F. Jatuff, W. Goll, T. Sonoda, A. Sasahara, S. Kitajima, M. Kinoshita, Properties of the high burnup structure in nuclear light water reactor fuel, Radiochimica Acta 105 (11) (2017) 893–906.

[142] C. T. Walker, M. Coquerelle, Correlation between microstructure and fission gas release in high burnup UO_2 and MOX fuel, in: Proceedings International Topical Meeting On Light Water Reactor Fuel Performance, Avignon, Vol. 506, 1991.

[143] F. Lemoine, D. Baron, P. Blanpain, Key parameters for the High Burnup Structure fromation thresholds, in: 2010 LWR Fuel Performance Meeting/Top Fuel/WRFPM, Orlando, Florida, USA, 2010.

[144] A. Bouloré, L. Aufore, E. Federici, P. Blanpain, R. Blachier, Advanced characterization of MIMAS MOX fuel microstructure to quantify the HBS formation, Nuclear Engineering and Design 281 (October 2014) (2015) 79–87.

[145] C. T. Walker, G. Nicolaou, Transmutation of neptunium and americium in a fast neutron flux: EPMA results and KORIGEN predictions for the Superfact fuels, Journal of Nuclear Materials 218 (2) (1995) 129–138.

[146] K. Maeda, K. Katsuyama, T. Asaga, Fission gas release in FBR MOX fuel irradiated to high burnup, Journal of Nuclear Materials 346 (2-3) (2005) 244–252. `doi:10.1016/j.jnucmat.2005.06.014`.

[147] I. Ray, H. Matzke, Observation of a high burnup rim-type structure in an advanced plutonium–uranium carbide fuel, Journal of Nuclear Materials 250 (2) (1997) 242–243.

[148] A. Leenaers, W. Van Renterghem, S. Van den Berghe, High burn-up structure of U(Mo) dispersion fuel, Journal of Nuclear Materials 476 (2016) 218–230.

[149] H. Matzke, M. Kinoshita, Polygonization and high burnup structure in nuclear fuels, Journal of Nuclear Materials 247 (1997) 108–115. `doi:10.1016/S0022-3115(97)00081-0`.

[150] D. Baron, M. Kinoshita, P. Thevenin, R. Largenton, Discussion about HBS transformation in high burn-up fuels, Nuclear Engineering and Technology 41 (2) (2009) 199–214.

[151] J. Rest, G. Hofman, Dynamics of irradiation-induced grain subdivision and swelling in U_3Si_2 and UO_2 fuels, Journal of Nuclear Materials 210 (1-2) (1994) 187–202.

[152] M. Kinoshita, Towards the mathematical model of rim structure formation, Journal of Nuclear Materials 248 (1997) 185–190.

[153] K. Nogita, K. Une, M. Hirai, K. Ito, K. Ito, Y. Shirai, Effect of grain size on recrystallization in high burnup fuel pellets, Journal of Nuclear Materials 248 (1997) 196–203.

[154] J. Rest, G. Hofman, An alternative explanation for evidence that xenon depletion, pore formation, and grain subdivision begin at different local burnups, Journal of Nuclear Materials 277 (2-3) (2000) 231–238.

[155] K. Une, K. Nogita, T. Shiratori, K. Hayashi, Rim structure formation of isothermally irradiated UO_2 fuel discs, Journal of Nuclear Materials 288 (1) (2001) 20–28.

[156] H. Xiao, C. Long, H. Chen, Model for evolution of grain size in the rim region of high burnup UO_2 fuel, Journal of Nuclear Materials 471 (2016) 74–79.

[157] H. Matzke, On the rim effect in high burnup UO_2 LWR fuels, Journal of Nuclear Materials 189 (1) (1992) 141–148.

[158] Matzke, H. J. and Turos, A. and Linker, G., Polygonization of single crystals of the fluorite-type oxide UO_2 due to high dose ion implantation $+$, Nuclear Instruments and Methods in Physics Research Section B: Beam Interactions with Materials and Atoms 91 (1) (1994) 294–300.

[159] I. L. F. Ray, H. J. Matzke, H. A. Thiele, M. Kinoshita, An electron microscopy study of the RIM structure of a UO_2 fuel with a high burnup of 7.9% FIMA, Journal of Nuclear Materials 245 (2-3) (1997) 115–123.

[160] T. Sonoda, M. Kinoshita, I. Ray, T. Wiss, H. Thiele, D. Pellottiero, V. Rondinella, H. Matzke, Transmission electron microscopy observation on irradiation-induced microstructural evolution in high burn-up UO_2 disk fuel, Nuclear Instruments and Methods in Physics Research Section B: Beam Interactions with Materials and Atoms 191 (1) (2002) 622 – 628.

[161] T. Sonoda, M. Kinoshita, N. Ishikawa, M. Sataka, A. Iwase, K. Yasunaga, Clarification of high density electronic excitation effects on the microstructural evolution in UO_2, Nucl. Instruments Methods Phys. Res. Sect. B Beam Interact. with Mater. Atoms 268 (19) (2010) 3277 – 3281.

[162] M. Chollet, G. Kuri, D. Grolimund, M. Marrtin, L. Bertsch, Synchrotron XRD Analysis of Irradiated UO_2 Fuel at Various Burn-up, in: TopFuel 2016: LWR Fuels with Enhanced Safety and Performance, Boise, Idaho, USA, 2016.

[163] C. Walker, Assessment of the radial extent and completion of recrystallisation in high burn-up UO_2 nuclear fuel by EPMA, Journal of Nuclear Materials 275 (1) (1999) 56–62.

[164] F. Cappia, D. Pizzocri, A. Schubert, P. Van Uffelen, G. Paperini, D. Pellottiero, R. Macian-Juan, V. V. Rondinella, Critical assessment of the pore size distribution in the rim region of high burnup UO_2 fuels, Journal of Nuclear Materials 480 (2016) 138–149.

[165] C. Ronchi, M. Sheindlin, D. Staicu, M. Kinoshita, Effect of burn-up on the thermal conductivity of uranium dioxide up to 100.000 MWd t^{-1}, Journal of Nuclear Materials 327 (1) (2004) 58–76.

[166] F. Cappia, D. Pizzocri, M. Marchetti, A. Schubert, P. V. Uffelen, L. Luzzi, D. Papaioannou, R. Macián-Juan, V. Rondinella, Microhardness and Young's modulus of high burn-up UO_2 fuel, Journal of Nuclear Materials 479 (2016) 447–454.

[167] OECD - NEA, Nuclear Fuel Behaviour in Loss-of-coolant Accident (LOCA) Conditions, Tech. Rep. NEA 6846 (2009).

[168] J. Noirot, Y. Pontillon, S. Yagnik, J. Turnbull, T. Tverberg, Fission gas release behaviour of a 103 GWd/tHM fuel disc during a 1200°C annealing test, J. Nucl. Mater. 446 (2014) 163 – 171.

133

[169]   OECD - NEA, Report on Fuel Fragmentation, Relocation, Dispersal, Tech. Rep. NEA-CSNI-R(2016)16 (2016).

[170]   A. Bianco, C. Vitanza, M. Seidl, A. Wensauer, W. Faber, R. Macián-Juan, Experimental investigation on the causes for pellet fragmentation under LOCA conditions, Journal of Nuclear Materials 465 (2015) 260–267.

[171]   OECD - NEA, Nuclear Fuel Behaviour during Reactivity Initiated Accidents, Tech. Rep. NEA-CSNI-R(2010)7 (2010).

[172]   K. Lassmann, C. Walker, J. van de Laar, F. Lindström, Modelling the high burnup UO$_2$ structure in LWR fuel, Journal of Nuclear Materials 226 (1995) 1–8.

[173]   L.O. Jernkvist, Modelling of fine fragmentation and fission gas release of UO$_2$ fuel in accident conditions, EPJ Nuclear Sci. Technol. 5 (2019) 11.

[174]   J. Rest, A model for the influence of microstructure, precipitate pinning and fission gas behavior on irradiation-induced recrystallization of nuclear fuels, Journal of Nuclear Materials 326 (2) (2004) 175–184.

[175]   K. Geelhood, W. Luscher, P. Raynaud, I. Porter, FRAPCON-4.0: a Computer Code for the Calculation of Steady-state, Thermal-Mechanical Behavior of Oxide Fuel Rods for High Burnup, Tech. Rep. PNNL-19417, Vol. 1 Rev. 2 (2015).

[176]   M. Lemes, A. Soba, A. Denis, An empirical formulation to describe the evolution of the high burnup structure, Journal of Nuclear Materials 456 (2015) 174–181.

[177]   P. Blair, A. Romano, C. Hellwig, R. Chawla, Calculations on fission gas behaviour in the high burnup structure, Journal of Nuclear Materials 350 (3) (2006) 232–239.

[178]   A. Denis, A. Soba, Simulation of pellet-cladding thermomechanical interaction and fission gas release, Nuclear Engineering and Design 223 (2) (2003) 211–229.

[179]   G. Khvostov, V. Novikov, A. Medvedev, S. Bogatyr, Approaches to Modeling of High Burn-up Structure and Analysis of its Effects on the Behaviour of Light Water Reactor Fuels in the START-3 Fuel Performance Code, in: Water Reactor Fuel Performance Meeting/WRFPM 2005, 2005.

[180]   Y. Rashid, R. Dunham, R. Montgomery, Fuel Analysis and Licensing Code: FALCON MOD01 Volume 1: Theoretical and Numerical Bases 1 (3) (2004) 246.

[181]   L. Holt, A. Schubert, P. Van Uffelen, C. T. Walker, E. Fridman, T. Sonoda, Sensitivity study on Xe depletion in the high burn-up structure of UO$_2$, Journal of Nuclear Materials 452 (1-3) (2014) 166–172.

134

[182] K. Lassmann, A. Schubert, J. van de Laar, C. Vennix, Developments of the TRANSURANUS code with emphasis on high burnup phenomena, in: IAEA Technical Committee Meeting on Nuclear Fuel Behaviour Modelling at High Burnup, Lake Windermere, U.K., 2000.

[183] K. Nogita, K. Une, Irradiation-induced recrystallization in high burnup UO_2 fuel, Journal of Nuclear Materials 226 (3) (1995) 302–310.

[184] J. Sercombe, I. Aubrun, C. Nonon, Power ramped cladding stresses and strains in 3D simulations with burnup-dependent pellet-clad friction, Nuclear Engineering and Design 242 (2012) 164–181.

[185] B. Baurens, J. Sercombe, C. Riglet-Martial, L. Desgranges, L. Trotignon, P. Maugis, 3D thermo-chemical-mechanical simulation of power ramps with ALCYONE fuel code, Journal of Nuclear Materials 452 (1-3) (2014) 578–594.

[186] D. Pizzocri, F. Cappia, L. Luzzi, G. Pastore, V. Rondinella, P. Van Uffelen, A semi-empirical model for the formation and depletion of the high burnup structure in UO_2, Journal of Nuclear Materials 487. `doi:10.1016/j.jnucmat.2017.01.053`.

[187] T. J. Gerczak, C. M. Parish, P. D. Edmondson, C. A. Baldwin, K. A. Terrani, Restructuring in high burnup UO_2 studied using modern electron microscopy 509 (2018) 245–259.

[188] J. Rest, The effect of irradiation-induced gas-atom re-solution on grain-boundary bubble growth, Journal of Nuclear Materials 321 (2-3) (2003) 305–312. `doi:10.1016/S0022-3115(03)00303-9`.

[189] V. I. Tarasov, M. S. Veshchunov, Models for fuel porosity evolution in UO_2 under various regimes of reactor operation, Nuclear Engineering and Design 272 (2014) 65–83. `doi:10.1016/j.nucengdes.2014.02.016`.

[190] M. S. Veshchunov, V. I. Tarasov, Modelling of pore coarsening in the high burn-up structure of UO_2 fuel, Journal of Nuclear Materials 488 (2017) 191–195. `doi:10.1016/j.jnucmat.2017.03.013`.

[191] A. Kolmogorov, On the Statistical Theory of Metal Crystallization, Izv. Akad. Nauk SSSR, Ser. Math (1937) 335–360.

[192] M. Kinoshita, Mesoscopic approach to describe high burn-up fuel behaviour, in: Enlarged HPG meeting on high burn-up fuel performance, safety and reliability and degradation of in-core materials and water chemistry effects and man-machine systems research, Loen (Norway), 24-29 May, 1999.

[193] J. Noirot, Y. Pontillon, S. Yagnik, J. A. Turnbull, Post-irradiation examinations and high-temperature tests on undoped large-grain UO_2 discs, Journal of Nuclear Materials 462 (2015) 77–84.

[194] E. Ruzauskas, K. Fardell, Design, Operation, and Performance Data for High Burnup PWR Fuel from the H. B. Robinson Plant for Use in the NRC Experimental Program at Argonne National Laboratory, Tech. Rep. Electric Power Research Institute, Palo Alto, CA, US, 1001558 (2001).

[195] A. Schubert, P. Van Uffelen, J. van de Laar, C. Walker, W. Haeck, Extension of the TRANSURANUS burn-up model, Journal of Nuclear Materials 376 (1) (2008) 1–10. doi:10.1016/J.JNUCMAT.2008.01.006.

[196] J. Noirot, J. Lamontagne, N. Nakae, T. Kitagawa, Y. Kosaka, T. Tverberg, Heterogeneous UO_2 fuel irradiated up to a high burn-up: Investigation of the HBS and of fission product releases, Journal of Nuclear Materials 442 (1-3) (2013) 309–319.

[197] J. W. Cahn, Transformation kinetics during continuous cooling, Acta Metallurgica 4 (6) (1956) 572–575.

[198] J. Noirot, I. Zacharie-Aubrun, T. Blay, Focused ion beam–scanning electron microscope examination of high burn-up UO_2 in the center of a pellet, Nuclear Engineering and Technology 50 (2) (2018) 259 – 267.

[199] A. H. Booth, A method of calculating fission gas diffusion from UO_2 fuel and its application to the X-2-f loop test, Atomic Energy of Canada Limited Chalk River Project Research and Development, Report AECL-496 (496) (1957) 1–23.

[200] M. Speight, A Calculation on the Migration of Fission Gas in Material Exhibiting Precipitation and Re-solution of Gas Atoms Under Irradiation, Nuclear Science and Engineering 37 (1969) 180–185.

[201] G. Pastore, D. Pizzocri, C. Rabiti, T. Barani, P. Van Uffelen, L. Luzzi, An effective numerical algorithm for intra-granular fission gas release during non-equilibrium trapping and resolution, Journal of Nuclear Materials 509 (2018) 687–699. doi:10.1016/j.jnucmat.2018.07.030.

[202] H. Matzke, Xenon migration and trapping in doped ThO_2, Journal of Nuclear Materials 21 (2) (1967) 190 – 198.

[203] H. Kleykamp, The chemical state of the fission products in oxide fuels, Journal of Nuclear Materials 131 (2-3) (1985) 221–246.

[204] S. Middleburgh, R. Grimes, K. Desai, P. Blair, L. Hallstadius, K. Backman, P. Van Uffelen, Swelling due to fission products and additives dissolved within the uranium dioxide lattice, Journal of Nuclear Materials 427 (1) (2012) 359–363. doi:https://doi.org/10.1016/j.jnucmat.2012.03.037.

[205] R. Ducher, R. Dubourg, M. Barrachin, A. Pasturel, First-principles study of defect behavior in irradiated uranium monocarbide, Phys. Rev. B 83 (2011) 104107. doi:10.1103/PhysRevB.83.104107.

136

[206] M. Klipfel, V. Di Marcello, A. Schubert, J. van de Laar, P. Van Uffelen, Towards a multiscale approach for assessing fission product behaviour in un, Journal of Nuclear Materials 442 (1) (2013) 253 – 261. `doi:https://doi.org/10.1016/j.jnucmat.2013.08.056`.

[207] C. F. Clement, M. H. Wood, Equations for the Growth of a Distribution of Small Physical Objects, Proc. R. Soc. London A368 (1979) 521.

[208] M. Fell, S. M. Murphy, The nucleation and growth of gas bubbles in irradiated metals, Journal of Nuclear Materials 172 (1990) 1–12.

[209] U. Gösele, Concentration dependence of rate constants for diffusion- or reaction-controlled void-point-defect reactions, Journal of Nuclear Materials 78 (1) (1978) 83–95. `doi:10.1016/0022-3115(78)90507-X`.

[210] N. L. Peterson, Diffusion mechanisms and structural effects in grain boundaries, Journal of Vacuum Science & Technology A: Vacuum, Surfaces, and Films 4 (6) (1986) 3066–3070. `doi:10.1116/1.573629`.

[211] D. Baron, B. Hermitte, J. Piron, An attempt to simulate the porosity buildup in the rim at high burnup, in: IAEA Technical Committee meeting on advances in fuel pellet technology for improved performance at high burnup, Tokyo, Japan, 1996.

[212] K. Kulacsy, Mechanistic model for the fragmentation of the high-burnup structure during LOCA, Journal of Nuclear Materials 466 (2015) 409–416. `doi:10.1016/j.jnucmat.2015.08.015`.

[213] C. Walker, S. Bremier, S. Portier, R. Hasnaoui, W. Goll, SIMS analysis of an UO_2 fuel irradiated at low temperature to 65 MWd/kgHM, Journal of Nuclear Materials 393 (2) (2009) 212–223.

[214] S. Brémier, C. Walker, Radiation-enhanced diffusion and fission gas release from recrystallised grains in high burn-up UO_2 nuclear fuel, Radiation Effects and Defects in Solids 157 (3) (2002) 311–322.

[215] D. Olander, P. Van Uffelen, On the role of grain boundary diffusion in fission gas release, Journal of Nuclear Materials 288 (2-3) (2001) 137–147. `doi:10.1016/S0022-3115(00)00725-X`.

[216] H. J. Matzke, Atomic transport properties in UO_2 and mixed oxides $(U,Pu)O_2$, J. Chem. Soc., Faraday Trans. 2 83 (1987) 1121–1142.

[217] L. Thomas, Condensed-Phase Xenon and Krypton in UO_2 Spent Fuel, in: S. Donnelly, J. H. Evans (Eds.), Fundamental Aspects of Inert Gases in Solids, Springer US, 1991, pp. 431–441.

[218] P. Losonen, Methods for calculating diffusional gas release from spherical grains, Nuclear Engineering and Design 196 (2000) 161 – 173.

[219] C. Ronchi, Extrapolated equation of state for rare gases at high temperatures and densities, Journal of Nuclear Materials 96 (3) (1981) 314 – 328.

[220] S. Zinkle, K. Terrani, J. Gehin, L. Ott, L. Snead, Accident tolerant fuels for LWRs: A perspective, Journal of Nuclear Materials 448 (1-3) (2014) 374–379. doi:10.1016/J.JNUCMAT.2013.12.005.

[221] S. Bragg-Sitton, B. Merrill, M. Teague, L. Ott, K. Rob, M. Farmer, M. Billone, R. Montgomery, C. Stanek, M. Todosow, N. Brown, Advanced fuels campaign light water reactor accident tolerant fuel performance metrics, Tech. Rep. INL/EXT-13-29957 (2014).

[222] H.-G. Kim, J.-H. Yang, W.-J. Kim, Y.-H. Koo, Development Status of Accident-tolerant Fuel for Light Water Reactors in Korea, Nuclear Engineering and Technology 48 (1) (2016) 1 – 15.

[223] State-of-the-Art Report on Light Water Reactor Accident-Tolerant Fuels, Tech. Rep. OECD/NEA No. 7317 (November 2018).

[224] J. White, A. Nelson, D. Byler, J. Valdez, K. McClellan, Thermophysical properties of U_3Si to 1150K, Journal of Nuclear Materials 452 (1) (2014) 304–310. doi:10.1016/j.jnucmat.2014.05.037.

[225] J. White, A. Nelson, J. Dunwoody, D. Byler, D. Safarik, K. McClellan, Thermophysical properties of U_3Si_2 to 1773 K, Journal of Nuclear Materials 464 (2015) 275–280.

[226] J. Wood, M. Foo, L. Berthiaume, L. Herbert, J. Schaefer, Advances in the Manufacturing and Irradiation of Reduced Enrichment Fuels For Canadian Research Reactors, in: Proc. of the Int. Meeting on Reduced Enrichment Fuels for Research and Test Reactors, Tokai, Japan, October, no. JAERI-M-84-073, 1983.

[227] J. Snelgrove, R. Domagala, G. Hofman, T. Weincek, G. Copeland, R. Hobbs, R. Senn, The Use Of U_3Si_2 Dispersions in Aluminum in Plate-Type Fuel Elements for Research and Test Reactors, Tech. Rep. ANL/RERTR/TM-11 (1987).

[228] W. Krug, E. Groos, J. Seferiadis, Thamm, Final Results of Test–Irradiations with LEU–Plates at KFA Jülich, in: Proc. of the Int. Meeting on Reduced Enrichment Fuels for Research and Test Reactors, San Diego, California, USA, 19–22 September, 1988.

[229] M. Ugajin, M. Akabori, A. Itoh, H. Someya, T. Nakagawa, K. Ohsawa, Capsule Irradiation Tests of U-Si and U-Me (Fe,Ni,Mn) Alloys for Use in Research Reactors, in: Proc. of the Int. Meeting on Reduced Enrichment Fuels for Research and Test Reactors, Oarai, Ibaraki, Japan, October, 1993.

138

[230] D. Sears, M. Primeau, C. Buchanan, D. Rose, Post-Irradiation Examination Of Prototype Al-64 wt% U_3Si_2 Fuel Rods from NRU , in: Proc. of the Int. Meeting on Reduced Enrichment Fuels for Research and Test Reactors, Williamsburg, Virginia, USA, 18–23 September, 1994.

[231] A. Leenaers, S. Van Den Berghe, E. Koonen, P. Jacquet, C. Jarousse, B. Guigon, A. Ballagny, L. Sannen, Microstructure of U_3Si_2 fuel plates submitted to a high heat flux, Journal of Nuclear Materials 327 (2-3) (2004) 121–129. doi:10.1016/j.jnucmat.2004.01.025.

[232] H. Shimizu, The properties and irradiation behavior of U_3Si_2, Tech. Rep. NAA-SR-10621, Atomics International (1965).

[233] J. M. Harp, F. Cappia, Accident Tolerant Fuels (ATF-1) Irradiation Tests: overview of the ongoing post-irradiation examinations, in: 2018 ANS annual meeting, Philadelphia, US, 2018, pp. 4–7.

[234] G. L. Hofman, Crystal structure stability and fission gas swelling in intermetallic uranium compounds, Journal of Nuclear Materials 140 (3) (1986) 256–263. doi:10.1016/0022-3115(86)90208-4.

[235] R. Birtcher, J. Richardson Jr, M. Mueller, Amorphization of U_3Si by ion or neutron irradiation, Journal of Nuclear Materials 244 (3) (1997) 251–257. doi:10.1016/S0022-3115(96)00741-6.

[236] M. R. Finlay, G. L. Hofman, J. L. Snelgrove, Irradiation behaviour of uranium silicide compounds, Journal of Nuclear Materials 325 (2-3) (2004) 118–128. doi:10.1016/j.jnucmat.2003.11.009.

[237] R. C. Birtcher, J. W. Richardson, M. H. Mueller, Amorphization of U_3Si_2 by ion or neutron irradiation, Journal of Nuclear Materials 230 (2) (1996) 158–163. doi:10.1016/0022-3115(96)00160-2.

[238] Y. S. Kim, G. L. Hofman, J. Rest, A. B. Robinson, Temperature and dose dependence of fission-gas-bubble swelling in U_3Si_2, Journal of Nuclear Materials 389 (3) (2009) 443–449. doi:10.1016/j.jnucmat.2009.02.037.

[239] Y. Miao, J. Harp, K. Mo, S. Zhu, T. Yao, J. Lian, A. M. Yacout, Bubble morphology in U_3Si_2 implanted by high-energy Xe ions at 300°C, Journal of Nuclear Materials 495 (2017) 146–153.

[240] Y. Miao, J. Harp, K. Mo, S. Zhu, T. Yao, A. M. Yacout, Bubble morphology in U_3Si_2 implanted by high-energy Xe ions at 600°C, Journal of Nuclear Materials (2017) 1–9.

[241] T. Yao, B. Gong, L. He, J. Harp, M. Tonks, J. Lian, Radiation-induced grain subdivision and bubble formation in U_3Si_2 at LWR temperature, Journal of Nuclear Materials 498 (2018) 169–175.

[242] T. Yao, B. Gong, L. He, Y. Miao, J. M. Harp, M. Tonks, J. Lian, In-situ TEM study of the ion irradiation behavior of U_3Si_2 and U_3Si_5, Journal of Nuclear Materials 511 (2018) 56 – 63.

[243] J. Rest, GRASS-SST: A Comprehensive Mechanistic Model for the Prediction of Fission-Gas Behavior in UO_2–Base Fuels during Steady-State and Transient Conditions, Tech. Rep. ANL-78-53 (1978).

[244] D. Andersson, P. Garcia, X.-Y. Liu, G. Pastore, M. Tonks, P. Millett, B. Dorado, D. Gaston, D. Andrs, R. Williamson, R. Martineau, B. Uberuaga, C. Stanek, Atomistic modeling of intrinsic and radiation-enhanced fission gas (Xe) diffusion in $UO_{2\pm x}$: Implications for nuclear fuel performance modeling, Journal of Nuclear Materials 451 (1) (2014) 225 – 242.

[245] D. Andersson, X.-Y. Liu, B. Beeler, S. Middleburgh, A. Claisse, C. Stanek, Density functional theory calculations of self- and Xe diffusion in U_3Si_2, Journal of Nuclear Materials 515 (2019) 312 – 325.

[246] G. Kresse, J. Furthmüller, Efficiency of ab-initio total energy calculations for metals and semiconductors using a plane-wave basis set, Computational Materials Science 6 (1) (1996) 15 – 50.

[247] G. Kresse, D. Joubert, From ultrasoft pseudopotentials to the projector augmented-wave method, Phys. Rev. B 59 (1999) 1758–1775.

[248] S. L. Dudarev, D. Nguyen Manh, A. P. Sutton, Effect of Mott-Hubbard correlations on the electronic structure and structural stability of uranium dioxide, Philosophical Magazine B 75 (5) (1997) 613–628.

[249] M. J. Noordhoek, T. M. Besmann, D. A. Andersson, S. C. Middleburgh, A. Chernatynskiy, Phase equilibria in the U-Si system from first-principles calculations, Journal of Nuclear Materials 479 (2016) 216 – 223.

[250] S. Middleburgh, R. Grimes, E. Lahoda, C. Stanek, D. Andersson, Non-stoichiometry in U_3Si_2, Journal of Nuclear Materials 482 (2016) 300 – 305.

[251] G. Mills, H. Jónsson, G. K. Schenter, Reversible work transition state theory: application to dissociative adsorption of hydrogen, Surface Science 324 (2) (1995) 305 – 337.

[252] D. A. Andersson, B. P. Uberuaga, P. V. Nerikar, C. Unal, C. R. Stanek, U and Xe transport in $UO_{2\pm x}$: Density functional theory calculations, Phys. Rev. B 84 (2011) 054105.

[253] R. S. Nelson, The stability of gas bubbles in an irradiation environment, Journal of Nuclear Materials 31 (2) (1969) 153–161.

[254] H. Blank, Properties of fission spikes in UO_2 and UC due to electronic stopping power, Physica Status Solidi (a) 10 (2) (1972) 465–478.

[255] H. Blank, H. Matzke, The effect of fission spikes on fission gas re-solution, Radiation Effects 17 (1-2) (1973) 57–64.

[256] C. Ronchi, P. T. Elton, Radiation re-solution of fission gas in uranium dioxide and carbide, Journal of Nuclear Materials 140 (3) (1986) 228–244.

[257] C. Matthews, D. Schwen, A. C. Klein, Radiation re-solution of fission gas in non-oxide nuclear fuel, Journal of Nuclear Materials 457 (C) (2015) 273–278.

[258] D. C. Parfitt, R. W. Grimes, Predicted mechanisms for radiation enhanced helium resolution in uranium dioxide, Journal of Nuclear Materials 381 (3) (2008) 216–222.

[259] J. F. Ziegler, J. P. Biersack, The Stopping and Range of Ions in Matter, in: Treatise on Heavy-Ion Science, Springer US, Boston, MA, 1985, pp. 93–129.

[260] K. Forsberg, A. Massih, Diffusion theory of fission gas migration in irradiated nuclear fuel UO_2, Journal of nuclear materials 135 (1985) 140–148.

[261] M. Fell, S. Murphy, The nucleation and growth of gas bubbles in irradiated metals, Journal of Nuclear Materials 172 (1) (1990) 1–12.

[262] D. Pizzocri, F. Cappia, V. V. Rondinella, P. Van Uffelen, Preliminary model for the pore growth in the HBS, Tech. Rep. JRC103064, European Commission, Directorate for Nuclear Safety and Security, JRC-Karlsruhe (2016).

[263] Y. Miao, B. Ye, Z.-G. Mei, D. Andersson, K. Mo, G. Hofman, A. M. Yacout, Fission Gas Swelling in U_3Si_2 at LWR Conditions, in: Top Fuel 2016, Boise, Idaho, USA, 2016.

[264] B. Beeler, M. Baskes, D. Andersson, M. W. Cooper, Y. Zhang, Molecular dynamics investigation of grain boundaries and surfaces in U_3Si_2, Journal of Nuclear Materials 514 (2019) 290 – 298.

[265] K. A. Gamble, J. D. Hales, G. Pastore, T. Barani, D. Pizzocri, Behavior of U_3Si_2 Fuel and FeCrAl Cladding under Normal Operating and Accident Reactor Conditions, Tech. Rep. INL/EXT-16-40059 Rev. 0, Idaho National Laboratory (2016).

[266] C. Vitanza, U. Graziani, N. T. Fordestrommen, K. Vilpponen, Fission gas release from in-pile measurements, Tech. Rep. HPR-221.10 (1978).

[267] A. Alfonsi, C. Rabiti, D. Mandelli, J. Cogliati, C. Wang, P. W. Talbot, D. P. Maljovec, C. Smith, RAVEN Theory Manual and User Guide, Tech. Rep. INL/EXT-16-38178, Idaho National Laboratory (2017).

[268] C. Rabiti, A. Alfonsi, J. Cogliati, D. Mandelli, R. Kinoshita, S. Sen, C. Wang, J. Chen, RAVEN User Manual, Tech. Rep. INL/EXT-15-34123, Idaho National Laboratory (2017).

[269] Y.-H. Koo, B.-H. Lee, D.-S. Sohn, Cosmos: A computer code to analyze LWR UO$_2$ and MOX fuel up to high burnup, Annals of Nuclear Energy 26 (1) (1999) 47–67. `doi:10.1016/S0306-4549(98)00033-4`.

[270] C. B. Lee, Y. S. Yang, D. H. Kim, S. K. Kim, J. G. Bang, A new mechanistic and engineering fission gas release model for a uranium dioxide fuel, Journal of Nuclear Science and Technology 45 (1) (2008) 60–71. `doi:10.1080/18811248.2008.9711415`.

[271] J. D. Hales, R. L. Williamson, S. R. Novascone, G. Pastore, B. W. Spencer, D. S. Stafford, K. A. Gamble, D. M. Perez, R. J. Gardner, W. Liu, BISON Theory Manual: the quations behind nuclear fuel analysis, Tech. Rep. Tech. Rep. INL/EXT-13-29930, Rev. 1, Idaho National Laboratory, Idaho Falls, ID, USA (2014).

[272] J. Sercombe, E. Fédérici, M. Le Saux, B. Michel, C. Poussard, 1D and 3D modeling of PCMI during a RIA with ALCYONE V1. 1, in: International Topical Meeting on Light Water Reactor Fuel Performance, Orlando, Florida, 2010.

[273] G. Khvostov, Models for numerical simulation of burst FGR in fuel rods under the conditions of RIA, Nuclear Engineering and Design 328 (2018) 36–57. `doi:10.1016/J.NUCENGDES.2017.12.028`.

[274] J. Y. R. Rashid, S. K. Yagnik, R. O. Montgomery, Light water reactor fuel performance modeling and multi-dimensional simulation, JOM 63 (8) (2011) 81. `doi:10.1007/s11837-011-0144-9`.

[275] M. Veshchunov, A. Boldyrev, V. Ozrin, V. Shestak, V. Tarasov, A new mechanistic code SFPR for modeling of single fuel rod performance under various regimes of LWR operation, Nuclear Engineering and Design 241 (8) (2011) 2822 – 2830. `doi:https://doi.org/10.1016/j.nucengdes.2011.05.032`.

[276] D. Pizzocri, T. Barani, L. Luzzi, SCIANTIX Code: online repository (December 2019).
URL `https://gitlab.com/poliminrg/sciantix`

[277] K. Lassmann, H. Benk, Numerical algorithms for intragranular fission gas release, Journal of Nuclear Materials 280 (2) (2000) 127–135. `doi:10.1016/S0022-3115(00)00044-1`.

[278] D. Pizzocri, C. Rabiti, L. Luzzi, T. Barani, P. Van Uffelen, G. Pastore, PolyPole-1: An accurate numerical algorithm for intra-granular fission gas release, Journal of Nuclear Materials 478 (2016) 333–342. `doi:10.1016/j.jnucmat.2016.06.028`.

[279] K. Salari, P. Knupp, Code Verification by the Method of Manufactured Solutions, Tech. rep. (2000).

[280] W. L. Oberkampf, T. G. Trucano, Verification and validation in computational fluid dynamics, Progress in Aerospace Sciences 38 (3) (2002) 209 – 272. doi:https://doi.org/10.1016/S0376-0421(02)00005-2.

[281] L. Verma, L. Noirot, P. Maugis, Modelling intra-granular bubble movement and fission gas release during post-irradiation annealing of UO_2 using a meso-scale and spatialized approach, Journal of Nuclear Materials 528 (2020) 151874. doi:https://doi.org/10.1016/j.jnucmat.2019.151874.

[282] M. J. F. Notley, J. R. MacEwan, Stepwise Release of Fission Gas from UO_2 Fuel , Nuclear Applications 2 (6) (1966) 477–480. doi:10.13182/nt66-a27540.

[283] R. M. Carroll, J. G. Morgan, R. B. Perez, O. Sisman, Fission Density, Burnup, and Temperature Effects on Fission-Gas Release From UO_2 , Nuclear Science and Engineering 38 (2) (1969) 143–155. doi:10.13182/nse69-a19519.

[284] K. Une, S. Kashibe, Fission gas release during post irradiation annealing of BWR fuels, Journal of Nuclear Science and Technology 27 (11) (1990) 1002–1016. doi:10.1080/18811248.1990.9731285.

[285] G. Ducros, Y. Pontillon, P. P. Malgouyres, Synthesis of the VERCORS experimental programme: Separate-effect experiments on Fission Product release, in support of the PHEBUS-FP programme, Annals of Nuclear Energy 61 (2013) 75–87. doi:10.1016/j.anucene.2013.02.033.

[286] W. Hering, The KWU fission gas release model for LWR fuel rods, Journal of Nuclear Materials 114 (1) (1983) 41–49. doi:10.1016/0022-3115(83)90071-5.

[287] G. L. Reynolds, B. Burton, Grain-boundary diffusion in uranium dioxide: the correlation between sintering and creep and a reinterpretation of creep mechanism, Journal of Nuclear Materials 82 (1979) 22–25.

[288] R. Hargreaves, D. Collins, A quantitative model for fission gas release and swelling in irradiated uranium dioxide, Journal of the British Nuclear Energy Society 15 (4) (1976) 311–318.

[289] M. Notley, I. Hastings, A microstructure-dependent model for fission product gas release and swelling in UO_2 fuel, Nuclear Engineering and Design 56 (1) (1980) 163–175. doi:10.1016/0029-5493(80)90180-6.

[290] P. Botazzoli, Helium production and behaviour in LWR oxide nuclear fuels, Ph.D. thesis, Politecnico di Milano, Italy (2011).

[291] P. Van Uffelen, P. Botazzoli, L. Luzzi, S. Bremier, A. Schubert, P. Raison, R. Eloirdi, M. A. Barker, An experimental study of grain growth in mixed oxide samples with various microstructures and plutonium concentrations, Journal of Nuclear Materials 434 (2013) 287–290.

[292] M. Hillert, On the theory of normal and abnormal grain growth, Acta Metallurgica 13 (3) (1965) 227–238. `doi:10.1016/0001-6160(65)90200-2`.

[293] J. Ainscough, B. Oldfield, J. Ware, Isothermal grain growth kinetics in sintered UO_2 pellets, Journal of Nuclear Materials 49 (2) (1973) 117–128. `doi:10.1016/0022-3115(73)90001-9`.

[294] M. R. Tonks, Y. Zhang, X. Bai, P. C. Millett, Demonstrating the temperature gradient impact on grain growth in UO_2 using the phase field method, Materials Research Letters 2 (1) (2014) 23–28. `doi:10.1080/21663831.2013.849300`.

[295] X.-M. Bai, Y. Zhang, M. R. Tonks, Testing thermal gradient driving force for grain boundary migration using molecular dynamics simulations, Acta Materialia 85 (2015) 95–106. `doi:10.1016/J.ACTAMAT.2014.11.019`.

[296] M. R. Tonks, Y. Zhang, A. Butterfield, X.-M. Bai, Development of a grain boundary pinning model that considers particle size distribution using the phase field method, Modelling and Simulation in Materials Science and Engineering 23 (4) (2015) 045009. `doi:10.1088/0965-0393/23/4/045009`.

[297] Y. Li, S. Hu, X. Sun, M. Stan, A review: Applications of the phase field method in predicting microstructure and property evolution of irradiated nuclear materials, npj Computational Materials 3 (1) (2017) 1–16. `doi:10.1038/s41524-017-0018-y`.

[298] J. Bainbridge, C. Forty, D. Martin, The grain growth of mixed oxide fuel during irradiation, Journal of Nuclear Materials 171 (2-3) (1990) 230–236. `doi:10.1016/0022-3115(90)90370-3`.

[299] R. N. Singh, Isothermal grain-growth kinetics in sintered UO_2 pellets, Journal of Nuclear Materials 64 (1-2) (1977) 174–178. `doi:10.1016/0022-3115(77)90021-6`.

[300] O. Khoruzhii, S. Kourtchatov, V. Likhanskii, New model of equiaxed grain growth in irradiated UO_2, Journal of Nuclear Materials 265 (1999) 112–116. `doi:10.1016/S0022-3115(98)00632-1`.

[301] M. Veshchunov, A new model of grain growth kinetics in UO_2 fuel pellets. Part 2: Normal grain growth kinetics controlled by pore migration, Journal of Nuclear Materials 346 (2-3) (2005) 220–225. `doi:10.1016/J.JNUCMAT.2005.06.010`.

[302] G. Pastore, C. Folsom, R. Williamson, J. Hales, L. Luzzi, D. Pizzocri, T. Barani, Modeling Fission Gas Behavior with the BISON Fuel Performance Code, in: EHPG meeting, Lillehammer, Norway, 2017.

[303] D. R. Olander, Theory of Helium Dissolution in Uranium Dioxide. II. Helium Solubility, Journal of Chemical Physics 43 (785).

[304] E. Maugeri, T. Wiss, J. P. Hiernaut, K. Desai, C. Thiriet, V. V. Rondinella, J. Y. Colle, R. J. M. Konings, Helium solubility and behaviour in uranium dioxide, Journal of Nuclear Materials 385 (2) (2009) 461–466. `doi:10.1016/j.jnucmat.2008.12.033`.

[305] L. Cognini, D. Pizzocri, T. Barani, P. Van Uffelen, A. Schubert, T. Wiss, L. Luzzi, Helium solubility in oxide nuclear fuel: Derivation of new correlations for Henry's constant, Nuclear Engineering and Design 340 (2018) 240–244. `doi:10.1016/j.nucengdes.2018.09.024`.

[306] K. Lassmann, C. O'Carroll, J. van de Laar, C. Walker, The radial distribution of plutonium in high burnup UO_2 fuels, Journal of Nuclear Materials 208 (3) (1994) 223–231. `doi:10.1016/0022-3115(94)90331-X`.

[307] K. Lassmann, C. Walker, J. van de Laar, Extension of the TRANSURANUS burnup model to heavy water reactor conditions, Journal of Nuclear Materials 255 (2-3) (1998) 222–233. `doi:10.1016/S0022-3115(98)00019-1`.

[308] D. Pizzocri, T. Barani, L. Luzzi, Coupling of TRANSURANUS with the SCIANTIX fission gas behaviour module, in: International Workshop " Towards nuclear fuel modelling in the various reactor types across Europe", 2019.

[309] M. Lainet, B. Michel, J.-C. Dumas, M. Pelletier, I. Ramière, GERMINAL, a fuel performance code of the PLEIADES platform to simulate the in-pile behaviour of mixed oxide fuel pins for sodium-cooled fast reactors, Journal of Nuclear Materials 516 (2019) 30–53.

Ringraziamenti

The route which led me to the defense of my PhD thesis has been windy, constantly uphill, often unpaved, yet ended up on a beautiful peak featured by an exquisite panorama. Beside the effort, I shall now express my gratefulness to a number of people who made it possible.

I owe my sincere gratitude to my tutor and supervisor, Prof. Lelio Luzzi, for having always believed in me, supported me, and guided me towards during these years. We had some harsh discussions and crossed our swords – figuratively – every now and then, but always under a high, mutual consideration, which resolved all of them in a cigarette smoked together. Lastly, I want to thank him for all the possibilities (and consequent responsibilities) he provided me, exceeding dramatically those had by the 99.99% of my fellow colleagues.

Dr. Giovanni Pastore deserves my heartfelt thanks for many things, but especially for having taught me the method and accuracy needed to develop an industrial scientific (nuclear) code. Our infinite discussions, on both coasts of the USA, on fission gas bubble evolution taught me more than any paper could do. Lastly, I want to thank him for the unique experiences and possibilities he made available to me, before and during this PhD.

Dr. Paul Van Uffelen guided me through the modeling of high burnup structure (among the rest). He would have deserved my deepest gratitude even if it would be the only thing I mention here. Yet, I am most grateful to him for having taught me the perspective under which analyzing the fuel performance world, and for being an unlimited source of matchless constructive comments on my work. Lastly, I am thankful for unveiling me the *dopple* espresso at the JRC-KA cafeteria.

I wish to thank Dr. Roland Dubourg (IRSN) for being an amazing office mate during my staying at the JRC-KA, being a great company on both scientific and sportive discussions. Dr. Arndt Schubert (JRC-KA) is acknowledged for his kindness, availability, and constructive discussions on the Transuranus code, and Prof. Roberto Caciuffo is acknowledged for having nicely hosted me in his unit at the JRC-KA. Prof. Koroush Shirvan (MIT) is acknowledged for having hosted me in his research group, for his sympathy, and constructive discussions on fuel performance and novel materials. Lastly, I deeply thank Dr. Fabiola Cappia (INL) for the discussion on the HBS characteristics and modeling aspects, for the patience and for the comprehension she showed to me in a delicate occasion.

The number of colleagues I met during these years is large, and I had the pleasure of having some of them become close friends of mine. First, the one who is bearing and supporting me, from a technical and personal point of view, since March 2015, Davide. You have been an amazing supervisor, a brilliant colleague, and a sincere friend. If I am writing this manuscript now, it is also thanks to you. A huge thanks is due also to Stefano L., for all the breakfasts, for having taught me the secrets of the train organization in Lombardia, for being an utterly prepared, frank, and critic